NRC Research Press

ARTICLE

Geology, mineralogy, S and Sr isotope geochemistry, and fluid inclusion analysis of barite associated with the Lemarchant Zn–Pb–Cu–Ag–Au-rich volcanogenic massive sulphide deposit, Newfoundland, Canada

Marie-Ève Lajoie, Stephen J. Piercey, James Conliffe, and Daniel Layton-Matthews

Abstract: Barite in the approximately 513 Ma Lemarchant volcanogenic massive sulphide (VMS) deposit, Newfoundland, consists of granular and bladed barite intimately associated with mineralization. Regardless of type, the composition of barite is homogeneous at bulk rock and mineral scale containing predominantly Ba, S, and Sr, with minor Ca and Na. The barite has homogeneous sulphur isotope compositions ($\delta^{34}S_{mean}$ = 27‰), similar to Cambrian seawater sulphate (25–35‰) and Sr isotope compositions ($^{87}Sr/^{86}Sr$ = 0.706905 to 0.707485). These results are consistent with barite having formed from fluid–fluid mixing between Cambrian seawater and VMS-related hydrothermal fluids. The $^{87}Sr/^{86}Sr$ values in the barite are lower than mid-Cambrian seawater, which suggests that some of the Sr was derived from the underlying Neoproterozoic basement. Fluid inclusions in bladed barite are low-salinity, CO_2-rich inclusions with homogenization temperatures between 245°–250 °C, and average salinity of 1.2 wt.% NaCl equivalent. Estimated minimum trapping pressures of between 1.7 to 2.0 kbars were calculated from aqueous–carbonic fluid inclusion assemblages. The fluid inclusion results reflect regional metamorphic reequilibration during younger Silurian regional metamorphism, rather than primary fluid signatures, despite the preservation of primary barite and fluid inclusion textures. These results illustrate that barite in VMS deposits records the physicochemical processes associated with VMS formation and the sources of fluids in ancient VMS deposits, as well as seawater sulphate and basement isotopic compositions. The results herein are not only relevant for the Lemarchant deposit but also for other barite-rich VMS deposits globally.

Key words: volcanogenic massive sulphide, barite, sulphur isotopes, strontium isotopes, Appalachians.

Résumé : La baryte dans le gisement de SMV Lemarchant de ~513 Ma, à Terre-Neuve, se présente sous forme granulaire et lamellaire et est intimement associée à la minéralisation. Peu importe sa forme, la composition de la baryte est homogène à l'échelle mesoscopique et microscopique, contenant principalement du Ba, du S, du Sr, avec des concentrations mineures de Ca et de Na. Les signatures des isotopes stables de soufre ($\delta^{34}S_{mean}$ = 27 ‰) et des isotopes de Sr ($^{87}Sr/^{86}Sr$ = 0,70699 à 0,0751) de la baryte sont homogènes, la signature des isotopes de soufre étant semblable à celle du sulfate dans l'eau de mer cambrienne (25–35 ‰). Ces résultats concordent avec l'interprétation selon laquelle la baryte s'est formée par le mélange d'eau de mer cambrienne et de fluides hydrothermaux associés à des SMV. Les valeurs de $^{87}Sr/^{86}Sr$ de la baryte sont plus basse que celle de l'eau de mer au Cambrien moyen, ce qui donne à penser qu'une partie du Sr est dérivée du socle néoprotérozoïque sous-jacent. Les inclusions fluides dans la baryte lamellaire sont des inclusions riches en CO_2 et de faible salinité, leurs températures d'homogénéisation se situant entre 245 °C et 250 °C et leur salinité moyenne étant de 1,2 % équivalent NaCl en poids. Des pressions de piégeage minimums estimées de 1,7 kbar à 2,0 kbar ont été calculées à partir d'assemblages d'inclusions fluides aqua-carboniques. Les résultats obtenus des inclusions fluides reflètent la rééquilibration métamorphique régionale durant le métamorphisme régional subséquent, plutôt que les signatures des fluides primaires, malgré la préservation de textures primaires de la baryte et des inclusions fluides. Ces résultats illustrent le fait que la baryte dans les gisements SMV enregistre les processus physicochimiques associés à la formation des SMV et des sources de fluides dans les gisements de SMV anciens, ainsi que des compositions isotopiques du sulfate de l'eau de mer et du socle. Ces résultats sont pertinents non seulement pour le gisement Lemarchant, mais aussi pour d'autres gisements de SMV riches en baryte dans le monde. [Traduit par la Rédaction]

Mots-clés : sulfures massifs volcanogènes, baryte, isotopes de soufre, isotopes de strontium, Appalaches.

Introduction

Barite is a common gangue mineral in both ancient and modern volcanogenic massive sulphide (VMS) and seafloor massive sulphide (SMS) deposits (e.g., Hannington and Scott 1988; Hannington et al. 1991, 1995; Sharpe 1991; Sherlock et al. 1999; Scotney et al. 2005). Despite numerous barite-bearing VMS deposits globally, integrated field and microanalytical studies of hydrothermal barite have only recently been undertaken (e.g., Safina et al. 2016; Jamieson et al. 2016). The current model for the formation of hydrothermal sulphate–sulphide mounds involves mixing of ascending hot hydrothermal fluids with cold ambient seawater (Eldridge et al. 1983; Goldfarb et al. 1983; Ohmoto et al.

Received 23 June 2018. Accepted 12 February 2019.

M.-È. Lajoie and S.J. Piercey. Department of Earth Sciences, Memorial University of Newfoundland, St. John's, NL A1B 3X5, Canada.
J. Conliffe. Geological Survey of Newfoundland and Labrador, Department of Natural Resources, 50 Elizabeth Avenue, St. John's, NL A1B 4J6, Canada.
D. Layton-Matthews. Department of Geological Sciences and Geological Engineering, Queen's University, Kingston, ON K7L 3N6, Canada.
Corresponding author: Marie-Ève Lajoie (email: mlajoie@osiskomining.com).

1983; Ohmoto 1996). Barite ($BaSO_4$) typically precipitates during the early and late low-temperature growth stages of a mound when Ba-rich hydrothermal fluids mix with seawater, in which the latter is the primary source of SO_4^{2+} (Blount 1977). Although barite commonly forms the outer carapace of the sulphide mound (Blount 1977; Hanor 2000; Hannington and Scott 1988; Griffith and Paytan 2012), it has also been recorded in high temperature venting zones of chimneys where extensive mixing with seawater occurs (Hannington and Scott 1988; Hannington et al. 1991). Because of the extremely low solubility of barite in seawater and its resistance to diagenetic alteration, barite preserves the geochemical signatures associated with the ore-forming conditions during VMS formation (Eldridge et al. 1983; Kusakabe and Chiba 1983; Ohmoto et al. 1983; Watanabe and Sakai 1983; Paytan et al. 1993; Averyt and Paytan 2003). Thus, the geochemical and isotopic signatures of barite can provide insights into the origin and formation of sulphate-rich VMS deposits.

The polymetallic Zn–Pb–Cu–Ag–Au Lemarchant VMS deposit (hereafter referred to as the Lemarchant deposit), consists of two zones of mineralization (the Main and Northwest zones), and occurs within upper Cambrian felsic volcanic and volcaniclastic rocks of the Tally Pond Group, Newfoundland (approximately 513–509 Ma; Evans et al. 1990; Dunning et al. 1991; Evans and Kean 2002; Pollock et al. 2002). The Main zone of the Lemarchant deposit contains indicated resources of 1.24 Mt averaging 5.38% Zn, 0.58% Cu, 1.19% Pb, 1.01 g/t Au, and 59.17 g/t Ag, with inferred resources of 1.34 Mt averaging 3.70% Zn, 0.41% Cu, 0.86% Pb, 1.00 g/t Au, and 50.41 g/t Ag (as of March 2012; Fraser et al. 2012). The Northwest zone does not have a documented resource estimate. The Tally Pond Group also hosts other well-studied VMS deposits, such as the past-producing Duck Pond and Boundary deposits (combined resources of 4.08 Mt at 3.29% Cu, 5.68% Zn, 0.9% Pb, 59.3 g/t Ag, 0.9 g/t Au; Wagner 1993; Squires et al. 2001; Evans and Kean 2002; Squires and Moore 2004; Piercey et al. 2014; Buschette and Piercey 2016). The Lemarchant deposit differs from these other deposits of the Tally Pond belt as it contains more complex ore and gangue mineral assemblages, enrichments in precious metals, and mineral phases that are intimately associated with barite (Copeland et al. 2008; Fraser et al. 2012; Gill and Piercey 2014; Gill 2015; Gill et al. 2015, 2016).

Given the spatial relationship between barite and the mineralization at Lemarchant, understanding the formation of barite is critical for obtaining a full understanding of the deposit formation. Despite the presence of barite in the Lemarchant deposit, the detailed relationships of mineralization, textural variations, and genesis are not well understood. Herein, we present results from drill core logging, petrography, mineral chemistry, stable ($\delta^{34}S$) and radiogenic ($^{87}Sr/^{86}Sr$) isotope geochemistry, and fluid inclusion microthermometry. These data provide new insights into the conditions of barite formation and the sources of fluids and metals associated with the formation of the Lemarchant deposit. This contribution not only provides insight into barite-associated VMS deposits in the Appalachians but is also relevant to others studying barite-associated VMS deposits globally.

Regional and deposit scale geology and metallogenic framework

The Dunnage zone is host to many VMS deposits in the Newfoundland Appalachian Orogen (Swinden 1991) and examples include past producers (e.g., the Buchans, Duck Pond, and Tilt Cove deposits) and current producers (e.g., the Ming deposit). The Dunnage zone represents vestiges of Ediacaran to Ordovician arcs, back-arcs, and ophiolites that formed within the Iapetus Ocean (e.g., van Staal et al. 1998; Zagorevski et al. 2007; van Staal and Barr 2012). It is further subdivided into the peri-Laurentian affinity Notre Dame subzone and the peri-Gondwanan affinity Exploits subzones. (Figs. 1*a*–1*b*; Williams et al. 1988; Williams 1995; van Staal et al. 1998; van Staal and Barr 2012).

The middle Cambrian Tally Pond Group, central Newfoundland, consists of bimodal volcanic and volcaniclastic successions of mafic to felsic volcanic and volcaniclastic rocks of the Lake Ambrose (approximate U–Pb age of 513 Ma; Dunning et al. 1991) and Bindons Pond (approximate U–Pb age of 509 Ma; Pollock 2004) formations. Together, these formations form the base of the Victoria Lake supergroup, which is part of the Exploits subzone (e.g., Rogers and van Staal 2002; Rogers et al. 2006, 2007; McNicoll et al. 2010; Piercey and Hinchey 2012). The Neoproterozoic (approximately 565 Ma; Evans et al. 1990) arc-related Crippleback Lake plutonic suite underlies the Tally Pond Group and is interpreted to be peri-Gondwanan, Ganderian basement to the group (Fig. 2; van Staal et al. 2002; Rogers et al. 2006).

The Lemarchant deposit is hosted within the upper section of the Bindons Pond Formation (Figs. 1*a*–1*b*; Fig. 2). These bimodal volcanic successions have arc-like geochemical signatures (e.g., transitional Zr/Y ratios of 2.8–4.5, upper crust normalized La/Sm ratios <1, negative Nb, Ti, and Eu anomalies; Piercey et al. 2014) and are interpreted to have formed during the onset of Cambrian arc rifting on the leading edge of Ganderia (Dunning et al. 1991; Rogers et al. 2006, 2007; Piercey et al. 2014; Buschette and Piercey 2016; Cloutier et al. 2017), and were accreted to the Ganderian margin during the Ordovician Penobscot orogeny (Colman-Sadd et al. 1992; Zagorevski et al. 2010). Post-Penobscot orogeny rifting and back-arc development occurred along the leading edge of Ganderia and along the edge of composite Laurentia. This resulted in a Molluscan Sea-type subduction environment that, upon closure, resulted in the latest Ordovician accretion of the Notre Dame and Exploits subzones to one another along the Red Indian Line (i.e., Taconic 3 of Zagorevski and van Staal 2011 and van Staal and Barr 2012). This was followed by the closure of the Exploits–Tetagouche back-arc basin and suturing of the remnants of Ganderia to composite Laurentia during the Silurian Salinic orogeny (Figs. 1*a*–1*b*; Dunning et al. 1990; van Staal 2007; Zagorevski et al. 2007; van Staal and Barr 2012). These latter orogenic events were responsible for thrusting, deformation, and greenschist facies metamorphism of the Tally Pond belt, resulting in a northeast-trending structural grain, east–northeast-striking faults, and minor regional folds (Dunning et al. 1991; Evans and Kean 2002; Rogers et al. 2006). Despite deformation and metamorphism, primary volcanic and sulphide structures and textures are well-preserved within the Lemarchant and other deposits of the Tally Pond belt (e.g., Piercey et al. 2014; Cloutier et al. 2017) and provide insight into primary volcanic and hydrothermal processes.

Deposit geology

The Lemarchant deposit contains two main mineralized zones, the Lemarchant Main zone and the Northwest zone, as well as and three other target areas (i.e., the North, the South, and the 24 zones) (Fig. 3). The Lemarchant thrust fault repeats the host stratigraphy and has displaced part of the main sulphide lens (Copeland et al. 2008; Fraser et al. 2012; Cloutier et al. 2017). The structure, lithostratigraphy, alteration, and mineralogy of the Lemarchant deposit has been the subject of numerous recent studies (Gill et al. 2016; Cloutier et al. 2017; and references therein) and will only be summarized here. The Main zone of the Lemarchant deposit is hosted by moderately to strongly altered felsic volcanic rocks that have distinct lithological assemblages (*Sequences 1 to 4* of Cloutier et al. 2017). The base (*Sequence 1*) consists of mafic to intermediate volcano-sedimentary lithofacies dominated by tuffs, poorly sorted breccias, and lapilli tuffs. This is conformably overlain by (*Sequence 2*) volcaniclastic rocks dominated by poorly sorted polymict breccias, tuffs, and lapilli tuffs (Fig. 4). Rocks immediately below mineralization are bimodal (*Sequence 3*), with the base of the sequence dominated by andesite that grades upwards into dacite (Fig. 4). Both the andesite and dacite sequences consist

Fig. 1. (*a*) Simplified tectonostratigraphic zones of the Newfoundland Appalachians. The red rectangle indicates the location of the study area located in the Exploits subzone of the Dunnage zone, east of the Red Indian Line. (*b*) Geologic map of the Victoria Lake supergroup and adjacent areas, including the Tulks volcanic belt, the Tally Pond Group, and the Cripplebach Intrusive Suite/Sandy Brook Formation. The Tally Pond Group, in which the Lemarchant deposit is located, is defined by the area within the red rectangle. The Tally Pond Group also hosts the Duck Pond and Boundary deposits, indicated by the red circles. RIL, Red Indian Line; TPB, Tally Pond; TVB, Tulks volcanic belt; CLIS, Cripplebach Intrusive Suite; VLIS, Valentine Lake intrusive suite; VLSZ, Victoria Lake Shear Zone. Diagram modified from McNicoll et al. 2010. [Colour online.]

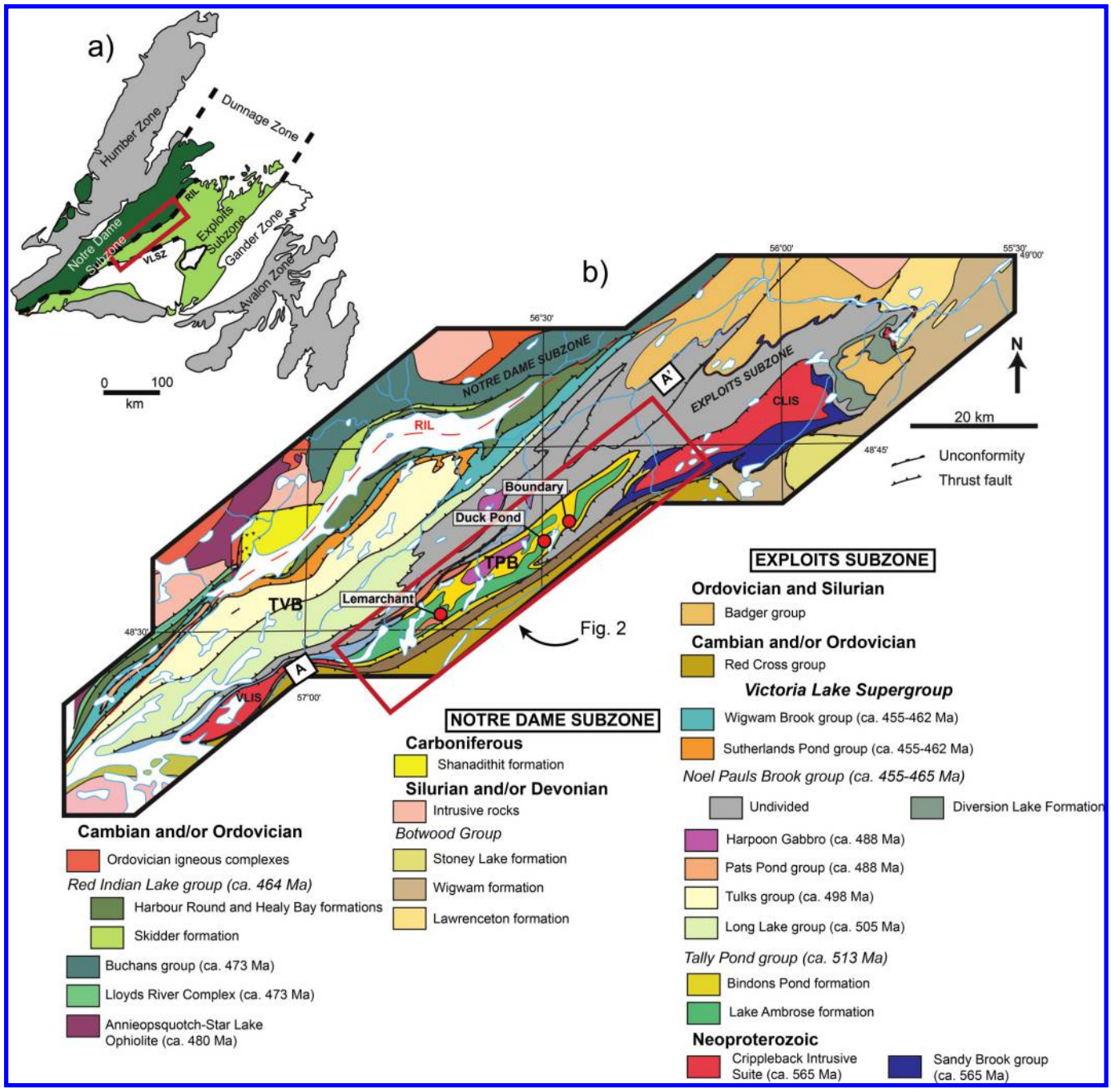

of poorly sorted monomictic breccias and flows, interpreted to have been deposited in a vent-proximal setting (Cloutier et al. 2017). Veinlets of sphalerite, chalcopyrite, quartz, carbonate, and chlorite cross-cut the monomictic breccia of this sequence. The hanging wall consists predominantly of massive to pillowed submarine mafic rocks and basaltic andesite (*Sequence 4*), which are weakly altered and generally barren of mineralization (Fig. 4). The stratiform mineralized zone occurs at the contact between the relatively unaltered hanging wall (*Sequence 4*) and the strongly altered footwall (*Sequence 3*) and consists of massive sulphide and barite, which is immediately overlain by a pyritic to carbonaceous mudstone (Figs. 4–6). Graphic logs of the typical stratigraphic sequence of the mineralized lenses are illustrated in Fig. 5 (Main zone) and Fig. 6 (Northwest zone).

Numerous intrusions pre-date and cross-cut the Lemarchant deposit. Felsic dikes cross-cut the Lemarchant stratigraphy and

Fig. 2. Detailed geologic map of the Tally Pond Group and the locations of U–Pb geochronological studies (McNicoll et al. 2008). Diagram modified from McNicoll et al. 2008, 2010; Squires and Hinchey 2006; Rogers et al. 2006. [Colour online.]

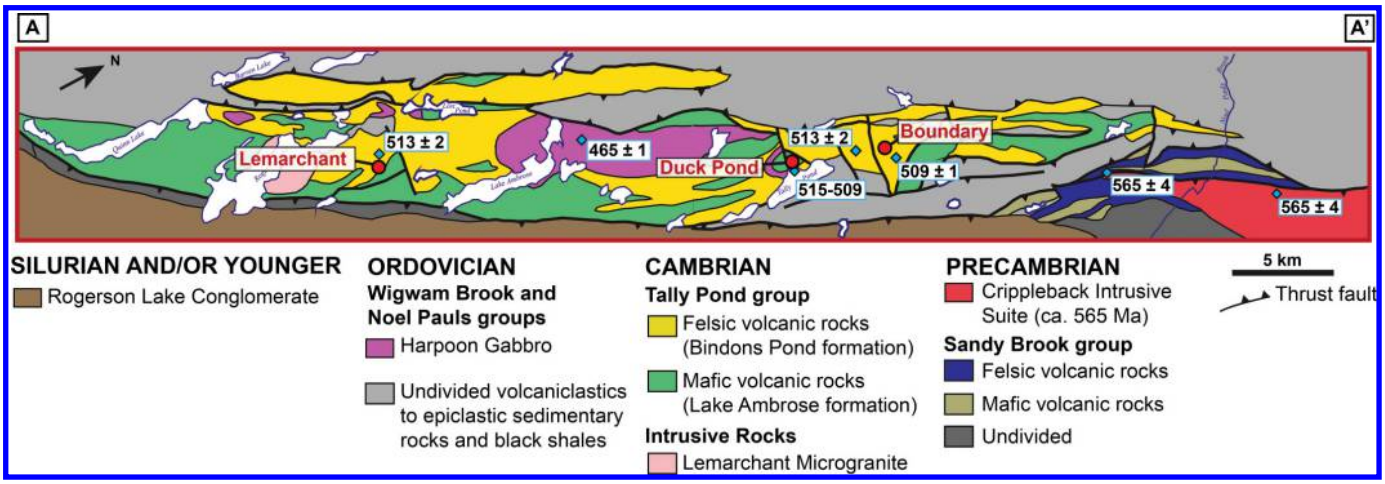

Fig. 3. Simplified geologic map of the Lemarchant deposit with drill hole locations. Drill holes represented by red circles are those that contain barite mineralization. The bimodal nature of the Lemarchant deposit is illustrated by the felsic volcanic footwall and the mafic volcanic hanging wall. The Lemarchant microgranite is located 500 m northwest of the mineralized zone. The Lemarchant fault strikes north–south and is indicated by the black line in the center. Surface projection of indicated and inferred resources are shown and are represented by the dark and light purple colors (Main zone). The surface projection of the mineralization in the Northwest zone is represented by the red polygon located near the Northwest zone. Modified after Fraser et al. (2012). [Colour online.]

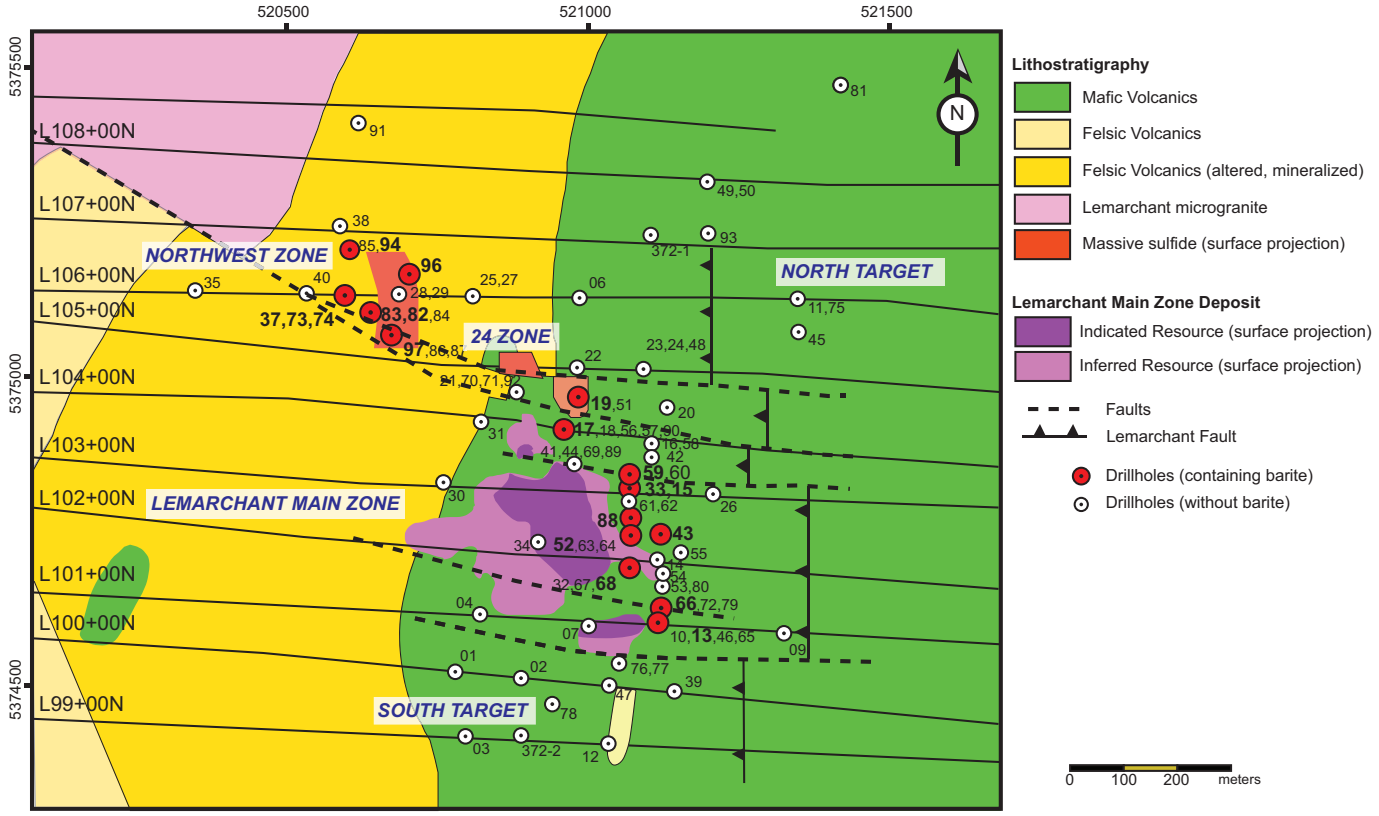

occur spatially associated in or adjacent to shear zones but are likely coeval with the volcanic rocks in the deposit (Cloutier et al. 2017). The Lemarchant microgranite is located approximately 500 m northeast of the Lemarchant deposit and cross-cuts the entire Tally Pond Group. This granite contains hydrothermal alteration and has geochemical similarities with rocks of the Lemarchant deposit, suggesting that it is a subvolcanic intrusion to the Tally Pond Group (Squires and Moore 2004). Late gabbro dikes and sills cross-cut all volcanic sequences in the Lemarchant deposit, including mineralization, and are interpreted to be equivalent to the approximately 465 Ma Harpoon Hill gabbro (Pollock 2004; Squires and Moore 2004).

Mineralization and alteration

The Main and Northwest zones are both hosted in the Bindons Pond Formation felsic volcanic rocks and are separated by a

Fig. 4. Schematic cross-sections of sections 103+00N (Main zone) and 106+00N (Northwest zone) of the Lemarchant deposit illustrating the mineralized zones and their relationship to the mafic-dominated hanging wall and the felsic-dominated footwall. Drill holes are represented by the thin solid black lines. Drill holes represented by red circles are those that contain barite mineralization. Modified after Fraser et al. (2012). [Colour online.]

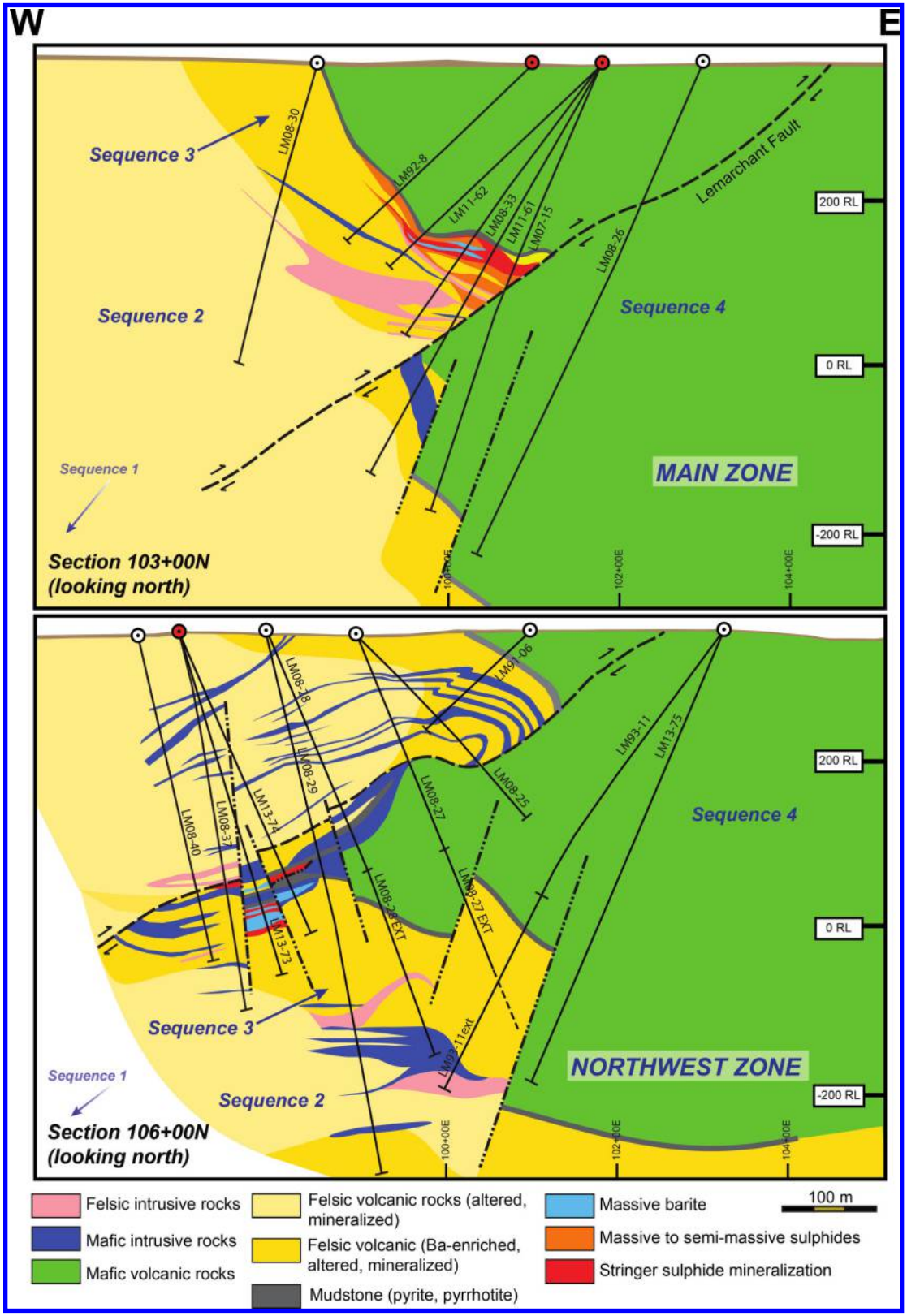

Fig. 5. Graphic logs of sections 103+00N to 102+50N intercepting the Main zone of the Lemarchant deposit. Barite units are interpolated between the drill holes. Barite is spatially associated with mineralization and occurs between a metalliferous mudstone unit above and altered felsic volcanic rocks below. [Colour online.]

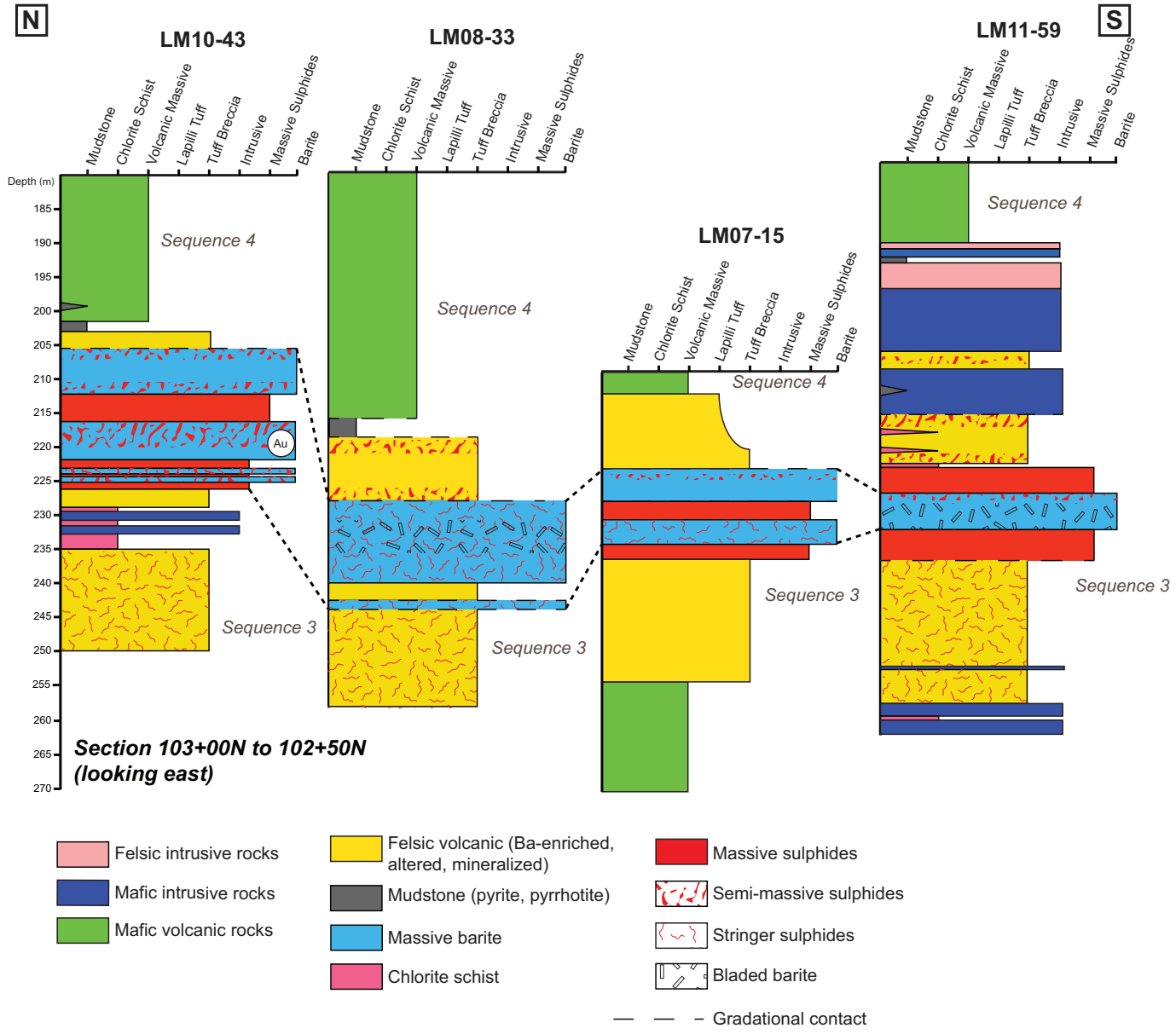

complex structural zone. Cloutier et al. (2017) suggested that the Main and Northwest zones represent two distinct mineralized lenses that were stacked due to deformation (likely associated with the 486–478 Ma Penobscot orogeny), and not separate parts of a continuous massive sulphide lens (cf. Fraser et al. 2012). Nevertheless, stratigraphic relationships in the Main and Northwest zones are similar. In general, the Lemarchant Main zone has mineral and metal zoning that consists of an upper stratiform zone consisting of a barite cap enriched in precious metals that grades inwards to a Zn–Pb semi-massive to massive sulphide-rich zone, which is underlain by a sulphide-bearing stringer composed predominantly of chalcopyrite and pyrite with lower base and precious metal grades (Gill et al. 2015, 2016); this zonation is typical of bimodal felsic/Kurko-type VMS deposits (e.g., Eldridge et al. 1983; Ohmoto 1996).

Hydrothermal alteration in the Lemarchant deposit consists predominantly of pervasive quartz and sericite in the felsic-dominated footwall and within the mineralized zone with local zones of intense chlorite alteration; a zone of intense black chlorite alteration is regularly found below the massive sulphide lenses (Squires and Moore 2004; Copeland et al. 2008*a*, 2008*b*). The weaker alteration in the mafic-dominated hanging wall consists of quartz–epidote–Mn–carbonate. Quartz–carbonate vein networks are abundant throughout the deposit and often contain Fe–carbonate. The surrounding wall rocks are locally altered to Fe–carbonate, mostly as spots and patches with local intense zones (Gill et al. 2016).

The mineralization at Lemarchant has a complex paragenesis (Fig. 7). Gill et al. (2016) identified five distinct mineral assemblages that reflected the paragenetic evolution of the deposit, related to three stages of mineralization (stages 1, 2, and 3, from oldest to youngest). During stage 1, metals were interpreted to be transported by low temperature (100–275 °C), oxidized hydrothermal fluids, and were dominated by barite intergrown with low-Fe sphalerite (<1 mol.% FeS; Gill et al. 2016), galena, and trace chalcopyrite in the upper stratiform zone. The mineral assem-

Fig. 6. Graphic logs of section 106+00N intercepting the Northwest zone of the Lemarchant deposit. Barite units are interpolated between the drill holes. Barite is spatially associated with mineralization and mafic dikes are abundant throughout the mineralized zone. [Colour online.]

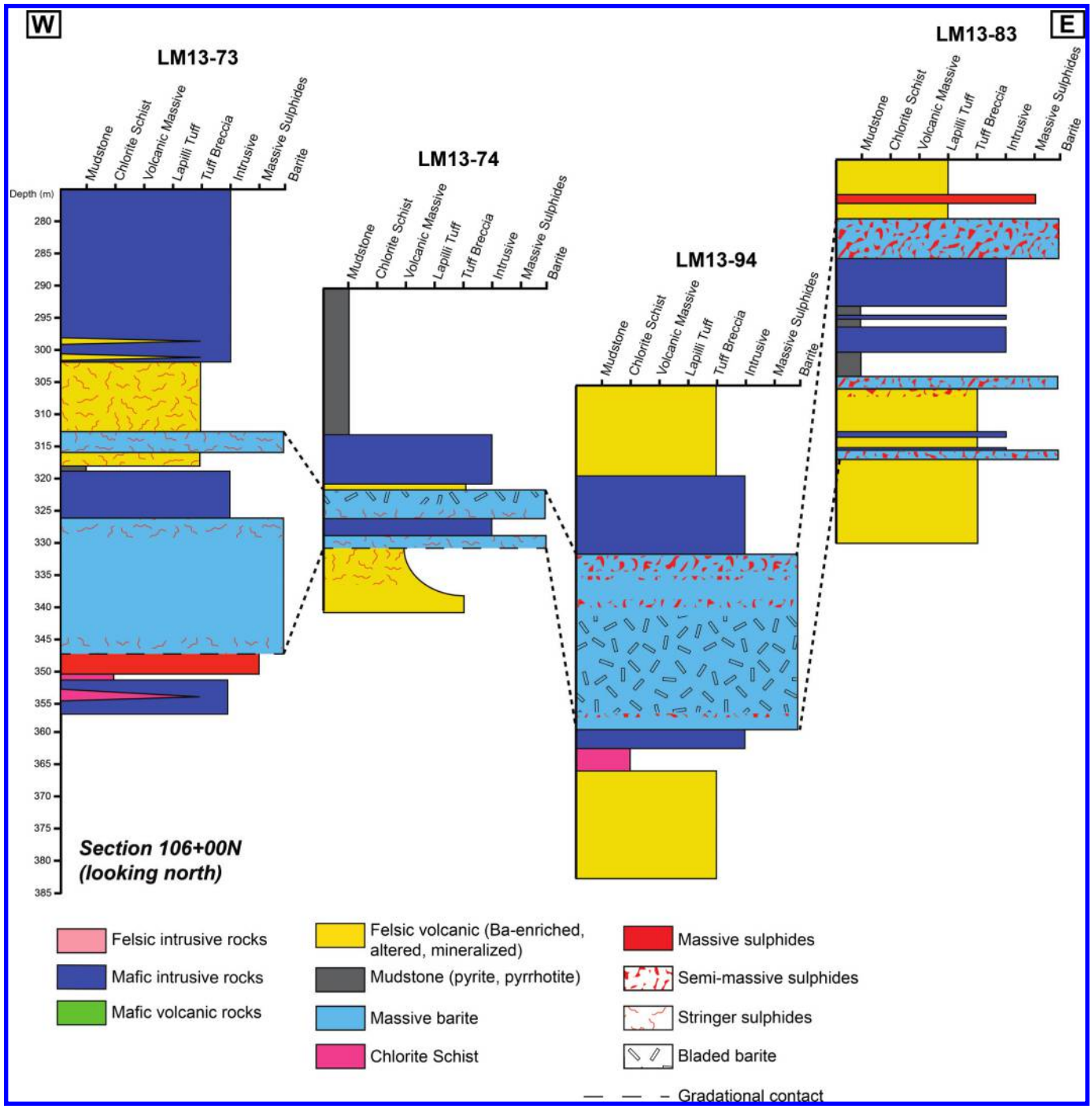

blages associated with the stage 2 mineralization consist of assemblage 2A dominated by bornite, tetrahedrite, covellite, and colusite (Cu–Au-dominated) and assemblage 2B dominated by an electrum and sulphosalt-rich assemblage (e.g., tetrahedrite-group minerals). Due to the complex intergrowth of both mineral assemblages, assemblages 2A and 2B likely precipitated simultaneously under similar physicochemical conditions. Stage 2 mineralization is enriched in epithermal-suite elements (i.e., As, Bi, Cr, Co, In, Mo, Ni, Sb, Se, Te, and Au), particularly in the upper parts of the mineralized lens associated with bladed barite (Gill et al. 2015, 2016). The precious metal and epithermal suite enrichment of stage 2 mineralization observed is interpreted to have formed at low temperatures (150–275 °C; Scott and Barnes 1971; Hannington and Scott 1988; Huston and Large 1989) and shallow water depths (<1500 m below sea level; Sillitoe et al. 1996; Hannington and Monecke 2009). The presence of gold and sulphosalt phases with bladed barite led Gill et al. (2015, 2016) to suggest that intermittent boiling events and magmatic fluids may have contributed to the formation of stage 2 mineralization. Stage 3 mineralization consists of Fe-rich sphalerite (4.7–13.6 mol.% FeS; Gill et al. 2016), chalcopyrite, and pyrite, and is interpreted to represent higher temperature mineralization (>300 °C). This late stage of mineralization forms the basal stringer sulphide zone.

Fig. 7. Simplified mineral paragenetic sequence diagram for the three main stages of mineralization of the Lemarchant deposit and the associated mineral assemblage types based on the work of Gill et al. (2015). Approximate temperature ranges for different minerals are based on temperature measurements from vent fluids, fluid inclusions, and thermodynamic equilibria (Hannington and Scott 1988; Paradis et al. 1988; Koski et al. 1994; Drummond and Ohmoto 1985). Modified from Gill et al. (2015). [Colour online.]

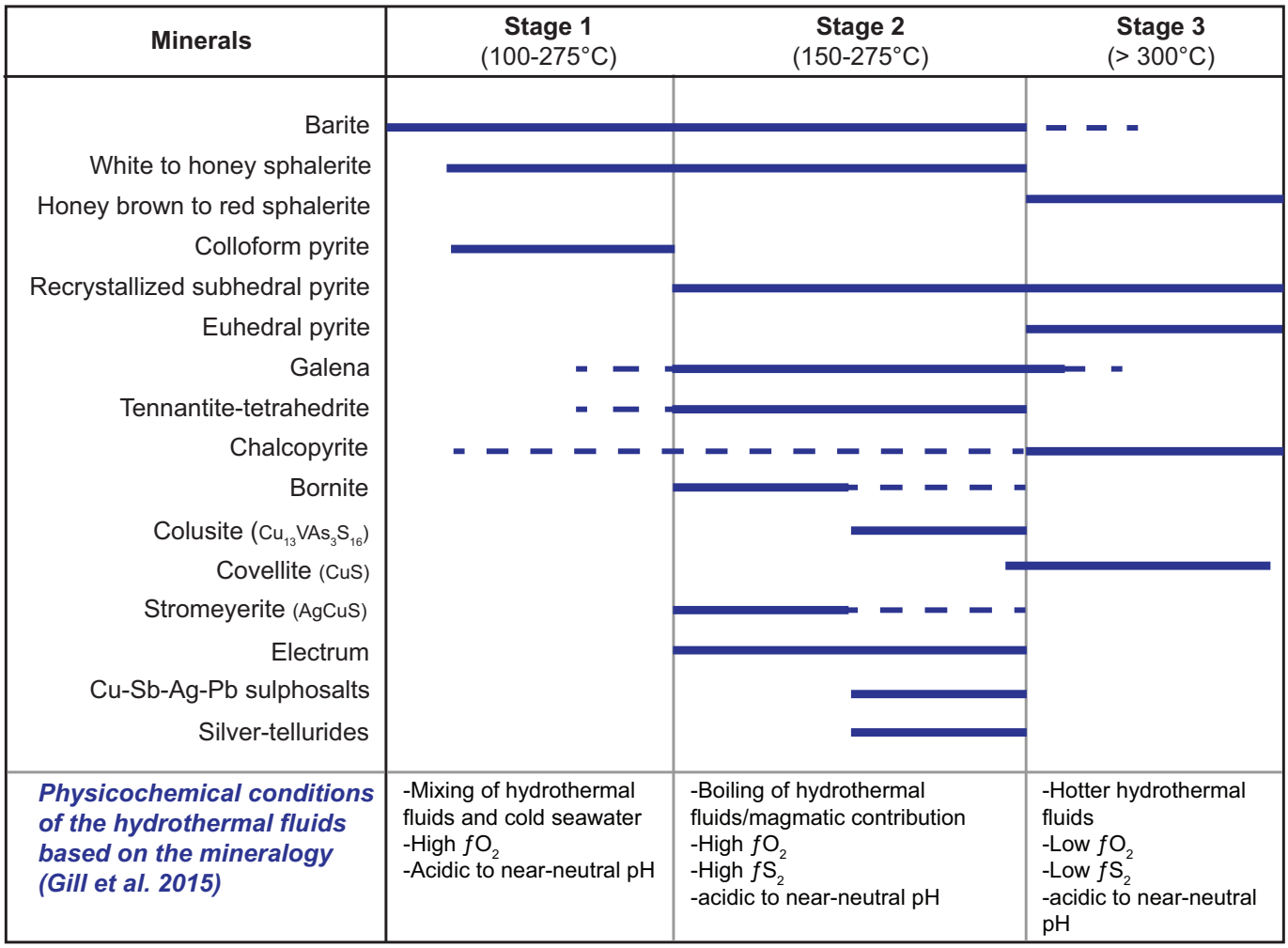

Analytical methods

Sampling and petrographic analysis

Drill holes containing barite units were logged to document textural and mineralogical relationships (see Supplementary Fig. S1[1] for log descriptions and sample locations). Samples were selected for thin sections and subsequent analytical work based on textural and mineralogical relationships (Table 1). Thin sections were studied using standard reflected and transmitted light microscopy and scanning electron microscopy (SEM); SEM was used for the identification of unknown mineral phases and precious metal phases. An FEI (Hillsboro, OR, USA) Quanta 650 SEM equipped with a field emission gun and silicon drift detectors was utilized for collection of both back-scatter electron images, and semiquantitative elemental maps derived from energy dispersive X-ray spectra (EDS) and were processed using Bruker (Billerica, MA, USA) Espirit software (v. 1.9).

Electron microprobe analysis

Major element concentrations of individual barite crystals were determined by electron probe microanalysis (EPMA). Twenty-one thin sections were analyzed for eleven elements (Ba, S, Sr, Na, Si, Ca, K, Fe, Zn, Pb, and F) on different barite textures using a five-spectrometer JEOL (Peabody, MA, USA) JXA-8230 electron microprobe at Memorial University, Newfoundland, Canada. The analyses were conducted at an accelerating voltage of 15 kV and intensity of 20 nA using a spot size of 1 μm. The X-ray takeoff angle was 40 degrees. Count times for elements varied between 10–30 s with off-peak count times set to equal half the peak count times. Element concentrations were determined using lithium fluoride (LIF), pentaerythritol (PET), and thallium acid phthalate (TAP) crystals. Natural and synthetic mineral phases were used as calibration standards. The standards and lines used were as follows: (1) SPI (SPI Supplies, West Chester, PA, USA) synthetic compound group $BaSO_4$ (BaLα on LIF); and (2) Astimex mineral suite, including: pyrite (SKα on PET), celestite (SrKα on PET), albite (NaKα, SiKα on TAP), bustamite (CaKα on PET), orthoclase (KKα on PET), almandine garnet (FeKα on LIF), willemite (ZnKα on LIF), and galena (PbKα on PET). Quality control was maintained by using a secondary standard (BaF_2; obtained from SPI Supplies). The secondary standard was measured at the beginning and end of each round and the measured values were in compliance with the accepted concentrations in this standard. Major element precision was gen-

[1]Supplementary data are available with the article through the journal Web site at http://nrcresearchpress.com/doi/suppl/10.1139/cjes-2018-0161.

Table 1. Sample descriptions of barite samples used in this study and associated analytical methods, Lemarchant deposit, Newfoundland.

Sample number	Drill hole	Depth (m)	Mineralized zone	General sample description	Analysis method		
					LA–ICP–MS	EPMA	Fluid inclusion microthermometry
CNF31721	LM13-73	333	Northwest zone	Bladed white barite and granular barite separated by a late cross-cutting carbonate vein.		✓	
CNF31723	LM13-73	346.5	Northwest zone	Massive granular barite cross-cut by a white, milky carbonate/barite vein associated with chalcopyrite clusters.		✓	✓
CNF31730	LM13-94	332.3	Northwest zone	Dark granular barite with muscovite in interstitial spaces with chalcopyrite clusters/ disseminations.		✓	
CNF31733	LM13-94	341.4	Northwest zone	Bladed, white barite crystals within a darker, granular barite matrix cross-cut by chalcopyrite stringers.		✓	
CNF31735	LM13-94	346.2	Northwest zone	Interlocking barite blades with interstial granular barite crystals. No stringers.	✓	✓	
CNF31809	LM10-43	213.7	Main zone	Semi-massive sulphide mineralization with bladed to colloform(?) barite.	✓	✓	
CNF31810	LM10-43	218.8	Main zone	Large, euhedral, white bladed barite within an interstitial granular barite matrix.		✓	
CNF31811	LM10-43	209.9	Main zone	Sharp contact between darker granular barite and white, bladed barite with visible gold mineralization.		✓	
CNF31812	LM10-43	226.1	Main zone	White, bladed barite clusters within a semi-massive sulphide and granular barite matrix (10%–15% sulphides).	✓	✓	
CNF31816	LM08-19	98.1	Main zone	Contact between jasper and massive granular barite.	✓	✓	
CNF31818	LM08-19	6.5	24 zone	Felsic volcanic lapilli tuff with thinly bladed barite clusters.		✓	
CNF31847	LM13-83	300.2	Northwest zone	Pyrrhotite-rich mudstone with layered white barite cross-cut by a late euhedral pyrite-rich vein.	✓	✓	
CNF31855	LM11-52	216.2	Main zone	Contact between granular barite and white barite irregular clusters.		✓	
CNF31860	LM11-68	198	Main zone	Bladed/large colloform barite within a darker, granular barite matrix.	✓	✓	✓
CNF31861	LM11-68	200	Main zone	White bladed barite adjacent to darker layered granular barite.	✓	✓	
CNF31865	LM14-96	309.9	Northwest zone	Contact between dark purple/blue massive barite and white thinly bladed barite.	✓	✓	✓
CNF31868	LM14-96	314.3	Northwest zone	White bladed barite within a darker granular barite matrix.		✓	
CNF31874	LM13-82	340.8	Northwest zone	White, bladed barite crystals within a granular barite matrix. Presence of pyrite and chalcopyrite clusters.	✓	✓	✓
CNF31875	LM13-82	342.2	Northwest zone	Large, irregular, monolithic rhyolite clasts with white bladed barite filling interstitial space between felsic clasts.	✓	✓	
CNF31877	LM11-66	164.4	Main zone	Dark granular barite in interstitial space between puzzle-fit felsic clasts.		✓	
CNF31879	LM08-37	297.9	Main zone	Bladed white barite clast and irregular rhyolite clast within a massive sulphide matrix composed primarily of honey sphalerite and pyrite. Chalcopyrite surrounds barite clast.		✓	

Note: EPMA, electron probe microanalysis ; LA–ICP–MS, laser ablation inductively coupled plasma mass spectrometry.

erally better than 1% (1σ); however, precision was reduced for minor elements. The analytical totals were accepted if they fell within a range of 100 ± 1.5 wt.%.

Laser ablation quadrupole inductively coupled plasma mass spectrometry (LA–ICP–MS)

Fourteen of the 21 barite samples analyzed by EMPA were analyzed for 57 elements using a ThermoFisher (Waltham, MA, USA) X-series 2 quadrupole ICP–MS coupled to an ESI (Portland, OR, USA) NWR-193 nm Excimer laser system at Queen's Facility for Isotope Research (QFIR), Kingston, ON, Canada. Thin section samples containing different barite textures and standards were affixed in the laser chamber using mounting putty. Barite crystals were ablated at 100% power using a repetition rate of 20 Hz and focused laser beam of 50 μm. Gas blanks were analysed for 30 s between each sample analysis. The ablation speed was 5 μm/s with a fluence of approximately 5 J/cm^2. United States Geological Survey (USGS) glass standards (GSC-1G, GSD-1G, and GSE-1G; Jochum et al. 2005) were used as external calibration at the begin-

ning and end of every round and the measured values were in compliance with the accepted concentrations in this standard. The K-0253 standard glass (SPI Supplies) was used as a reference material for Ba at the beginning and end of each run, and the BHVO-2G standard (Jochum et al. 2005) was used as an unknown once every ten sample analyses to monitor instrument drift, correct for changes in element ionization, and assess data quality. All analyses were within ± 5% error of the certified elemental values for BHVO except for Ti and In, which had a precision of 10% and 93%, respectively (Table B1). Quantitative results were obtained through external calibration and normalisation of each analysis to Sr contents of the barites as determined by electron probe analysis. The whole suite of trace elements, rare earth elements (REE), and base metal elements were measured using the quadrupole–ICP–MS.

Whole-rock Sr isotopes ($^{87}Sr/^{86}Sr$)

Whole-rock major, trace, and REE concentrations were determined for 10 of the 18 samples analyzed for Sr isotope geochemistry (Tables A1 and A2). Samples were crushed and sieved to <80 μm and centrifuged to isolate barite. Samples were analysed by inductively coupled plasma mass spectrometry (ICP–MS) at Activation Laboratories Inc., ON, Canada, using the 4B2-Research-Lithium Metaborate/Tetraborate Fusion-ICP/MS package that involves lithium metaborate/tetraborate fusion and HNO_3 dissolution. Lithogeochemical analyses of these samples were determined prior to Sr isotope analyses to determine the concentrations of Sr and Rb.

Whole-rock Sr isotope ($^{87}Sr/^{86}Sr$) compositions of crushed barite samples that contained mixed textures (bladed and granular) were acquired using a standard step leaching process to eliminate impurities. Approximately 50 mg of crushed barite was placed in 15 mL beakers and 7N HNO_3 was added to cover each sample. The beakers were removed from the hot plate after two hours and left covered for two days to allow the sample material to settle to the bottom of the beaker. The acid was removed with a pipette from each beaker and this process was repeated three times. The samples were then left on a hot plate to evaporate to ensure that barite samples were dry and no HNO_3 remained. Each sample was then submersed in 6N HCl, covered, and subsequently placed on hot plates at 100 °C for three days. The 6N HCl was pipetted from the beakers and the barite samples were left to dry overnight. Approximately 1.5 mL of 2.5N HCl was added to each beaker and the samples were left covered for two days. After leaching procedures, the samples were run through Sr resin columns to isolate the strontium dissolved barite solutions.

Whole-rock strontium isotope ($^{87}Sr/^{86}Sr$) ratios were determined for the samples using a Finningan MAT (San José, CA, USA) 262V thermal ionization mass spectrometer (TIMS) in dynamic mode at Memorial University, Newfoundland, Canada. Instrumental mass fractionation of Sr isotopes was corrected using a Rayleigh law relative to $^{88}Sr/^{86}Sr = 8.375209$. The reported $^{87}Sr/^{86}Sr$ ratios were corrected for the deviation from repeated duplicates of the NBS 987 standard ($^{87}Sr/^{86}Sr = 0.710240$, Veizer et al. 1999). Replicates of the standard gave an average of $^{87}Sr/^{86}Sr = 0.710245 \pm 000011$ ($n = 23$).

Sulphur isotopes ($\delta^{34}S$)

A total of 23 barite samples from various zones of the deposit (see above) were analyzed for sulphur isotope geochemistry: (1) granular purple-grey barite (associated with stage 1 mineralization; $n = 5$); and (2) bladed white barite (associated with stage 2 mineralization; $n = 18$). For each sample, barite was drilled out using a hand-held microdrill. The microdrill was cleaned with acetone between each sample to eliminate sample contamination. Approximately 0.35 mg of drilled mineral separate was used for analysis, with analyses undertaken on a Finnigan MAT252 isotope ratio mass spectrometer (IRMS) at Memorial University, Newfoundland, Canada. Stable isotope results are reported in standard (δ) notation as per mil (‰) relative to the Vienna Canyon Diablo Troilite (V-CDT), with an analytical uncertainty of ±0.4‰ (1σ) (A. Pye, personal communication, 2016). Standards IAEA-S-2 (+22.67 ± 0.15 $\delta^{34}S_{VCDT}$) and IAEA-S-3 (−32.55 ± 0.12 $\delta^{34}S_{VCDT}$) were used for isotope calibration and standards IAEA-S-1 (−0.30 (exact) $\delta^{34}S_{VCDT}$), NBS-127 (+21.1 ± 0.36 $\delta^{34}S_{VCDT}$), and (or) IAEA-SO-5 (+0.49 ± 0.11 $\delta^{34}S_{VCDT}$) were used as check (unknown) standards for quality control. Duplicate analyses during the course of the study illustrated that bulk samples had maximum internal variations of <0.85‰.

Fluid inclusion microthermometry

Four samples were analyzed for fluid inclusion microthermometry (e.g., Table 1). The selected samples were from the Main zone and Northwest zone of the Lemarchant deposit. Fluid inclusion samples were selected based on the presence of abundant and well-preserved fluid inclusion assemblages (FIAs) in bladed barite hosted within the massive sulphide lenses. Additionally, one sample was selected from a barite-rich vein. Samples were prepared as approximately 100 μm doubly-polished thin sections mounted with acetone-soluble glue (cyanoacrylate). Prior to microthermometric measurements, a detailed petrographic examination of the samples was completed to identify FIAs and classify fluid inclusion types. The barite was removed from the glass backing prior to heating and freezing experiments by immersing the polished thick section in acetone overnight. The general method for heating/freezing experiments followed the procedure of Roedder (1984) and Shepherd et al. (1985). Measurements were completed at Memorial University, Newfoundland, Canada, using a Linkam (Linkam Scientific, Tadworth, UK) THMSG600 heating freezing stage mounted on an Olympus (Center Valley, PA, USA) BX51 microscope equipped for use with reflected, transmitted, and infrared light. Fluid inclusion images were captured using an Olympus DP71 camera. The accuracy and precision of measurements was insured by calibration against the triple point of CO_2 (−56.6 ± 0.1 °C), the freezing point of water (0.0 ± 0.1 °C), and the critical point of water (374.6 ± 0.5 °C) using SYNFLINC synthetic fluid inclusions. Barite is particularly susceptible to leakage and necking-down processes (Ulrich and Bodnar 1988); therefore, fluid inclusions near cracks or showing necking-down or leakage were not analyzed.

Salinities of aqueous–carbonic fluid inclusions were calculated using the *Q2* program within the software package CLATHRATES (Bakker et al. 1996; Bakker 1997, 1998). Salinities were calculated for all analysed inclusions that contain a coexisting liquid and vapor gas phase (CO_2) using the temperature of clathrate melting. Pressure (bars) for fluid inclusion assemblages were calculated using the *Q2* program within the software package Loner15 and calculated from homogenization temperatures (T_h) of aqueous carbonic inclusion assemblages (Bakker 1997; Bakker and Brown 2003). Isochores for type-I fluid inclusion assemblages were calculated using the FLUIDS software package and the equation of state reported by Anderko and Pitzer (1993) and Duan et al. (1995) (Table C2). Bulk fluid compositions calculated from the Loner15 software and T_h of the FIAs were used to calculate the isochores on a pressure–temperature diagram.

Results

Petrographic and microtextural features of barite

Barite is spatially associated with massive sulphides and occurs in layers approximately 2–30 m thick (Fraser et al. 2012) with variable textures. Granular barite is medium- to fine-grained, consisting of 1–50 μm, dark grey-blue crystals that are associated with white to honey-coloured sphalerite, pyrite, galena, and minor chalcopyrite and tetrahedrite–tennantite (stage 1; Figs. 8A–8B). Bladed/tabular barite occurs as euhedral blades (up to 0.5 cm in

Fig. 8. Drill core images showing the different barite textures and associated stages of mineralization (Gill et al. 2015). (A) Bladed barite in a granular baritic matrix of stage 1 mineralization (sample CNF31804 from drill hole LM11-59, depth: 227.6 m). (B) Granular barite associated with stage 1 mineralization with localized areas of bladed barite, milky carbonate, and chalcopyrite clusters (sample CNF31830 from drill hole LM07-15, depth: 232 m). (C) Stage 2A mineralization (bornite, covellite, chalcopyrite, and galena) associated with localized areas of bladed barite overprinting disseminated sulphides from stage 1 mineralization (sample CNF31809 from drill hole LM10-43, depth: 213.7 m). (D) Sharp contact between bladed barite associated with stage 2B mineralization and granular barite associated with stage 1 mineralization. Visible electrum (stage 2B) is present in bladed barite (sample CNF31811 from drill hole LM10-43, depth: 210 m). (E) Stage 3 mineralization composed dominantly of pyrite and minor chalcopyrite (zone refining) overprinting stage 1 mineralization in a chaotic granular barite–dolomite matrix (from drill hole LM13-83, depth: 280 m). (F) Granular barite associated with stage 1 mineralization (disseminated low-Fe sphalerite, galena, and pyrite), cross-cut by a white, euhedral barite vein associated with stage 3 mineralization (dominantly chalcopyrite) (sample CNF31723 from drill hole LM13-73, depth: 346.5 m). (G) Stage 3 pyrite-rich vein cross-cutting the overlying laminated metalliferous mudstone unit (sample CNF31847 from drill hole LM13-83, depth: 300.2 m). (H) Stage 3 mineralization (high-Fe sphalerite, pyrite, and granular barite) within interstitial spaces of felsic volcanic blocks in the footwall stockwork zone (sample CNF31854 from drill hole LM13-88, depth: 214.5 m). Au, gold; Brt, barite; Dol, dolomite; Py, pyrite. [Colour online.]

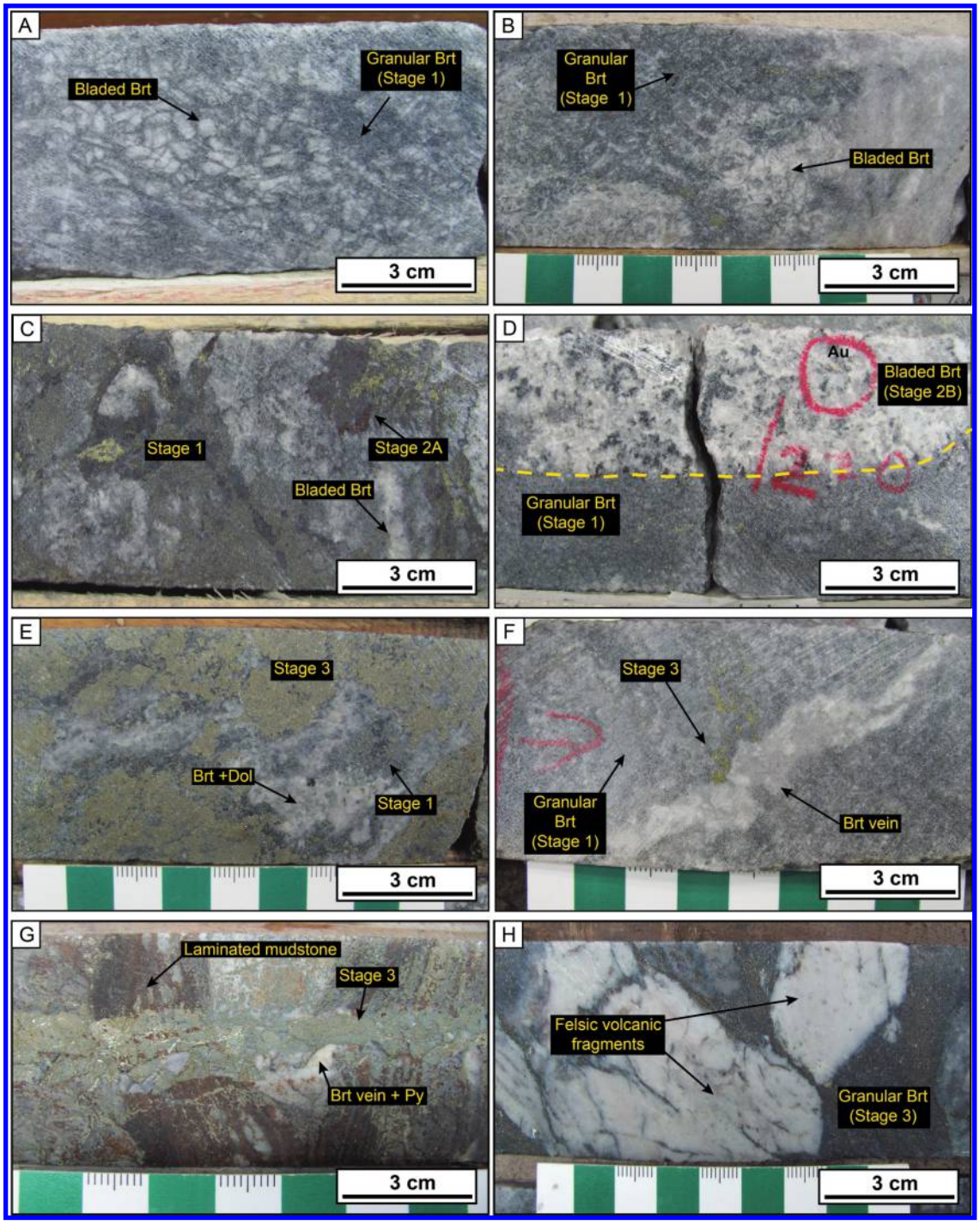

Fig. 9. Cross-polarized and reflected images of thin sections of the different barite textures found at the Lemarchant deposit. (A) Cross-polarized image showing localized radiating barite laths from central subhedral, rounded barite clusters (sample CNF31803 from drill hole LM11-59, depth: 226.6 m). (B) Cross-polarized image showing plumose barite crystals adjacent to small, subhedral, interlocking granular barite grains (sample CNF31860 from drill hole LM11-68, depth: 198 m). (C) Cross-polarized image showing randomly oriented large tabular barite laths with carbonate material filling interstitial spaces between barite crystals (sample CNF31863 from drill hole LM11-68, depth: 203.4 m). (D) Cross-polarized image showing bladed barite with interstitial granular barite between barite blades (sample CNF31860 from drill hole LM11-68, depth: 198 m). (E) Reflected image showing bladed crystals of barite. The matrix interstitial to the barite blades is composed of smaller, granular barite grains and sulphides such as sphalerite, galena, and pyrite (sample CNF31849 from drill hole LM13-83, depth: 304.4 m). (F) Large tabular laths of barite with sulphides (sphalerite, galena, and chalcopyrite) infilling the interstitial space between the laths (sample CNF31863 from drill hole LM11-68, depth: 203.4 m). (G) Reflected image of microinclusions of sulphides in fluid inclusions in bladed/tabular barite (sample CNF31860 from drill hole LM11-68, depth: 198 m). (H) Reflected image showing euhedral pyrite and disseminated sulphides associated with granular barite (sample CNF31877 from drill hole LM11-66, depth: 164.4 m). Brt, barite; Cp, chalcopyrite; Dol, dolomite; Gn, galena; Py, pyrite; Sp, sphalerite. [Colour online.]

size) that are associated with bornite, chalcopyrite, tetrahedrite–tennantite, galena, pyrite, and electrum (stage 2; Figs. 8A–8D). Radial aggregates ("rosettes") of barite and plumose textured barite are also associated with stage 2 mineralization (Figs. 9A–9B). Locally, large tabular barite crystals are hosted in granular barite or in a dolomitic matrix, and the interstitial spaces between barite blades contain smaller, rounded, possibly recrystallized barite grains (Figs. 9C–9D). The contact between granular barite in stage 1 mineralization and bladed barite in stage 2 mineralization is typically sharp and irregular to locally gradational (Fig. 8D). Both granular and bladed barite are cross-cut by honey brown to red sphalerite, pyrite, galena, and chalcopyrite of stage 3 mineralization (Fig. 8E).

Barite also occurs as thin (approximately 1 cm) veins that cross-cut the granular barite in the upper portion of the mineralized lens (Fig. 8F). Barite-rich veins are generally composed of large interlocking euhedral to subhedral grains with chalcopyrite, galena, and pyrite (stage 3) commonly found in or proximal to these late stage veins. Semi-continuous layers and secondary barite veinlets are also found within the metalliferous mudstone unit, immediately above the massive sulphides (Fig. 8G) (Lode et al. 2015). Barite also occurs deeper in the deposit, occurring in fractures and interstitial spaces in the quartz–sericite-altered footwall volcanic rocks, spatially associated with chalcopyrite, pyrite, honey brown to orange sphalerite, and galena bearing stringers (stage 3; Fig. 8H). Barite and carbonate nodules (up to 3 cm in size) are rare but are found locally within the massive sulphide layers themselves.

In zones of well-formed crystalline tabular barite, sulphide minerals are present in minor amounts and generally occur along barite grain boundaries or in interstitial spaces between grains (Figs. 9E–9F). Growth zones are locally visible in tabular barite and are usually denoted by abundant fluid inclusions that locally contain sulphide microinclusions (<10 μm) (Fig. 9G). Conversely, in zones of high sulphide content, barite generally occurs as small (approximately 1–100 μm), rounded and fractured grains (Fig. 9H).

It is noteworthy that other Ba-rich phases have been observed spatially associated with barite, including celsian ($BaAl_2Si_2O_8$), which is found with alteration minerals such as albite and phlogopite near barite within the massive sulphide lenses, and hyalophane ($(K,Ba)Al(Si,Al)_3O_8$) and witherite ($BaCO_3$), which are present with barite in the mudstones above mineralization (Lode et al. 2015).

Parageneses

As illustrated above, barite has specific mineral textures and sulphide–sulphosalt associations that are related to the paragenetic evolution of the deposits (e.g., Gill et al. 2016). Massive granular barite is paragenetically early and crystallized with pyrite, sphalerite, galena, and minor chalcopyrite of stage 1 mineralization. This was immediately followed by the bladed/tabular barite associated with tetrahedrite–tennantite, Cu-rich phases, pyrite, galena, and electrum of stage 2 mineralization. Small, rounded barite crystals that fill interstitial spaces between larger tabular barite are paragenetically later than the tabular laths; however, these interstitial grains may represent recrystallized phases of earlier granular barite. All the above barite types are cut by barite-rich veins associated with stage 3 mineralization, and these also cut the hanging wall metalliferous mudstones above the massive sulphide lens. Finally, granular barite associated with high-temperature stage 3 mineralization in the footwall stringer zone is the paragenetically youngest barite (e.g., Fig. 7).

Mineral chemistry

The average major element (Ba, Sr, Na, and Ca) concentrations for the 21 analyzed samples (n = 514) are listed in Table 2 (for the complete geochemical data set for all analyzed elements and atoms per formula unit (apfu) calculations refer to Supplementary Table S1[1]). Barite shows little variation in major element composition and is near stoichiometric ($Ba_{0.95–0.99}$, $Sr_{0.01–0.04}$, $Na_{0.01}$, $Ca_{0.00–0.01})SO_4$ regardless of texture. In bladed barite, Ba and S contents vary from 59.66 to 67.97 wt.% (avg. 64.33 ± 1.09 wt.% BaO) and 33.50 to 36.05 wt.% (avg. 34.79 ± 0.41 wt.% SO_3), respectively. Strontium is the most abundant minor element and averages 1.08 ± 0.72 wt.% SrO, but varies between 0.02 wt.% and 4.78 wt.% SrO, and is negatively correlated (r^2 = 0.5388) with BaO. This moderately negative trend suggests that Sr^{2+} substitutes for Ba^{2+} in barite and corresponds to the solid solution between barite and celestine ($SrSO_4$) (Hanor 2000; Zhu 2004; Monnin and Cividini 2006). Bladed barite contains minor to trace amounts of Na and Ca, averaging 0.18 ± 0.09 wt.% Na_2O and 0.02 ± 0.05 wt.% CaO, respectively, but shows very poor correlations with Ba content (Fig. 10). In granular barite, Ba and S contents vary from 62.61 to 67.75 wt.% (avg. 64.74 ± 0.83 wt.% BaO) and from 33.50 to 35.70 wt.% (avg. 34.73 ± 0.43 wt.% SO3), respectively. Strontium varies from 0.02 to 2.89 wt.% (avg. 0.79 ± 0.39 wt.% SrO). Granular barite also contains very minor to trace amounts of Na and Ca, averaging 0.14 ± 0.05 wt.% Na_2O and 0.01 ± 0.01 wt.% CaO, respectively.

Select average trace element concentrations and detected REE analyzed by laser ablation on bladed and granular barite samples are reported in Table 3 (for the complete geochemical data set for all analyzed elements refer to Supplementary Table S2[1]). In general, the results from laser ablation analyses indicate that barite contains low amounts of trace elements that are at or below detection (e.g., Sc, Co, Ni, Ge, In, Bi, and Te). Elevated relative standard deviations (2σ; Supplementary Table S2[1]) are associated with elements that are near detection limits suggesting that the data of elements near detection limits are imprecise. Despite this, some elements are well correlated (Fig. 11). For example, Sb, As, Ag, and Au are well correlated in bladed barite containing metal-rich fluid inclusions (r^2 = 0.77–0.93) (Figs. 11A–11E). Granular barite also exhibits strong positive correlation between As, Sb, and Ag (r^2 = 0.9) (Figs. 11D–11E) and locally contains enrichments of Mo, As, Ag, and Sb (e.g., Fig. 11). However, concentrations of these elements in granular barite are much lower compared with bladed barite (Fig. 11). Additionally, Ga, Mo, Hg, Tl, and V are moderately well correlated in bladed barite that contains metal-rich fluid inclusions (r^2 = 0.71–0.85) compared with granular barite ($r^2 \leq 0.5$)

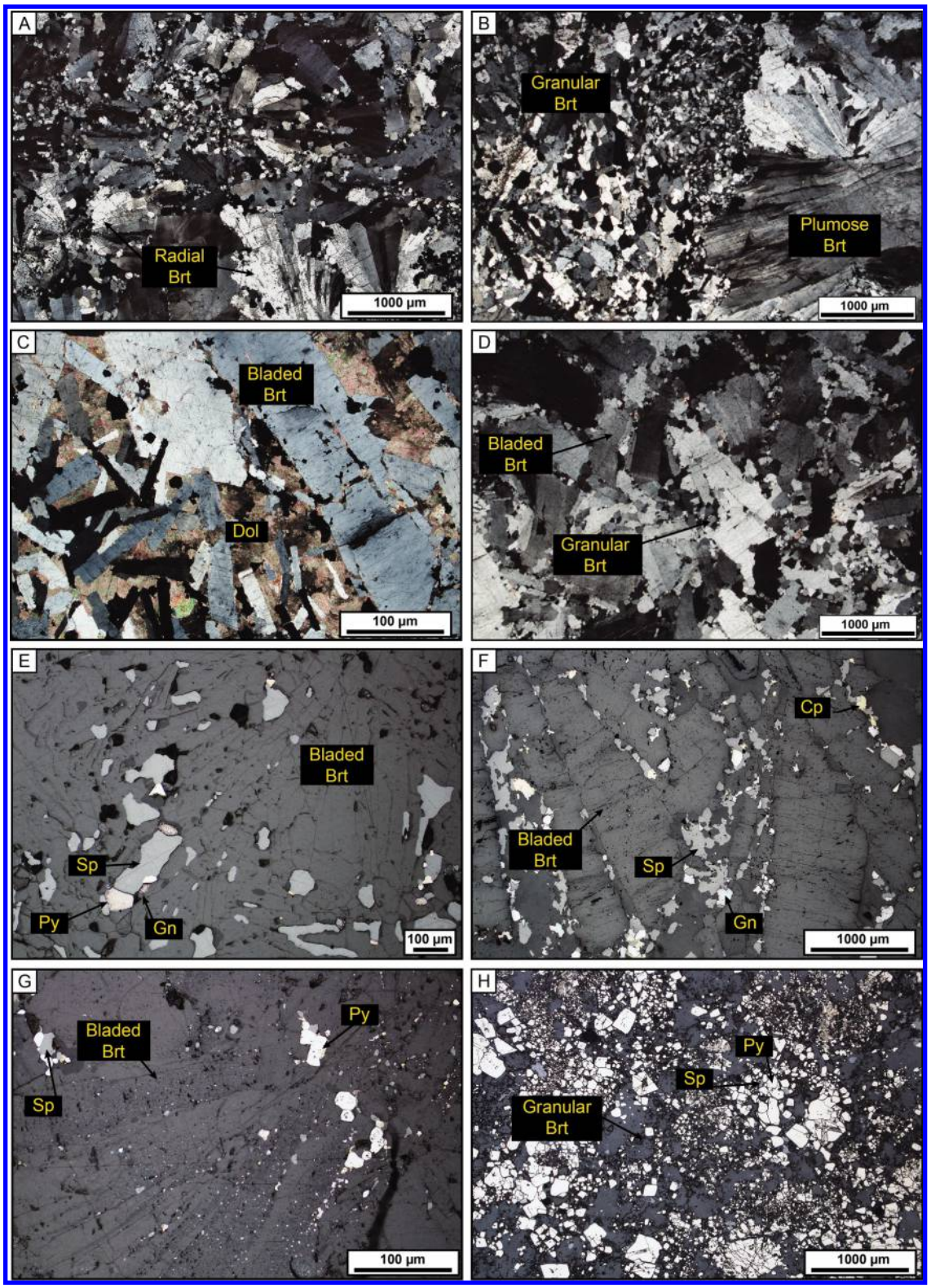

(Figs. 11F–11K). It is likely that these metal enrichments and correlations generally found in bladed barite samples do not reflect trace elements within the lattice of barite, but represent sulphide/sulphosalt inclusions, as detected by SEM (e.g., Fig. 12 and Figs. 14E–14H). Laser ablation analyses were targeted in areas that had minimal mineral inclusions; however, the mineral inclusions (<<10 µm) were often unavoidable as the focused laser beam had a much larger beam diameter of 50 µm so as to ensure sufficient analyte for LA–ICP–MS analysis. Sample CNF31860 contained abundant mineral inclusions and its contrasting geochemistry compared with inclusion-poor bladed and granular barite is highlighted in Fig. 11.

Barite also shows very minor concentrations of light rare earth elements (LREE) (e.g., La, Ce, Eu, Y, and Gd), with most analyses

Table 2. Electron microprobe results of average major element composition of barite (wt.%) from the Lemarchant deposit (n = 514).

	BaO			SO_3			SrO			Na_2O			CaO		
	Av ± 1σ	Min	Max	Av ± 1σ	Min	Max	Av ± 1σ	Min	Max	Av ± 1σ	Min	Max	Av ± 1σ	Min	Max
Bladed	64.33 ± 1.09	59.66	67.97	34.79 ± 0.41	33.72	36.05	1.08 ± 0.72	0.15	4.78	0.18 ± 0.09	0.02	0.67	0.02 ± 0.05	0.00	0.73
Granular	64.74 ± 0.83	62.61	67.75	34.73 ± 0.43	33.50	35.70	0.79 ± 0.39	0.02	2.89	0.14 ± 0.05	0.03	0.28	0.01 ± 0.01	0.00	0.05

Note: Av, average value; Min, minimum value; Max, maximum value.

Fig. 10. Biplots of BaO versus SrO, Na_2O, and CaO. A strong negative correlation exists between Sr and Ba, whereas no correlation exists between Na vs. Ba and Ca vs. Ba. The correlation between Sr and Ba is associated with the solid solution series between celestite ($SrSO_4$) and barite ($BaSO_4$). [Colour online.]

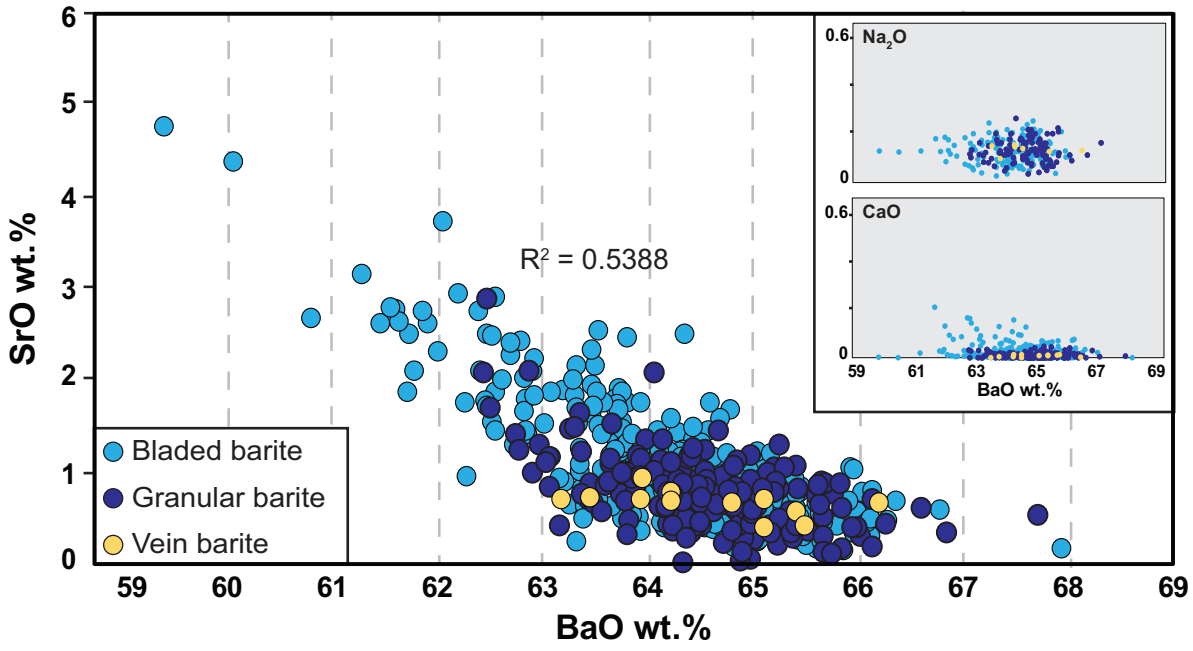

Table 3. Laser ablation results of trace elements (ppm) for bladed and granular barite in the Lemarchant deposit.

	Bladed				Granular					
	Stage 1		Stage 2		Stage 1		Stage 2		Stage 3	
	Av	2σ	Av	2σ	Av	2σ	Av	2σ	Av	2σ
Sc	1.6	3.1	0.6	1.2	0.4	0.8	0.7	1.3	<0.01	—
Ti	16.7	31.6	199.5	82.9	9.7	11.7	68.6	33.3	11.1	6.2
V	0.0	0.0	9.7	3.8	1.0	1.1	18.8	15.3	<0.01	—
Cr	31.8	33.0	25.8	16.4	10.2	10.4	51.3	27.4	<0.01	—
Co	0.0	0.0	0.9	1.1	0.6	0.6	0.6	0.5	0.4	0.2
Ni	7.5	14.2	24.4	23.6	23.3	29.2	17.6	17.1	<0.01	—
Ga	0.1	0.2	4.2	2.2	1.4	1.6	493.6	948.7	<0.01	—
Ge	<0.01	—	2.8	3.0	1.2	1.6	2.6	2.9	1.0	0.5
As	16.9	25.1	46.1	22.0	17.9	16.5	111.5	77.6	1.9	0.7
Se	22.4	16.2	40.3	22.6	63.7	48.2	21.6	9.8	1.3	0.3
Mo	0.0	0.1	74.2	31.2	0.2	0.4	106.5	113.0	0.9	0.3
Ag	5.1	4.6	579.7	181.4	142.9	103.7	1340.4	2028.7	0.2	0.1
In	0.8	1.5	<0.01	—	<0.01	—	0.1	0.1	<0.01	—
Sn	38.1	48.5	8.3	6.8	9.7	4.8	10.7	5.5	0.7	0.4
Sb	0.1	0.2	1.2	0.6	0.6	0.6	4.2	5.7	<0.01	—
Te	<0.01	—	<0.01	—	<0.01	—	0.1	0.3	<0.01	—
Au	2.8	3.4	21.1	15.3	6.4	8.8	3.7	2.0	2.1	0.5
Hg	98.6	39.4	558.3	145.2	462.0	204.1	307.8	220.4	27.3	2.6
Tl	1.0	1.3	28.7	12.2	30.0	22.4	24.8	25.4	<0.01	—
Bi	<0.01	—	1.2	2.3	0.0	0.1	0.0	0.0	<0.01	—
La	11.3	7.1	14.8	4.9	7.2	2.8	36.4	40.6	2.8	0.4
Ce	2.9	3.7	13.5	6.7	2.1	1.4	12.0	10.4	0.7	0.2
Eu	13.2	3.7	8.5	2.0	18.0	5.2	7.3	1.7	12.0	2.2
Gd	465.8	90.0	277.4	31.9	511.6	123.8	227.0	38.5	415.6	46.8

Note: Av, average value.

close to detection limits (Table 3); however, when present, barite is heavily depleted of heavy rare earth elements (HREE) relative to LREE.

Bulk rock analyses: S and Sr isotope data

Measured $\delta^{34}S$ compositions of five granular barite and 18 bladed barite samples within different mineralized zones from the Lemarchant deposit are listed in Table 4. Sulphur isotopic values are shown in Fig. 13 and display a relatively narrow range from 24.7 to 28.7‰, with an average isotope value of 27.1‰. The measured $\delta^{34}S$ values of bladed barite samples show a slightly higher range (25.7 to 28.7‰) than for massive/granular barite (24.7 to 27.8‰). Despite these differences, the average measured $\delta^{34}S$ values for barite within the Northwest zone, Main zone, and 24 zone are very similar and within error (27.0‰, 27.1‰, and 27.3‰, respectively).

Lemarchant barite samples have abundant Sr (approximately 0.3%–0.9%), and minimal Rb (<1 ppm) (Table A1). The high Sr, coupled with low Rb, indicates that the measured Sr isotope ratios are similar to those at the time of formation and do not require age correction for the decay of ^{87}Rb. The barite exhibits a narrow range of $^{87}Sr/^{86}Sr$ ratios ranging from 0.706905 ± 0.000010 to 0.707485 ± 0.000010 (Table 5 and Fig. 13).

Fluid inclusion petrography

Fluid inclusion assemblages were analysed in bladed barite from samples CNF31723, CNF31860, CNF31865, and CNF31874 (drill holes LM13-73, LM11-68, LM14-96, and LM13-82, respectively; Table 1) and within a vein composed entirely of barite from sample CNF31723. Three types of fluid inclusion assemblages (type-I,

Fig. 11. Compositional plots of selected trace elements from bladed, granular, and inclusion-rich bladed barite samples of the Lemarchant deposit. (A) Au vs. Sb, (B) Au vs. Ag, (C) Au vs. As, (D) As vs. Ag, (E) Sb vs. Ag, (F) Mo vs. Hg, (G) Hg vs. Tl, (H) Mo vs. Tl, (I) Ga vs. Mo, (J) Ga vs. Hg, (K) Ga vs. Tl. [Colour online.]

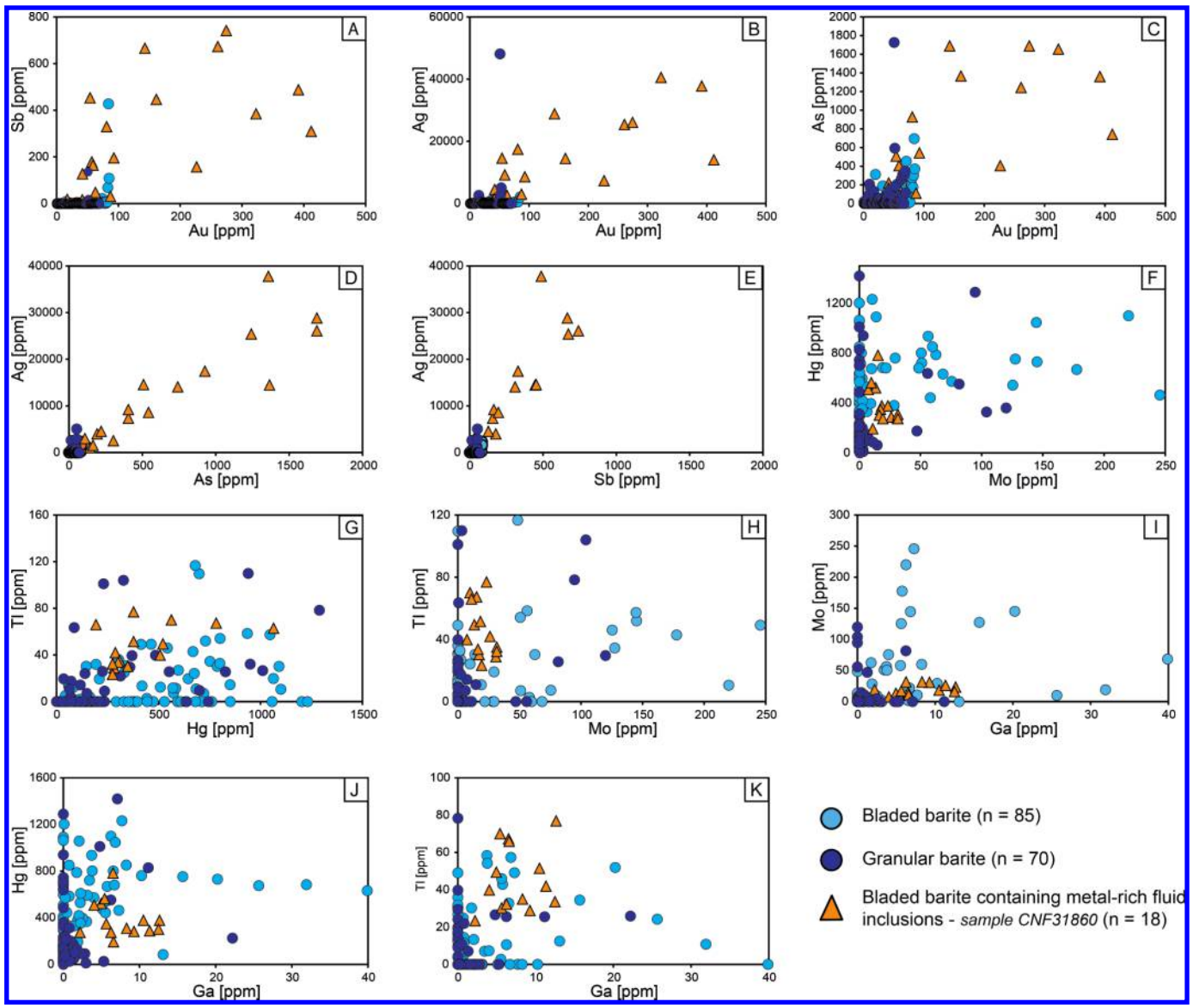

-II, and -III) occur in primary growth zones (Fig. 14) in barite including (in order of decreasing abundance at room temperature):

I. Three-phase immiscible liquid aqueous–carbonic inclusions ($L_1 + L_2 \pm V$) (Roedder and Coombs 1967; Roedder 1984; Van den Kerkhof and Thiery 2001) that have two immiscible liquids, one aqueous and the other liquid CO_2 occurring as a thin meniscus surrounding a carbonic vapour phase (approximately 20–40 vol.%) (Figs. 14A–14B). The inclusions are <1 μm to approximately 30 μm and are equant to oblate.
II. Two-phase, liquid (L)-rich, containing liquid water plus a water (± CO_2) vapor bubble of approximately 40–60 vol.%. The inclusions are irregular to equant in shape.
III. Vapor (V)-rich (80–100 vol.%) (±CO_2) inclusions.

The fluid inclusion assemblages occur as clusters away from crystal edges and within the primary growth zones of the host crystal (Figs. 14C–14D). Pseudo-secondary inclusions, although less common than primary inclusions, cross-cut growth zones; however, the inclusion trails do not cut across all growth zones of the host mineral. Captured sulphide inclusions (i.e., tetrahedrite–tennantite, pyrite, galena, and electrum) of stage 2B mineralization (e.g., Gill 2015) are found within what appears to be in type-I primary and pseudo-secondary fluid inclusion trails in bladed barite crystals (Figs. 14E–14H). Secondary fluid inclusion assemblages are less common than primary inclusions and occur as trails cross-cutting all growth zones of the host mineral.

Type-I inclusions are by far the most abundant (i.e., 75 to 95% of the inclusions observed) and present in both bladed barite and the barite vein. Type-II inclusions consist of 5 to 25% of the observed fluid inclusion assemblages and are present in bladed barite and occur together with aqueous–carbonic inclusions (type-I). Type-III inclusions are very rare (<2%) and most are decrepitated inclusions.

Fluid inclusion microthermometry

Microthermometric data from fluid inclusions in bladed barite from the Lemarchant deposit are listed in Table C1. The aqueous carbonic inclusions (type-I) were cooled to temperatures lower

Fig. 12. Back scattered electron (BSE) image and semiquantitative elemental maps (Ba, S, Cu, Zn, and Pb) showing an example of captured sulphide phases in pseudo-secondary fluid inclusion trails in barite blades (sample CNF31860 from drill hole LM11-68, depth: 198 m). [Colour online.]

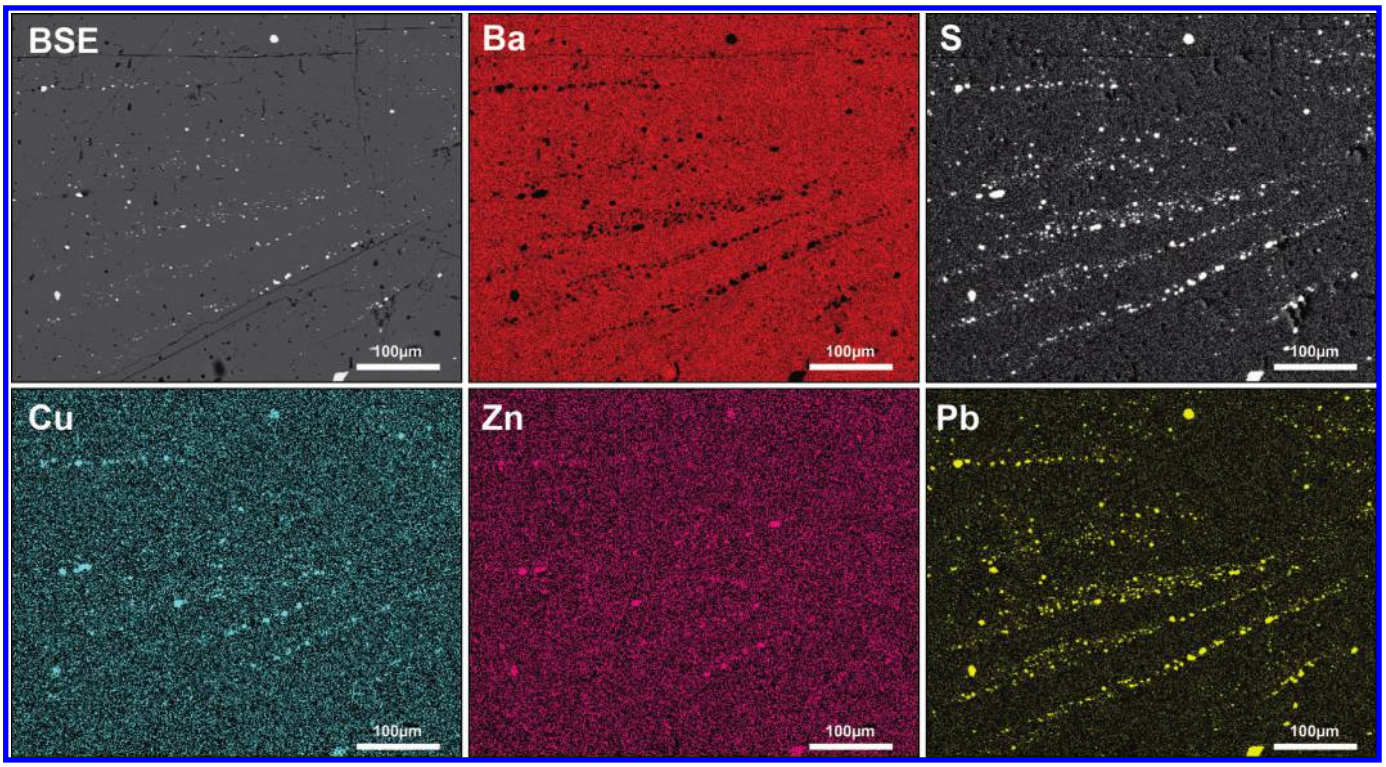

Table 4. Sulphur isotope values ($\delta^{34}S$ V-CDT) of granular and bladed barite samples from the Lemarchant deposit.

Sample name	Drill hole	Barite texture	Mineralized zone	$\delta^{34}S$ (‰ V-CDT)
CNF31715	LM13-73	Granular	Northwest zone	27.8
CNF31721	LM13-73	Granular	Northwest zone	27.0
CNF31723	LM13-73	Granular	Northwest zone	24.7
CNF31730	LM13-94	Granular	Northwest zone	27.1
CNF31861	LM11-68	Granular	Main zone	27.4
CNF31721	LM13-73	Bladed	Northwest zone	27.8
CNF31723	LM13-73	Bladed	Northwest zone	28.1
CNF31733	LM13-97	Bladed	Northwest zone	26.7
CNF31809	LM10-43	Bladed	Main zone	27.9
CNF31810	LM10-43	Bladed	Main zone	27.6
CNF31811	LM10-43	Bladed	Main zone	26.1
CNF31811	LM10-43	Bladed	Main zone	26.9
CNF31812	LM10-43	Bladed	Main zone	26.6
CNF31812	LM10-43	Bladed	Main zone	26.5
CNF31812	LM10-43	Bladed	Main zone	26.1
CNF31816	LM08-19	Bladed	24 zone	27.3
CNF31829	LM07-15	Bladed	Main zone	27.8
CNF31855	LM11-52	Bladed	Main zone	27.3
CNF31860	LM11-68	Bladed	Main zone	28.7
CNF31861	LM11-68	Bladed	Main zone	26.9
CNF31865	LM14-96	Bladed	Northwest zone	25.7
CNF31868	LM14-96	Bladed	Northwest zone	27.0
CNF31874	LM13-82	Bladed	Northwest zone	27.5

Note: V-CDT, Vienna Canyon Diablo Troilite.

than –100 °C to trigger solidification and slowly heated until melting of the carbonic phase occurred. Upon heating, the initial melting temperatures of the carbonic phase ($T_m(CO_2)$) (n = 11) occurred between –56.0 and –57.1 °C (avg. –56.2 ± 0.3 °C), which is close to the melting point of pure CO_2 (–56.6 °C). Final melting temperatures recorded in type-I inclusions were interpreted as the melting of clathrate phases (T_m(clath)) and occurred from 7.6 °C to 9.9 °C (avg. 9.3 ± 0.7 °C; n = 18). The average salinity of the aqueous carbonic inclusions within both the bladed and vein barite is 1.2 ± 1.2 wt.% NaCl equivalent (Fig. 15*a*), which is lower than seawater values (3.2 wt.% NaCl equivalent: Bischoff and Rosenbauer 1985; Bodnar and Vityk 1994). Upon further heating, the temperature of homogenization of CO_2 into the liquid state (T_hCO_2) for aqueous carbonic inclusions occurred between 30.2 and 31.0 °C (avg. 30.6 ± 0.3 °C, n = 6) (Fig. 15*b*).

Final homogenization temperatures (T_h(total)) of type-I inclusions in both bladed and vein barite (n = 18) occurred at temperatures between 191 and 276 °C (avg. 245.2 ± 16.5 °C), with most of the temperatures measured between 245 and 250 °C (Fig. 15*c*). All type-I inclusions homogenized to the liquid phase or decrepitated prior to final homogenization.

Final melting temperatures in type-II inclusions occurred between –4 and 1 °C (n = 6). Final melting temperatures above 0 °C are consistent with clathrates forming during freezing, indicating the presence of CO_2 in type-II inclusions (Diamond 2001). Although measurements of final homogenization temperatures (T_h(total)) of type-II inclusions are less abundant than measurements of type-I inclusions, the final homogenization temperatures are lower and range from 198 to 216 °C (avg. 210.2 ± 7.0 °C; n = 4) (Fig. 15*c*).

Final homogenization temperatures (T_h(total)) for type-III inclusions could not be determined as all the inclusions were decrepitated. Whereas type-III inclusions are difficult to distinguish from decrepitated or leaked inclusions, CO_2 was detected in a small number of vapour-rich inclusions from initial melting temperatures (T_{mi}) (–56 °C; n = 1) and final melting temperatures (T_m) of the clathrate (7.8 °C to 10.3 °C; n = 3).

Fluid inclusion pressure trapping conditions

Microthermometric data for type-I fluid inclusion assemblages were used to calculate the minimum trapping pressure for these

Fig. 13. Plot of S isotopic composition of bladed and granular barite versus whole-rock Sr isotopic geochemistry of barite from the Lemarchant deposit and approximate endmember composition of different reservoirs. Light orange areas represent S and Sr isotopic composition of middle to late Cambrian seawater ($\delta^{34}S \approx 25–30‰$ and $^{87}Sr/^{86}Sr \approx 0.7090$, respectively; Sangster 1968; Claypool et al. 1980; Ohmoto and Goldhaber 1997; Huston 1997; Seal 2006; Burke et al. 1982; Derry et al. 1989, 1994; Asmerom et al. 1991; Montañez et al. 1996; Denison et al. 1998). Dotted black lines represent S isotope composition of magmatic sulphate ($\delta^{34}S \sim 0‰$; Ohmoto and Rye 1979; Janecky and Shanks 1988; Huston 1997; Shanks 2001; Seal 2006) and Sr isotope composition of Cambrian–Ordovician mantle-derived material ($^{87}Sr/^{86}Sr \approx 0.7030$; Ayuso and Schulz 2003). Ranges of S isotope signatures of microbial reduction of sulphate ($\delta^{34}S < 0‰$; Elsgaard et al. 1994; Habicht and Canfield 2001; Shanks 2001; Seal 2006) and Sr isotope signatures of more radiogenic crustal material ($^{87}Sr/^{86}Sr > 0.7100$; Griffith and Paytan 2012) signatures are shown by the dark blue arrows. V-CDT, Vienna Canyon Diablo Troilite. [Colour online.]

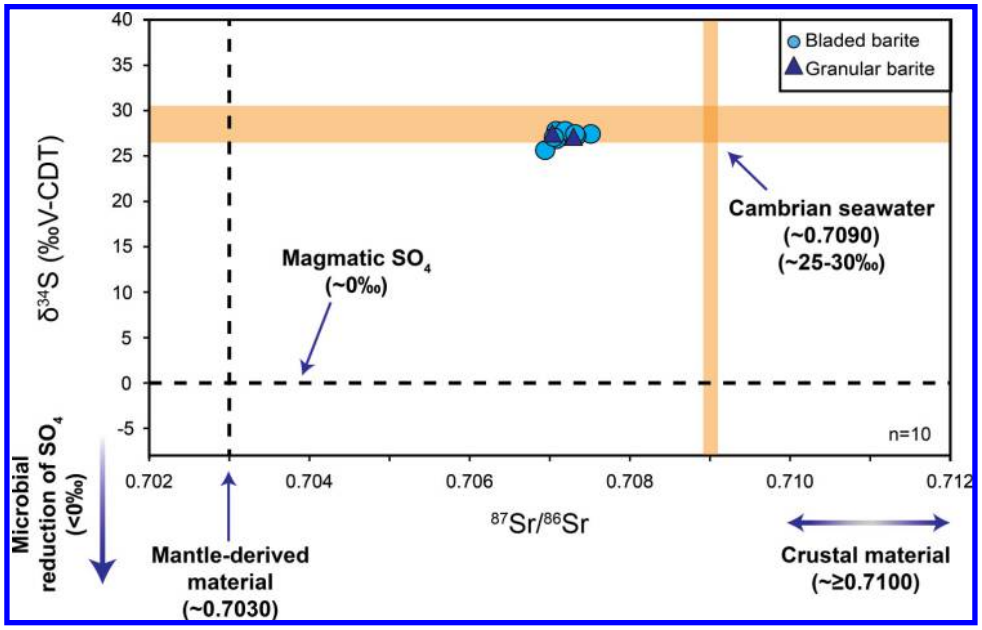

Table 5. Whole-rock strontium isotope ratios ($^{87}Sr/^{86}Sr$), calculated % hydrothermal fluid, Sr and Rb concentrations (ppm), and calculated [Sr]/[Ba] ratios from barite whole-rock lithogeochemical analyses.

Sample No.	Drill hole	Depth (m)	$^{87}Sr/^{86}Sr \pm 2\sigma$	% hydrothermal fluid[a]	Sr (ppm)[b]	Rb (ppm)[b]	[Sr]/[Ba] (Whole-rock)[c]
CNF31816	LM08-19	98.1	0.707485 ± 0.000010	37	4889	1	0.010
CNF31861	LM11-68	199.9	0.707320 ± 0.000010	41	5905	<1	0.011
CNF31733	LM13-94	341.4	0.707053 ± 0.000010	47	9348	<1	0.017
CNF31810	LM10-43	218.8	0.707049 ± 0.000010	47	4034	<1	0.008
CNF31730	LM13-94	332.3	0.707283 ± 0.000010	42	5419	2	0.010
CNF31721	LM13-73	333.0	0.706993 ± 0.000010	48	4997	<1	0.009
CNF31874	LM13-82	340.8	0.707192 ± 0.000010	44	3604	<1	0.007
CNF31865	LM14-96	309.9	0.706905 ± 0.000010	51	7438	<1	0.013
CNF31868	LM14-96	314.3	0.707031 ± 0.000010	48	7233	<1	0.013
CNF31855	LM11-52	216.2	0.707305 ± 0.000010	41	5693	<1	0.010

[a]% hydrothermal fluids are calculated using eq. (1).
[b]Sr and Rb concentrations (ppm) from whole-rock lithogeochemical data.
[c][Sr]/[Ba] ratios are calculated based on Sr and Rb from whole-rock lithogeochemical data.

assemblages, and to construct isochores (Table 6 and Table C2). A total of four isochores were constructed for FIA in four separate samples with calculated fluid densities of 22.14 to 24.17 cc/mol and xCO_2 of 0.08 to 0.13. Minimum trapping pressures for these fluid inclusion assemblages ranged from 1.7 to 2.0 kbars, which corresponds to depths of approximately 6.5 to 7.9 km (assuming a lithostatic pressure gradient of 0.27 kbars/km). Although these minimum trapping pressures assume a pure $H_2O–CO_2–NaCl$ composition, the presence of other trace amounts of gases (e.g., CH_4 and H_2S) are likely to have only a minor effect on calculated pressures (Swanenberg 1979; Roedder and Bodnar 1980). Therefore, the calculated minimum trapping pressures and depths of type-I inclusions are much higher than would be expected for a shallow water VMS deposit like Lemarchant (i.e., >1500 m below sea level for Kuroko-type VMS deposits; Monecke et al. 2014).

Discussion

Barite is common in many VMS deposits, including many bimodal felsic (Kuroko)-type deposits (e.g., Eldridge et al. 1983; Lydon 1984; Large 1992; Ohmoto 1996). Barite in VMS deposits is interpreted to have formed from the mixing of Ba- (+Ca, Sr)-rich hydrothermal fluids with sulphate from seawater, typically in the early stages of mound growth (e.g., Eldridge et al. 1983; Large 1992; Ohmoto 1996). Correspondingly, the bulk rock and mineral chemistry of barite, as well as its S, Sr, and fluid inclusion data can provide insight into barite genesis and subsequent modification. The discussion below addresses the origin of barite in the Lemarchant deposit using this multi-proxy approach, as well as addresses the effects of post-VMS deformation and metamorphism on fluid inclusions present within barite.

Fig. 14. Photomicrographs of fluid inclusions in bladed barite from the Lemarchant deposit. (A) Transmitted light image showing secondary carbonic-rich fluid inclusion (L1+L2+V) population in primary growth zones in a late barite vein (sample CNF31723 from drill hole LM13-73, depth: 346.5 m). (B) Transmitted light image showing secondary carbonic-rich fluid inclusion population clearly showing the immiscible three phases (L1+L2+V) (sample CNF31874 from drill hole LM13-82, depth: 340.8 m). (C) Transmitted light image of bladed barite showing clusters of secondary fluid inclusions (L1+L2+V) in primary growth zones found in the center of blades (sample CNF31723 from drill hole LM13-73, depth: 346.5 m). (D) Transmitted light image of bladed barite showing clusters of secondary fluid inclusions (L1+L2+V) in primary growth zones in the center of the blades (sample CNF31874 from drill hole LM13-82, depth: 340.8 m). (E) Cross-polarized image showing growth zones in a single tabular barite crystal that are delineated by primary fluid inclusions that contain sulphides (black) (sample CNF31735 from drill hole LM13-94, depth: 346.7 m). (F) Reflected image of the growth zones in a single tabular barite crystal supporting the presence of captured sulphides within the fluid inclusions. The sulphides are generally composed of sphalerite, galena, chalcopyrite, pyrite, and tetrahedrite (sample CNF31735 from drill hole LM13-94, depth: 346.7 m). (G) Transmitted light image of secondary fluid inclusions that also contain microinclusions of captured sulphides (sample CNF31860 from drill hole LM11-68, depth: 198 m). (H) Reflected image of secondary fluid inclusions clearly showing the abundance of microinclusions of sulphides within inclusion trails (sample CNF31860 from drill hole LM11-68, depth: 198 m). [Colour online.]

Mineral chemical variations

Barite crystals, regardless of type, show little geochemical variations, with most having similar major element compositions and S and Sr isotope signatures (e.g., Figs. 10 and 13). Moreover, they have low trace element contents with most having trace element concentrations at or near the detection limits of EMPA and LA–ICP–MS. One exception to the latter is Sr, which is up to 4.78 wt.% SrO in barite, despite bulk rock chemical analyses indicating much lower Sr contents (<1 wt.% Sr; Table A1). Low Sr in bulk rock chemical analyses is likely diluted by sulphides and silicate minerals. The SrO contents of Lemarchant barite are similar to barite in modern hydrothermal deposits. For example, SrO contents vary from 0.6 to 3.5 wt.% in barite from the Franklin Seamount, Papua New Guinea (Binns et al. 1993); 0 to 17.8 wt.% (av. 7 wt.%) in barite from the Endeavour Segment, Juan de Fuca Ridge (Jamieson et al. 2016); and up to 4.4 wt.% in barite from the Axial Seamount, Juan de Fuca Ridge (Hannington and Scott 1988). The Sr contents of barite in ancient VMS deposits are also variable (i.e., 0–2 wt.%, Hellyer deposit, Australia, Sharpe 1991; up to 4.73 wt.%, Saf'yanovka, Central Urals, Safina et al. 2016). Similarities in ionic radii, charge, and electronegativity between Ba^{2+} and Sr^{2+} create a complete solid solution between barite ($BaSO_4$) and celestite ($SrSO_4$) (Sabine and Young 1954; Boström et al. 1967). The variation in SrO is attributed to this solid solution series and varying Sr substitution for Ba in the barite structure. The range of SrO contents for barite was initially thought to represent fluctuations in fluid chemistry during ore genesis or the high degree of mixing between ambient seawater and hydrothermal fluids (Farrell et al. 1978; Kalogeropoulos and Scott 1983, 1989; Farrell and Holland 1983; Hannington and Scott 1988). However, Jamieson et al. (2016) suggested that the Sr-partitioning in barite is attributed to temperature fluctuations and that Sr substitution is independent of fluid mixing. Our results agree with the latter model and this will be discussed in greater detail below.

The enrichment of Ag, Sb, and Au in bladed barite compared with granular barite is directly related to microinclusions of electrum, galena, sphalerite, and tetrahedrite–tennantite. Although electrum inclusions were not observed via reflected light petrography and SEM, the high content of Au (up to approximately 400 ppm) in some bladed barite suggests the presence of gold-rich microinclusions in selected samples (i.e., CNF31860). The strong correlation and localized peaks of Ga–Mo–Hg–Tl–V are attributed to pyrite and possibly minor colusite inclusions within bladed barite as these elements are enriched in these minerals and are found in stage 2 mineralization (Gill et al. 2015, 2016; Fig. 7).

Petrographic observations of bladed barite also show that sulphide inclusions are found within or associated with fluid inclusions, usually along growth zones or in pseudo-secondary fluid inclusion trails (Figs. 14E–14H). It is suggested that the sulphide inclusions were "captured" mineral phases, and were solid phases suspended in the ore-forming fluid that were trapped in the inclusions, rather than daughter minerals. This is attributed to the fact that only some inclusions within a single fluid inclusion assemblage have sulphide inclusions, rather than being present in all inclusions as would be expected if these sulphides precipitated from the fluid after trapping. In recent years, some workers have suggested that gold in hydrothermal systems can be transported in particulate form from high-temperature boiling fluids into lower temperature vents (Gartman et al. 2018; Hannington et al. 2016). The sulphide particulates observed in certain bladed barite samples could potentially represent deposition from sulphide (± gold) colloids, which were carried upward in suspension via boiling of hydrothermal fluids. The transportation of gold colloids in suspension, combined with significant mixing and cooling, could represent an alternative mechanism for gold transportation and deposition at the Lemarchant deposit that has not been previously suggested.

Sulphur sources

Sulphur in VMS deposits can come from a variety of sources, including leaching of basement rocks, seawater sulphate, and in some cases, magmatic fluids (Ohmoto and Rye 1979; Sakai et al. 1984; Janecky and Shanks 1988; Halbach et al. 1989; Rye 1993; de Ronde 1995; Hannington et al. 1995; Herzig et al. 1998; Shanks 2001; de Ronde et al. 2005; Seal 2006). Negligible sulphate concentrations have been observed in many modern hydrothermal vent fluids (e.g., Butterfield et al. 1990, 1997; Reeves et al. 2011; Bischoff and Seyfried 1978). Assuming that the Lemarchant deposit formed under similar hydrothermal fluid conditions as modern seafloor systems (e.g., Gill et al. 2016), it can be presumed that the fluids that formed the deposit had low concentrations of sulphate. Moreover, although there were variations in seawater sulphate concentrations in the Phanerozoic (Berner 2004), the concentration of seawater sulphate is much higher than sulphate in hydrothermal fluids (e.g., von Damm et al. 1985). Correspondingly, it is likely that hydrothermal sulphate was not an important contributor to the sulphate budget of barite in the Lemarchant deposit.

Most workers argue that seawater sulphate is the main source of sulphate in VMS-associated sulphate minerals (Huston 1997; Seal et al. 2000), whereas in some relatively rare instances sulphate from magmatic fluids, commonly from condensed SO_2, can result in the precipitation of sulphate minerals (e.g., Rye 1993, 2005; Huston et al. 2011). The $\delta^{34}S$ isotope data for both granular and bladed barite in the Lemarchant deposit are similar (Table 4; Fig. 13), overlapping the values for Cambrian seawater sulphate (Sangster 1968; Claypool et al. 1980; Ohmoto and Goldhaber 1997; Huston 1997; Seal 2006), and similar to the sulphur isotope values in barite from other Cambro–Ordovician VMS deposits globally (e.g., 25–28‰, Barite Hill deposit, South Carolina, Seal et al. 2001; 22.5–24.8‰, Buchans deposit, Newfoundland, Kowalik et al. 1981; and 27.6–32.4‰, Mt. Windsor deposit, Australia, Hill 1996). In contrast, sulphates formed from magmatic SO_2 can result in complex sulphate–sulphide relationships with highly variable $\delta^{34}S$ in

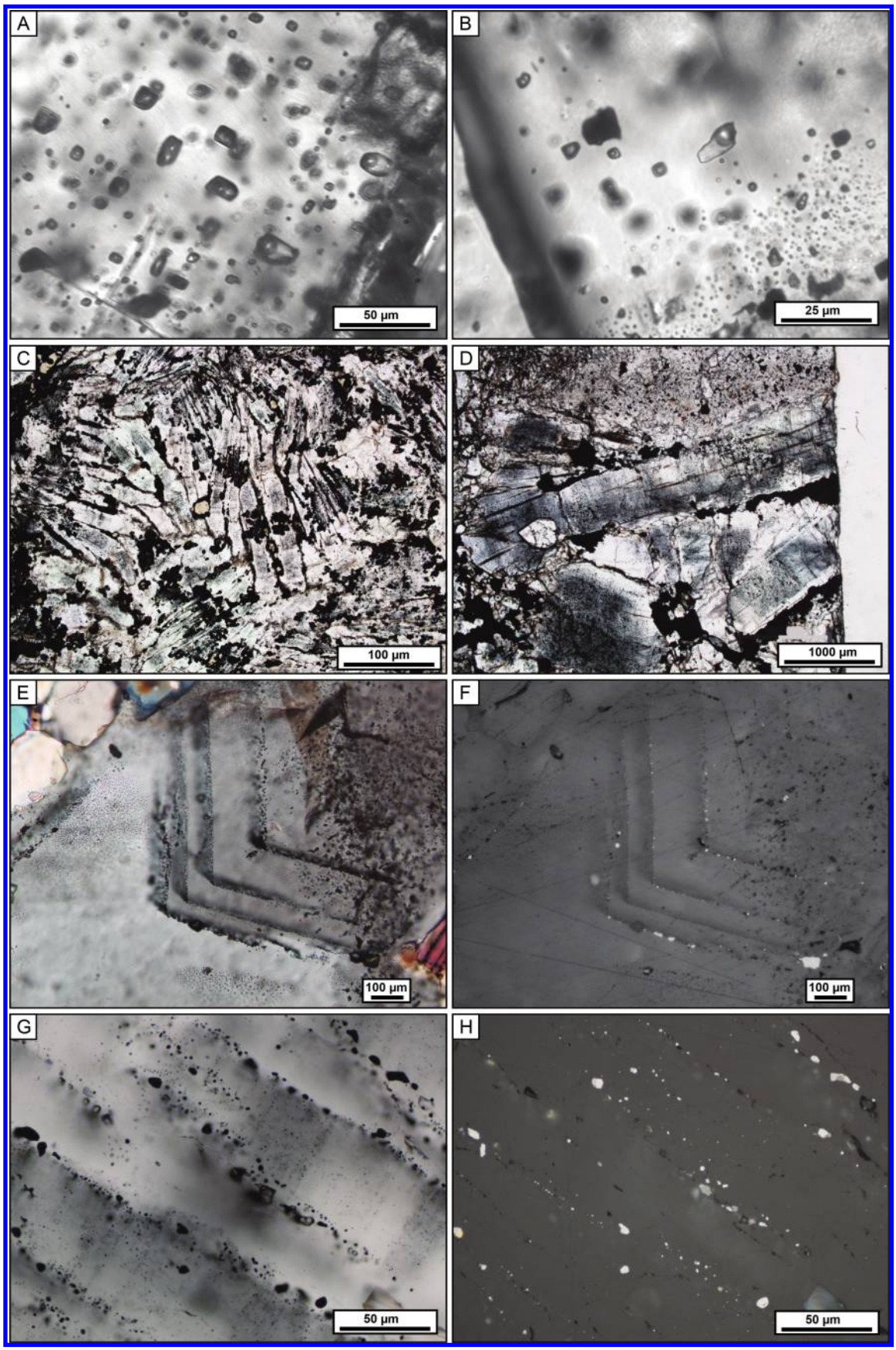

Fig. 15. Fluid inclusion microthermometry results. (A) Salinity (wt.% NaCl equivalent) versus homogenization temperatures (T_h) of type-I (three-phase CO_2) inclusions. The squares represent the average salinity of individual fluid inclusion assemblages, whereas the solid black bars represent the range of salinities within individual fluid inclusion assemblages. The black squares represent salinity and homogenization temperatures (T_h) of type-I inclusions from a barite vein (CNF31723). Note that the average salinities are below 2 wt.% NaCl equivalent. (B) Range of temperature of homogenization of CO_2 (T_hCO_2) (indicated by the shaded purple area) of all type-I inclusions in bladed barite. The theoretical melting point of CO_2 is indicated by the vertical dashed black line. (C) Homogenization temperatures (T_h) of type-I and type-II (aqueous two-phase) fluid inclusions. The T_h of type-I inclusions are represented by the shaded purple area, whereas the T_h for type-II inclusions are indicated by the shaded grey area. Notice that the T_h for type-I inclusions are generally higher than those of type-II inclusions. [Colour online.]

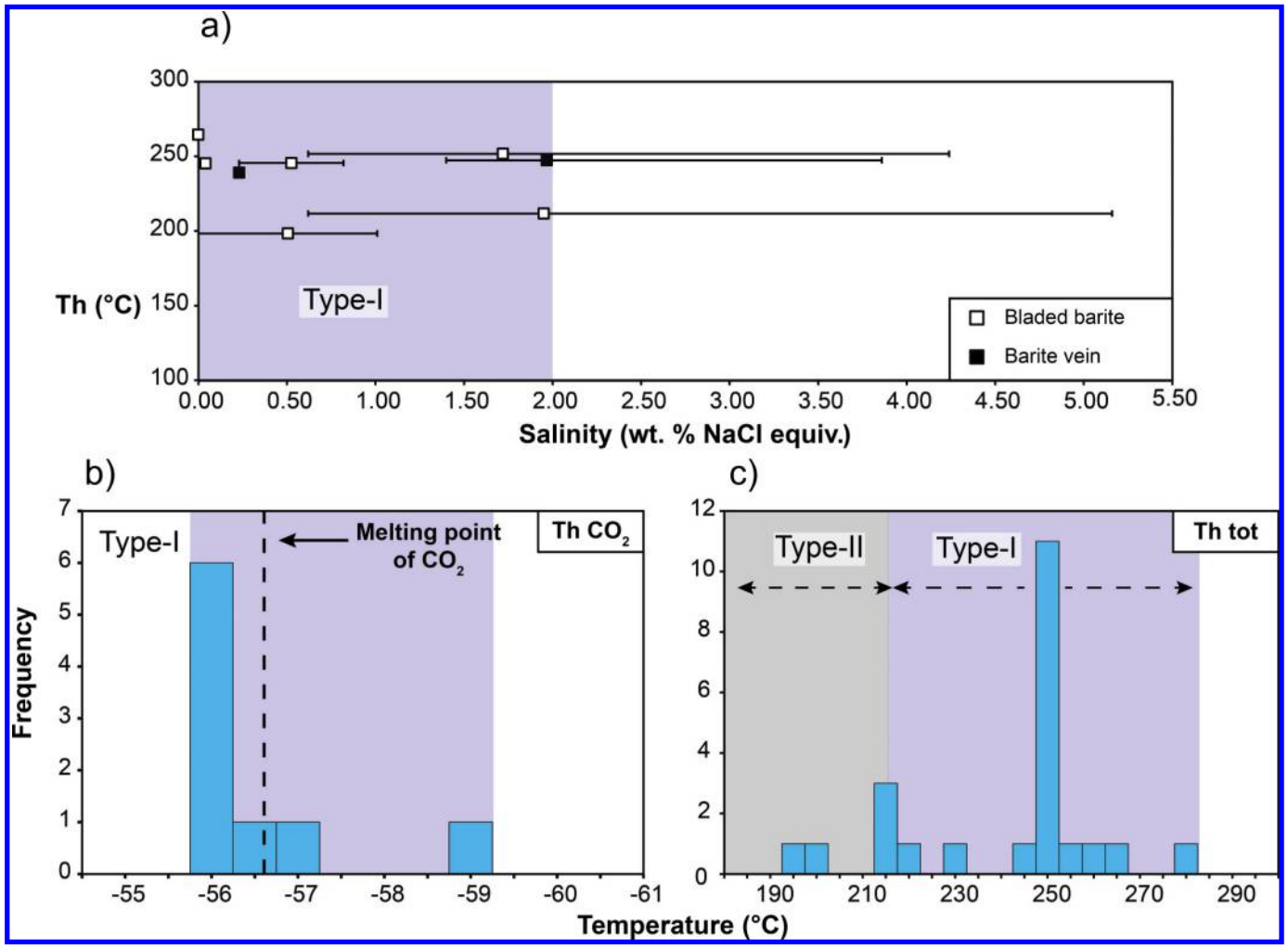

Table 6. Calculated minimum trapping pressures and trapping depths (assuming lithostatic pressure gradient of 2.7 g/cm^3) for type-I inclusions in bladed barite from the Lemarchant deposit.

Sample/inclusion No.	xH_2O	xCO_2	xNa	xCl	Density (cc/mol)	Minimum trapping pressure (bars)*	Minimum trapping depth (lithostatic pressure) (km)
CNF31723 (bladed barite)†	—	—	—	—	—	—	—
CNF31874 -1 (bladed barite)	0.8658	0.1298	0.0022	0.0022	23.99	1759	6.64
CNF31874 -2 (bladed barite)	0.8753	0.1234	0.0006	0.0006	24.17	1711	6.46
CNF31865 (bladed barite)	0.8894	0.1039	0.0033	0.0033	23.06	1956	7.38
CNF31860 (bladed barite)	0.9151	0.0825	0.0012	0.0012	22.14	2007	7.58

Note: Molar concentrations of H_2O, CO_2, Na, and Cl determined using microthermometric measurements and the software package CLATHRATES (Bakker 1997). Minimum trapping pressures calculated using the Q2 program and calculated from homogenization temperatures of aqueous carbonic inclusion assemblages (Bakker 1997; Bakker and Brown 2003).

*Pressures (bars) were calculated using the Q2 program within the software Loner15.

†No pressure calculations could be processed for the fluid inclusion assemblage of sample CNF31723.

sulphates due to sulphur partitioning between H_2S-bearing phases and SO_4-bearing phases during SO_2 disproportionation (e.g., Rye 1993; Seal 2006; Ray et al. 2017). Whereas more positive $\delta^{34}S$ sulphate can form during this process (e.g., Rye 1993, Seal 2006), the homogeneity of the $\delta^{34}S$ signature in the Lemarchant barite, coincident with the remarkable similarity to $\delta^{34}S$ for Cambrian seawater, supports that seawater sulphate was the main source of S in the Lemarchant barites. The likely seawater sulphate source for S in the Lemarchant barite is also consistent with existing models for barite formation, which suggest formation via the mixing of Ba-rich hydrothermal fluids with SO_4-rich seawater (e.g., Ohmoto 1996).

Strontium sources

The Sr isotopic composition of barite has been used to constrain the source of Sr in the fluids that formed barite (Paytan et al. 1993). In VMS deposits, the potential sources of Sr include seawater, crustal basement (i.e., high $^{87}Sr/^{86}Sr$ sources), and mantle-derived mafic crust (i.e., low $^{87}Sr/^{86}Sr$ sources) (Griffith and Paytan 2012). Strontium isotopic studies of carbonate rocks have shown that the $^{87}Sr/^{86}Sr$ of Cambrian seawater is ≈0.7090 (Burke et al. 1982; Derry et al. 1989, 1994; Asmerom et al. 1991; Montañez et al. 1996; Denison et al. 1998). Although Cambrian seawater $^{87}Sr/^{86}Sr$ is well known, deciphering hydrothermal to magmatic/hydrothermal signatures is more problematic. In modern systems, ridge-dominated hydrothermal signatures have Sr isotopic signatures similar to underlying basaltic crust ($^{87}Sr/^{86}Sr$ approximately 0.7030–0.7035; Albarède et al. 1981; Ayuso and Schulz 2003; Griffith and Paytan 2012), and fluids in the Cambrian that equilibrated with Sr from such sources would inherit similar signatures (i.e., mid-Cambrian mantle; $^{87}Sr/^{86}Sr \approx 0.7025–0.7030$; Ayuso and Schulz 2003). In contrast, fluids that equilibrated with crustal material would have higher $^{87}Sr/^{86}Sr$ values, similar to the isotopic signatures of the underlying crust (e.g., $^{87}Sr/^{86}Sr$ of upper crust at 510 Ma is ≈0.7103; calculated from the $^{87}Sr/^{86}Sr$ composition and average Rb and Sr concentration of upper crust from Goldstein and Jacobsen (1988)).

The Sr isotopic compositions of barite at Lemarchant have $^{87}Sr/^{86}Sr = 0.7069–0.7075$, values that are much lower than the $^{87}Sr/^{86}Sr$ values of Cambrian seawater (approximately 0.7090; Burke et al. 1982; Derry et al. 1989, 1994; Asmerom et al. 1991; Montañez et al. 1996; Denison et al. 1998). Moreover, the $^{87}Sr/^{86}Sr$ ratios of the Lemarchant barites are less than the average value of 0.7104 for mid-Cambrian upper continental crust, thus requiring a source more juvenile than both Cambrian seawater and upper continental crust. There is abundant geochemical, isotopic, and field evidence for young continental basement beneath the Tally Pond Group, including juvenile basaltic material from the Sandy Brook Group that have weakly evolved Nd isotopic signatures (Rogers et al. 2006; McNicoll et al. 2010). The Sr isotope signature of these mafic rocks is likely between mantle values (i.e., $^{87}Sr/^{86}Sr$ approximately 0.7025–0.7030; Albarède et al. 1981; Ayuso and Schulz 2003; Griffith and Paytan 2012) and normal Cambrian upper crust ($^{87}Sr/^{86}Sr$ approximately 0.7103; Griffith and Paytan 2012). Thus, the $^{87}Sr/^{86}Sr$ values lower than Cambrian seawater and evolved upper continental crust suggest that at least some of the Sr present in the barite was derived from the basalt-rich, Neoproterozoic crust of the Sandy Brook Group.

Table 7. Measured temperatures (°C), Sr concentrations (μmol/kg), and Sr isotopic ratios of hydrothermal fluids and seawater from the PACMANUS hydrothermal vent field.

	PACMANUS vent fluid[a]	Seawater[a]
Temperature (°C)	247	3
Sr (μmol/kg)	0.099	0.091
$^{87}Sr/^{86}Sr$	0.7049[b]	0.7092[c]

Note: Values used in two-component fluid mixing calculations.

[a]PACMANUS vent fluid chemistry and seawater values are from Reeves et al. (2011).

[b]Average Sr-isotope ratios from vent fluids from the PACMANUS vent field (Reeves et al. 2011).

[c]From Reeves et al. (2011).

The leaching of Sr from basement rocks is consistent with existing models for Sr sources in barite in VMS deposits (e.g., Whitford et al. 1992; Marchev et al. 2002; Ayuso and Schulz 2003). These results also illustrate the decoupling of isotopic systems in barite, where Sr is derived predominantly from basement sources, and S is derived predominantly from seawater, consistent with seawater–hydrothermal fluid mixing models for barite genesis (von Damm 1990; Hannington et al. 2005; Griffith and Paytan 2012). However, the relative abundances of Sr from the fluid vs. seawater remain unquantified and to test this we have employed the mixing model of Mills et al. (1998):

$$(1)\qquad \%HF = 100 \times \frac{[Sr]_{SW}\left[(^{87}Sr/^{86}Sr)_{SW} - (^{87}Sr/^{86}Sr)_{M}\right]}{[Sr]_{SW}\left[(^{87}Sr/^{86}Sr)_{SW} - (^{87}Sr/^{86}Sr)_{M}\right] + [Sr]_{HF}\left[(^{87}Sr/^{86}Sr)_{M} - (^{87}Sr/^{86}Sr)_{HF}\right]}$$

where *%HF* is the proportion of hydrothermal fluid and the subscripts *SW*, *M*, and *HF* refer to Sr concentrations and $^{87}Sr/^{86}Sr$ ratios values of these in seawater, measured values (in barite), and hydrothermal fluids, respectively. Strontium concentrations $[Sr]_{HF}$ and Sr isotope compositions $(^{87}Sr/^{86}Sr)_{HF}$ of vent fluids were assumed to be similar to vent fluid samples from the modern PACMANUS hydrothermal field (Table 7; Reeves et al. 2011), as this is a valid modern analogue to the Lemarchant deposit (e.g., Gill et al. 2016). The measured Sr concentrations $[Sr]_M$ Sr isotope composition $(^{87}Sr/^{86}Sr)_M$ are the calculated averages from our microprobe data, and $[Sr]_{SW}$ is the measured Sr concentration of seawater at 3 °C at the PACMANUS hydrothermal vent field (Reeves et al. 2011).

Mixing equations above suggest that the relative hydrothermal fluid contribution for Lemarchant barite range between 37% to 51% (av. 45%) (Table 5). The consistency of Sr- and S-isotopic data in barite from Lemarchant, and the lack of correlation between Sr/Ba ratios and calculated relative contribution hydrothermal fluids (Fig. 16), suggest that Sr substitution in barite was not controlled by fluctuations in fluid composition/mixing during precipitation (e.g., Jamieson et al. 2016). Rather, Sr substitution in barite was likely controlled by temperature variations caused by conductive cooling within chimney walls (Jamieson et al. 2016). Moreover, the paragenesis, the mineral assemblages, and the sulphide geochemistry of the Lemarchant deposit reflect varying physicochemical conditions during deposit formation (Gill et al. 2015, 2016), and further support the model that temperature fluctuations may have contributed to the variable substitution of Sr in barite.

Nature and origin of CO_2-rich fluid inclusions

Three types of fluid inclusions were identified in bladed barite from the massive sulphide lenses: (1) type-I aqueous carbonic, (2) type-II aqueous two-phase (± CO_2), and (3) type-III vapor-rich

Fig. 16. [Sr]/[Ba] ratio from whole-rock geochemistry results of barite versus %hydrothermal fluid for barite in the Lemarchant deposit. [Colour online.]

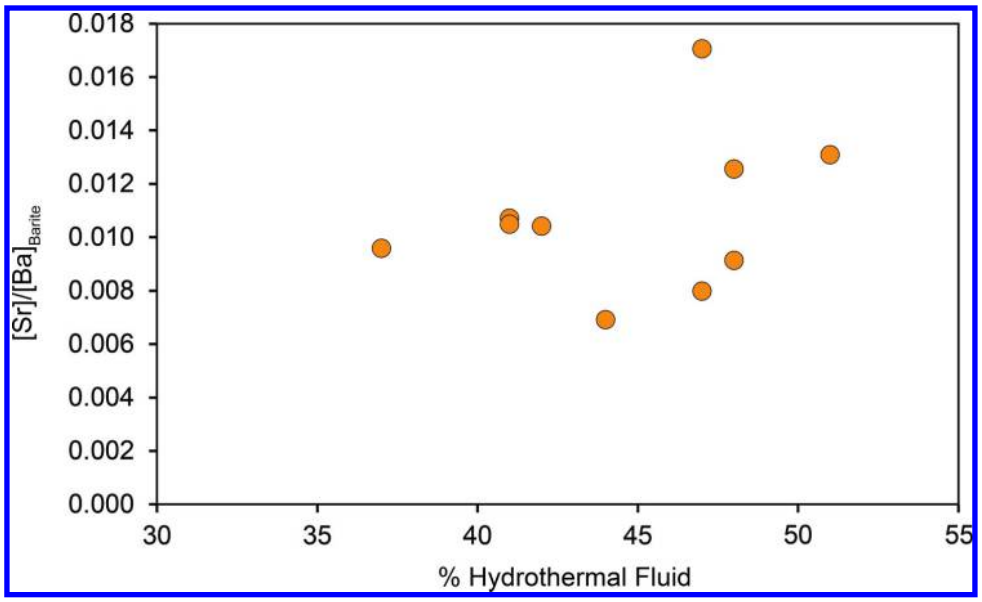

inclusions (± CO_2?). All inclusion assemblages appear in primary growth zones, with aqueous carbonic fluids being the most abundant type in bladed barite, with low salinities (avg. 1.2 wt.% NaCl equivalent) and average T_h between 245–250 °C. Pressure estimates for the type-I fluid inclusion are between 1.7 to 2.0 kbars (approximately 6.4 to 7.2 km depth). Most modern massive sulphides at ridges occur below 1500 m water depth and in back-arc basins most known VMS are at depths of approximately 1500 to 2000 m, at pressures of 0.15 to 0.20 kbars, with no known deposits at depth of >5000 m (Monecke et al. 2014). Thus, the pressure estimates from the inclusions are inconsistent with the depths typical of seafloor VMS systems in arcs and back-arc basins, the inferred setting for the Lemarchant deposit (e.g., Cloutier et al. 2017). Additionally, VMS deposits typically contain two-phase inclusions, with salinities near seawater values (2–6 wt.% NaCl equivalent), and low CO_2 (Bodnar et al. 2014). Although T_h for fluid inclusions at Lemarchant are within the range of VMS mineralization (i.e., approximately 100–300 °C), their low salinity and high density are similar to fluid inclusions described in metamorphic terranes (Bodnar et al. 2014).

The T_h recorded in type-I fluid inclusions represent minimum trapping conditions. By using T_h and pressure data calculated from type-I inclusions, we can extrapolate the possible conditions of trapping through isochoric trajectories on a P–T plot in an H_2O-rich isopleth of the CO_2–H_2O system (Fig. 17) (Diamond 2003). The calculated isochores show that the trapping conditions for aqueous–carbonic fluid inclusions in bladed barite fall within the greenschist facies metamorphic field. Although the carbonic-rich fluid inclusions demonstrate no significant evidence of textural change from deformation and metamorphism, the anomalous calculated pressures suggest that fluid diffusion occurred during post-VMS (i.e., Silurian to Devonian) tectonism. The measured and calculated trapping conditions of the carbonic-rich inclusion are consistent with the results of previous workers who have demonstrated that barite is particularly susceptible to stretching and leaking (Ulrich and Bodnar 1988). Hence, despite textural preservation, it is likely that the Lemarchant fluid inclusions leaked and (or) may have been refilled by a younger metamorphism-related overprinting fluid event(s) and must be considered secondary inclusions.

Regionally, three-phase carbonic-rich fluid inclusions similar to those observed in the Lemarchant deposit have been recorded in both the Midas Pond (Evans 1993) and Valentine Lake deposits (J. Conliffe, personal observation, 2012) in the Victoria Lake supergroup. Boulanger et al. (2010) recorded similar carbonic-rich fluid inclusions in the primary ore in the Ming deposit in northeast

Fig. 17. Schematic pressure–temperature (P–T) projection of metamorphic facies. The orange field represents the range of isochores calculated for type-I aqueous–carbonic fluid inclusions in bladed barite. Our data suggest that type-I fluid inclusions are refilled primary fluid inclusions during circulation of greenschist facies metamorphic fluids. Our data are in agreement with the regional metamorphic grade of the Victoria Lake Supergroup. Isochores were calculated using the equation of states of Anderko and Pitzer (1993) and Duan et al. (1995). Metamorphic facies diagram modified from Spear 1993. And; andalusite; Ky, kyanite; Sil, sillimanite. [Colour online.]

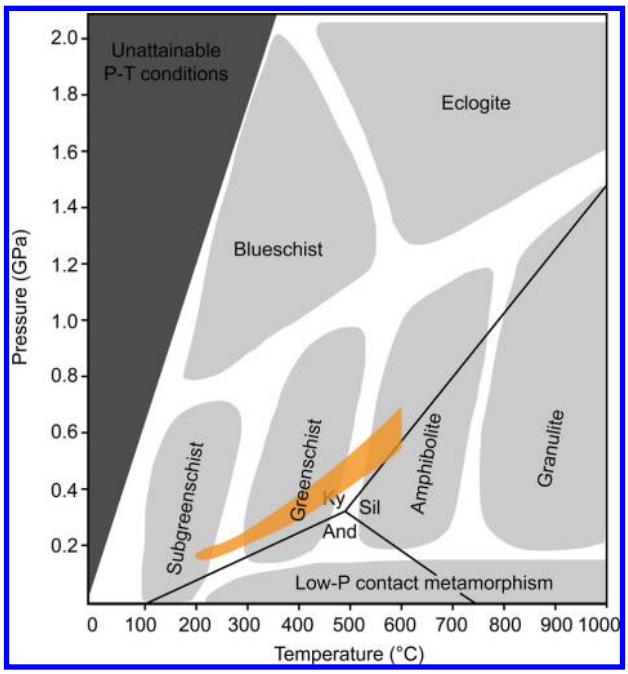

Newfoundland, which they interpreted to be secondary and related to the circulation of CO_2-rich fluids during regional metamorphism. These observations suggest that circulation of regional CO_2-rich metamorphic fluids did occur within the Victoria Lake supergroup and it is highly likely that they overprinted primary fluid inclusion assemblages.

The association of CO_2-rich fluids with younger (i.e., Silurian–Devonian) orogenic Au activity leads to the possibility that Au–Ag-enrichment in the Lemarchant deposit was to the result of a post-VMS orogenic overprint. This is unlikely for a number of reasons. Firstly, Au-enrichment is restricted to the Lemarchant deposit and not found in any rocks outside the immediate massive sulphide mineralization (i.e., Au does not extend along faults outside the massive sulphide horizon, nor is it present in quartz veins vis-à-vis orogenic Au regionally). Secondly, the mineralization has distinctive intermediate- to high-sulphidation epithermal suite/sulphosalt-rich mineral assemblages (e.g., tetrahedrite-group minerals, bornite, covellite, electrum, and other sulphosalts), interpreted to be syngenetic and derived from magmatic fluids (Gill et al. 2016), minerals notably absent in orogenic Au deposits regionally (e.g., Evans et al. 1990). Finally, the alteration assemblages associated with Au in the Lemarchant deposit are generally Fe–carbonate poor (Cloutier et al. 2017), typical of global VMS deposits (Galley et al. 2007), and unlike those in orogenic Au deposits of the Newfoundland Appalachians and globally (Evans and Wilson 1994; Groves et al. 1998; McCuaig and Kerrich 1998; Ramezani et al. 2000; Goldfarb et al. 2001).

Conclusions

Barite in the Lemarchant VMS deposit is spatially associated with unique sulphide mineral assemblages and shows distinctive textures, which are atypical of most VMS deposits. Granular barite is associated with all types of mineralization, whereas bladed textured barite is associated with sulphosalt- and precious-metal-enriched mineral assemblages with enrichments in Sb–Ag–As–Au and Ga–Mo–Hg–Tl–V. In certain samples of bladed barite there are microinclusions of sulphide minerals in pseudo-secondary fluid inclusion trails. It is suggested that the sulphide inclusions were "captured" mineral phases during barite formation from the hydrothermal plume, rather than having formed as daughter minerals. Barite geochemistry showed little compositional variations and is stoichiometric, although Sr concentrations vary in both granular and bladed barite showing a negative correlation with Ba. The variable substitution of Sr in barite was likely controlled by temperature fluctuations rather than fluid mixing with greater Sr contents reflecting increased conductive cooling for barite formation (Jamieson et al. 2016). Barite generally contains low concentrations of trace elements that are at or below detection limits by both EPMA and LA–ICP–MS.

The S-isotope compositions of barite suggest that Cambrian seawater was the main source of sulphur in the barite, whereas Sr isotopes reflect mixing of seawater and ancient crustal sources, likely the underlying basement (Neoproterozoic Sandy Brook Group). These data support a model where hydrothermal fluid leached Ba and Sr from the underlying basement and mixed with SO_4 in Cambrian seawater. Our results agree with other isotopic studies of host rocks and sulphides and the regional geology of the Tally Pond Group.

All fluid and inclusion assemblages in Lemarchant bladed barite appear to be in primary growth zones and are dominated by aqueous carbonic fluids. Low salinities, high internal pressures, and high formation temperatures are characteristic of type-I inclusions in bladed barite. However, elevated T_h and calculated pressures of formation for the aqueous–carbonic inclusions are secondary and are interpreted to be refilled primary inclusions that were influenced by CO_2-rich metamorphic fluids possibly during Silurian regional greenschist metamorphism.

The data presented in this this study are comparable with present-day barite-rich hydrothermal systems on the seafloor and suggests that the Lemarchant barites formed in a manner similar to younger, Kuroko-style mineralization.

Acknowledgements

This project was supported by an NSERC Alexander Graham Bell Canada Graduate Scholarship to the first author as part of a M.Sc. project. Additional funding was provided by the NSERC Altius Industrial Research Chair in Mineral Deposits supported by NSERC, Altius Resources Inc., the Research and Development Corporation of Newfoundland and Labrador, and an NSERC Discovery Grant to S. Piercey. Access to the Lemarchant drill core, core logs, and assay database, and logistical support were provided by NorZinc Ltd. (formerly Canadian Zinc Corporation). Many thanks to those who helped with analytical data acquisition, including Evelyne Leduc (Queen's University), Dr. Wanda Aylward, Sherri Strong, Matthew Crocker, and Dr. Dave Grant (Memorial University). A special thanks to Dr. Stefanie Brueckner for her guidance with laser ablation data reduction. We thank Associate Editor Dr. Erin Adlakha and reviewers Dr. Steve Hollis and Dr. Melissa Anderson for their reviews and comments on an earlier draft of this manuscript, which have greatly improved this manuscript.

References

Albarède, F., Michard, A., Minster, J., and Michard, G. 1981. $^{87}Sr/^{86}Sr$ ratios in hydrothermal waters and deposits from the East Pacific Rise at 21 N. Earth and Planetary Science Letters, **55**: 229–236. doi:10.1016/0012-821X(81)90102-3.

Anderko, A., and Pitzer, K.S. 1993. Phase equilibria and volumetric properties of the systems KCl-H_2O and NaCl-KCl-H_2O above 573K: Equation of state representation. Geochimica et Cosmochimica Acta, **57**: 4885–4897. doi:10.1016/0016-7037(93)90127-I.

Asmerom, Y., Jacobsen, S.B., Knoll, A.H., Butterfield, N.J., and Swett, K. 1991. Strontium isotopic variations of Neoproterozoic seawater: implications for crustal evolution. Geochimica et Cosmochimica Acta, **55**: 2883–2894. doi:10.1016/0016-7037(91)90453-C.

Averyt, K.B., and Paytan, A. 2003. Empirical partition coefficients for Sr and Ca in marine barite: Implications for reconstructing seawater Sr and Ca concentrations. Geochemistry, Geophysics, Geosystems, **4**: 1043. doi:10.1029/2002GC000426.

Ayuso, R.A., and Schulz, K.J. 2003. Nd-Pb-Sr isotope geochemistry and origin of the Ordovician Bald Mountain and Mount Chase massive sulfide deposits, northern Maine. Massive Sulfide Deposits of the Bathurst Mining Camp, New Brunswick, and Northern Maine. Economic Geology Monograph, **11**: 611–630.

Bakker, R.J. 1997. Clathrates: Computer programs to calculate fluid inclusion V-X properties using clathrate melting temperatures. Computers and Geosciences, **23**: 1–18. doi:10.1016/S0098-3004(96)00073-8.

Bakker, R.J. 1998. Improvements in clathrate modelling II: The H_2O-CO_2-CH_4-N_2-C_2H_6 fluid system. Geological Society, London, Special Publications, **137**: 75–105. doi:10.1144/GSL.SP.1998.137.01.06.

Bakker, R.J., and Brown, P.E. 2003. Computer modelling in fluid inclusion research. *In* Fluid inclusions: Analysis and interpretation, Vol. 32, pp. 175–212.

Bakker, R.J., Dubessy, J., and Cathelineau, M. 1996. Improvements in clathrate modelling: I. the H_2O-CO_2 system with various salts. Geochimica et Cosmochimica Acta, **60**: 1657–1681. doi:10.1016/0016-7037(96)00032-4.

Berner, R.A. 2004. A model for calcium, magnesium and sulphate in seawater over Phanerozoic time. American Journal of Science, **304**: 438–453. doi:10.2475/ajs.304.5.438.

Binns, R.A., Scott, S.D., Bogdanov, Y.A., Lisitzin, A.P., Gordeev, V.V., Gurvich, E.G., et al. 1993. Hydrothermal oxide and gold-rich sulphate deposits of Franklin Seamount, western Woodlark Basin, Papua New Guinea. Economic Geology, **88**: 2122–2153. doi:10.2113/gsecongeo.88.8.2122.

Bischoff, J.L., and Seyfried, W.E. 1978. Hydrothermal chemistry of seawater from 25 degrees to 350 degrees C. American Journal of Science, **278**: 838–860. doi:10.2475/ajs.278.6.838.

Bischoff, J.L., and Rosenbauer, R.J. 1985. An empirical equation of state for hydrothermal seawater (3.2 percent NaCl). American Journal of Science, **285**: 725–763. doi:10.2475/ajs.285.8.725.

Blount, C. 1977. Barite solubilities and thermodynamic quantities up to 300 °C and 1400 bars. American Mineralogist, **62**(9–10): 942–957.

Bodnar, R.J., and Vityk, M.O. 1994. Interpretation of microthermometric data for H_2O-NaCl fluid inclusions. *In* Fluid inclusions in minerals: methods and applications. IMA Short Course, pp. 117–130.

Bodnar, R.J., Lecumberri-Sanchez, P., Moncada, D., and Steele-MacInnis, M. 2014. Fluid inclusions in hydrothermal ore deposits. *In* Treatise on geochemistry, 2nd ed. Elsevier, Oxford. pp. 119–142.

Boström, K., Frazer, J., and Blankenburg, J. 1967. Subsolidus phase relations and

lattice constants in the system $BaSO_4$-$SrSO_4$-$PbSO_4$. Arkiv för kemi, mineralogi och geologi, **4**: 477–485.

Boulanger, R.A., Chi, G., Skulski, T., and Castonguay, S. 2010. Characterization and evolution of fluids associated with the Cu-Au deposit of the Ming Mine, Rambler area, northeast Newfoundland, Canada. *In* GeoCanada 2010 – Working with the Earth: 5.

Burke, W., Denison, R., Hetherington, E., Koepnick, R., Nelson, H., and Otto, J. 1982. Variation of seawater $^{87}Sr/^{86}Sr$ throughout Phanerozoic time. Geology, **10**: 516–519. doi:10.1130/0091-7613(1982)10<516:VOSSTP>2.0.CO;2.

Buschette, M.J., and Piercey, S.J. 2016. Hydrothermal alteration and lithogeochemistry of the Boundary volcanogenic massive sulphide deposit, central Newfoundland, Canada. Canadian Journal of Earth Sciences, **53**(5): 506–527. doi:10.1139/cjes-2015-0237.

Butterfield, D.A., Massoth, G.J., McDuff, R.E., Lupton, J.E., and Lilley, M.D. 1990. Geochemistry of hydrothermal fluids from Axial Seamount hydrothermal emissions study vent field, Juan de Fuca ridge: Subseafloor boiling and subsequent fluid-rock interaction. Journal of Geophysical Research: Solid Earth, **95**: 12895–12921. doi:10.1029/JB095iB08p12895.

Butterfield, D.A., Jonasson, I.R., Massoth, G.J., Feely, R.A., Roe, K.K., Embley, R.E., et al. 1997. Seafloor eruptions and evolution of hydrothermal fluid chemistry. Philosophical Transactions of the Royal Society of London A: Mathematical, Physical and Engineering Sciences, **355**: 369–386. doi:10.1098/rsta.1997.0013.

Claypool, G.E., Holser, W.T., Kaplan, I.R., Sakai, H., and Zak, I. 1980. The age curves of sulphur and oxygen isotopes in marine sulphate and their mutual interpretation. Chemical Geology, **28**: 199–260. doi:10.1016/0009-2541(80)90047-9.

Cloutier, J., Piercey, S.J., Lode, S., Guchte, M.V., and Copeland, D.A. 2017. Lithostratigraphic and structural reconstruction of the Zn-Pb-Cu-Ag-Au Lemarchant volcanogenic massive sulphide (VMS) deposit, Tally Pond group, central Newfoundland, Canada. Ore Geology Reviews, **84**: 154–173. doi:10.1016/j.oregeorev.2017.01.010.

Colman-Sadd, S.P., Dunning, G., and Dec, T. 1992. Dunnage-Gander relationships and Ordovician orogeny in central Newfoundland; a sediment provenance and U-Pb age study. American Journal of Science, **292**: 317–355. doi:10.2475/ajs.292.5.317.

Copeland, D.A., Toole, R.M.S., and Piercey, S.J. 2008*a*. Assessment report on diamond drilling and soil sampling, License 8183M (10th year) and 9569M (5th year) South Tally Pond property, Rogerson Lake area, Newfoundland and Labrador, NTS 12A/10 and 12A/07; Newfoundland and Labrador Geological Survey, Assessment Report, p. 956.

Copeland, D.A., McClenaghan, S.M., and Piercey, S.J. 2008*b*. Ninth year assessment report on diamond drilling, lithogeochemistry, pulse EM surveying and linecutting on license 8183M, South Tally Pond Property, Rogerson Lake area, Newfoundland and Labrador NTS 12A/10 and 12A/07. Newfoundland and Labrador Geological Survey, Assessment Report, 91 pp. [for Paragon Minerals and Altius Minerals|.

de Ronde, C.E. 1995. Fluid chemistry and isotopic characteristics of seafloor hydrothermal systems and associated VMS deposits: potential for magmatic contributions. Magmas, fluids, and ore deposits. Mineralogical Association of Canada, Short Course Series, **23**: 479–509.

de Ronde, C.E., Hannington, M.D., Stoffers, P., Wright, I.C., Ditchburn, R.G., Reyes, A.G., et al. 2005. Evolution of a submarine magmatic-hydrothermal system: Brothers volcano, southern Kermadec arc, New Zealand. Economic Geology, **100**: 1097–1133. doi:10.2113/gsecongeo.100.6.1097.

Denison, R.E., Koepnick, R.B., Burke, W.H., and Hetherington, E.A. 1998. Construction of the Cambrian and Ordovician seawater $^{87}Sr/^{86}Sr$ curve. Chemical Geology, **152**: 325–340. doi:10.1016/S0009-2541(98)00119-3.

Derry, L.A., Keto, L.S., Jacobsen, S.B., Knoll, A.H., and Swett, K. 1989. Sr isotopic variations in Upper Proterozoic carbonates from Svalbard and East Greenland. Geochimica et Cosmochimica Acta, **53**: 2331–2339. doi:10.1016/0016-7037(89)90355-4.

Derry, L.A., Brasier, M.D., Corfield, R.E.A., Rozanov, A.Y., and Zhuravlev, A.Y. 1994. Sr and C isotopes in Lower Cambrian carbonates from the Siberian craton: a paleoenvironmental record during the 'Cambrian explosion'. Earth and Planetary Science Letters, **128**: 671–681. doi:10.1016/0012-821X(94)90178-3.

Diamond, L.W. 2001. Review of the systematics of CO2–H2O fluid inclusions. Lithos, **55**: 69–99. doi:10.1016/S0024-4937(00)00039-6.

Diamond, L.W. 2003. Introduction to gas-bearing, aqueous fluid inclusions. Fluid Inclusions: Analysis and Interpretation, **32**: 101–158.

Drummond, S., and Ohmoto, H. 1985. Chemical evolution and mineral deposition in boiling hydrothermal systems. Economic Geology, **80**: 126–147. doi:10.2113/gsecongeo.80.1.126.

Duan, Z., Møller, N., and Weare, J.H. 1995. Equation of state for the NaCl-H_2O-CO_2 system: prediction of phase equilibria and volumetric properties. Geochimica et Cosmochimica Acta, **59**: 2869–2882. doi:10.1016/0016-7037(95)00182-4.

Dunning, G.R., O'Brien, S.J., Colman-Sadd, S.P., Blackwood, R.F., Dickson, W.L., O'Neill, P.P., and Krogh, T.E. 1990. Silurian Orogeny in the Newfoundland Appalachians. The Journal of Geology, **98**: 895–913 doi:10.1086/629460.

Dunning, G.R., Swinden, H.S., Kean, B., Evans, D., and Jenner, G. 1991. A Cambrian island arc in Iapetus: Geochronology and geochemistry of the Lake Ambrose volcanic belt, Newfoundland Appalachians. Geological Magazine, **128**: 1–17. doi:10.1017/S0016756800018008.

Eldridge, C.S., Barton, P., and Ohmoto, H. 1983. Mineral textures and their bearing on formation of the Kuroko orebodies. Economic Geology Monograph, **5**: 241–281.

Elsgaard, L., Isaksen, M.F., Jørgensen, B.B., Alayse, A.M., and Jannasch, H.W. 1994. Microbial sulphate reduction in deep-sea sediments at the Guaymas Basin hydrothermal vent area: influence of temperature and substrates. Geochimica et Cosmochimica Acta, **58**: 3335–3343. doi:10.1016/0016-7037(94)90089-2.

Evans, D.T.W. 1993. The Midas Pond gold prospect, Victoria Lake Group: geology, alteration and mineralization. Unpublished M.Sc. thesis, Department of Earth Sciences, Memorial University of Newfoundland, St. John's, NL.

Evans, D.T.W., and Kean, B. 2002. The Victoria Lake supergroup, central Newfoundland-its definition, setting and volcanogenic massive sulphide mineralization. Newfoundland and Labrador Department of Mines and Energy, Geological Survey, Open File NFLD/2790, 68 p.

Evans, D.T.W., and Wilson, M.R. 1994. Epigenetic gold occurrences in the eastern Dunnage Zone, Newfoundland: preliminary stable isotope results. Current Research Report, 94-1: St. John's, Newfoundland, Geological Survey Branch.

Evans, D.T.W., Kean, B.F., and Dunning, G.R. 1990. Geological studies, Victoria Lake supergroup, central Newfoundland. Current Research Report 90-1: St. John's, Newfoundland, Geological Survey Branch, pp. 131–144.

Farrell, C.W., and Holland, H.D. 1983. Strontium isotope geochemistry of the Kuroko deposits. Economic Geology Monograph, **5**: 302–319.

Farrell, C., Holland, H., and Petersen, U. 1978. The isotopic composition of strontium in barites and anhydrites from Kuroko deposits. Mining Geology, **28**: 281–291. doi:10.11456/shigenchishitsu1951.28.281.

Fraser, D., Giroux, G.H., Copeland, D.A., and Devine, C.A. 2012. NI-43-101 technical report and mineral resource estimate on the Lemarchant deposit, South Tally Pond VMS project, central Newfoundland, Canada. Paragon Minerals Corporation.

Galley, A.G., Hannington, M.D., and Jonasson, I.R. 2007. Volcanogenic massive sulphide deposits. *In* Mineral Deposits of Canada: A Synthesis of Major Deposit-Types, District Metallogeny, the Evolution of Geological Provinces, and Exploration Methods. *Edited by* W.D. Goodfellow. Geological Association of Canada, Mineral Deposits Division, Special Publication No. 5, pp. 141–161.

Gartman, A., Hannington, M., Jamieson, J.W., Peterkin, B., Garbe-Schönberg, D., Findlay, A.J., Fuchs, S., and Kwasnitschka, T. 2018. Boiling-induced formation of colloidal gold in black smoker hydrothermal fluids. Geology, **46**: 39–42. doi:10.1130/G39492.1.

Gill, S.B. 2015. Mineralogy, metal zoning, and genesis of the Cambrian Zn-Pb-Cu-Ag-Au Lemarchant volcanogenic massive sulfide (VMS) deposit. M.Sc. thesis, Department of Earth Sciences, Memorial University of Newfoundland, St. John's, Newfoundland.

Gill, S.B., and Piercey, S.J. 2014. Preliminary observations on styles of mineralization and sulfide-mineral zonation in the Cambrian Zn-Pb-Cu-Ag-Au Lemarchant volcanogenic massive-sulphide deposit, Newfoundland and Labrador; Geological Survey of Canada, Current Research 2014-5, p. 17.

Gill, S.B., Piercey, S., Layton-Matthews, D., Layne, G., and Piercey, G. 2015. Mineralogical, sulphur, and lead isotopic study of the Lemarchant Zn-Pb-Cu-Ag-Au-VMS deposit: Implications for precious-metal enrichment processes in the VMS environment. Targeted Geoscience Initiative, **4**: 183–195.

Gill, S.B., Piercey, S.J., and Layton-Matthews, D. 2016. Mineralogy and Metal Zoning of the Cambrian Zn-Pb-Cu-Ag-Au Lemarchant Volcanogenic Massive Sulfide (VMS) Deposit, Newfoundland. The Canadian Mineralogist, **54**: 1307–1344. doi:10.3749/canmin.1500069.

Goldfarb, M., Converse, D., Holland, H., and Edmond, J. 1983. The genesis of hot spring deposits on the East Pacific Rise, 21 N. Economic Geology Monograph, **5**: 184–197.

Goldfarb, R.J., Groves, D.I., and Gardoll, S. 2001. Orogenic gold and geologic time: a global synthesis. Ore Geology Reviews, **18**: 1–75. doi:10.1016/S0169-1368(01)00016-6.

Goldstein, S.J., and Jacobsen, S.B. 1988. Nd and Sr isotopic systematics of river water suspended material: implications for crustal evolution. Earth and Planetary Science Letters, **87**: 249–265. doi:10.1016/0012-821X(88)90013-1.

Griffith, E.M., and Paytan, A. 2012. Barite in the ocean–occurrence, geochemistry and palaeoceanographic applications. Sedimentology, **59**: 1817–1835. doi:10.1111/j.1365-3091.2012.01327.x.

Groves, D.I., Goldfarb, R.J., Gebre-Mariam, M., Hagemann, S.G., and Robert, E. 1998. Orogenic gold deposits - a proposed classification in the context of their crustal distribution and relationship to other gold deposit types. Ore Geology Reviews, **13**: 7–27. doi:10.1016/S0169-1368(97)00012-7.

Habicht, K.S., and Canfield, D.E. 2001. Isotope fractionation by sulphate-reducing natural populations and the isotopic composition of sulfide in marine sediments. Geology, **29**: 555–558. doi:10.1130/0091-7613(2001)029<0555:IFBSRN>2.0.CO;2.

Halbach, P., Nakamura, K.I., Wahsner, M., Lange, J., Sakai, H., Käselitz, L., et al. 1989. Probable modern analogue of Kuroko-type massive sulphide deposits in the Okinawa Trough back-arc basin. Nature, **338**: 496–499. doi:10.1038/338496a0.

Hannington, M.D., and Scott, S.D. 1988. Mineralogy and geochemistry of a hydrothermal silica-sulfide-sulphate spire in the caldera of Axial Seamount, Juan de Fuca Ridge. The Canadian Mineralogist, **26**: 603–625.

Hannington, M.D., and Monecke, T. 2009. Modern submarine hydrothermal systems — A global perspective on distribution, size and tectonic settings. *In* Submarine Volcanism and Mineralization: Modern through Ancient. *Edited by*

B. Cousens and S.J. Piercey; Geological Association of Canada, Mineral Deposits Division, Short Course Notes, v. 19, p. 91–146.

Hannington, M.D., Herzig, P.M., Scott, S.D., Thompson, G., and Rona, P. 1991. Comparative mineralogy and geochemistry of gold-bearing sulfide deposits on the mid-ocean ridges. Marine Geology, **101**: 217–248. doi:10.1016/0025-3227(91)90073-D.

Hannington, M.D., Jonasson, I.R., Herzig, P.M., and Petersen, S. 1995. Physical and chemical processes of seafloor mineralization at mid-ocean ridges. Seafloor Hydrothermal Systems: Physical, Chemical, Biological, and Geological Interactions Geophysical Monograph, **91**: 115–157. doi:10.1029/GM091p0115.

Hannington, M.D., de Ronde, C., and Sven Petersen, D.J. 2005. *Sea-floor tectonics and submarine hydrothermal systems*. Economic Geology 100th Anniversary Volume. Society of Economic Geologists, Littleton, Colorado, USA, pp. 111–141.

Hannington, M., Harðardóttir, V., Garbe-Schönberg, D., and Brown, K. 2016. Gold enrichment in active geothermal systems by accumulating colloidal suspensions. Nature Geoscience, **9**: 299–302. doi:10.1038/ngeo2661.

Hanor, J.S. 2000. Barite–celestine geochemistry and environments of formation. Reviews in Mineralogy and Geochemistry, **40**: 193–275. doi:10.2138/rmg.2000.40.4.

Herzig, P.M., Hannington, M.D., and Arribas, A., Jr. 1998. Sulphur isotopic composition of hydrothermal precipitates from the Lau back-arc: implications for magmatic contributions to seafloor hydrothermal systems. Mineralium Deposita, **33**: 226–237. doi:10.1007/s001260050143.

Hill, A.P. 1996. Structure, volcanic setting, hydrothermal alteration and genesis of the Thalanga massive sulphide deposit. Ph.D. thesis, Department of Earth Sciences, University of Tasmania, Hobart, Tasmania.

Huston, D.L. 1997. Stable isotopes and their significance for understanding the genesis of volcanic-hosted massive sulfide deposits: A review. *In* Volcanic Associated Massive Sulfide Deposits: Processes and examples in Modern and Ancient Settings. Reviews in Economic Geology, **8**: 157–179. doi:10.5382/Rev.08.07.

Huston, D.L., and Large, R.R. 1989. A chemical model for the concentration of gold in volcanogenic massive sulphide deposits. Ore Geology Reviews, **4**: 171–200. doi:10.1016/0169-1368(89)90017-6.

Huston, D.L., Relvas, J.M., Gemmell, J.B., and Drieberg, S. 2011. The role of granites in volcanic-hosted massive sulphide ore-forming systems: an assessment of magmatic–hydrothermal contributions. Mineralium Deposita, **46**: 473–507. doi:10.1007/s00126-010-0322-7.

Jamieson, J.W., Hannington, M.D., Tivey, M.K., Hansteen, T., Williamson, N.M.B., Stewart, M., et al. 2016. Precipitation and growth of barite within hydrothermal vent deposits from the Endeavour Segment, Juan de Fuca Ridge. Geochimica et Cosmochimica Acta, **173**: 64–85. doi:10.1016/j.gca.2015.10.021.

Janecky, D.R., and Shanks, W.C., III. 1988. Computational modeling of chemical and sulphur isotopic reaction processes in seafloor hydrothermal systems: chimneys, massive sulfides, and subjacent alterations zones. The Canadian Mineralogist, **26**: 805–825.

Jochum, K.P., Nohl, U., Herwig, K., Lammel, E., Stoll, B., and Hofmann, A.W. 2005. GeoReM: a new geochemical database for reference materials and isotopic standards. Geostandards and Geoanalytical Research, **29**: 333–338. doi:10.1111/j.1751-908X.2005.tb00904.x.

Kalogeropoulos, S.I., and Scott, S.D. 1983. Mineralogy and geochemistry of tuffaceous exhalites (Tetsusekiei) of the Fukazawa mine, Hokuroku district, Japan. Economic Geology Monograph, **5**: 412–432.

Kalogeropoulos, S.I., and Scott, S.D. 1989. Mineralogy and geochemistry of an Archean tuffaceous exhalite: The main contact tuff, Millenbach mine area, Noranda, Quebec. Canadian Journal of Earth Sciences, **26**(1): 88–105. doi:10.1139/e89-008.

Koski, R.A., Jonasson, I.R., Kadko, D.C., Smith, V.K., and Wong, F.L. 1994. Compositions, growth mechanisms, and temporal relations of hydrothermal sulfide-sulphate-silica chimneys at the northern Cleft Segment, Juan de Fuca Ridge. Journal of Geophysical Research: Solid Earth, **99**: 4813–4832. doi:10.1029/93JB02871.

Kowalik, J., Rye, R.O., and Sawkins, F.J. 1981. Stable isotope study of the Buchans, Newfoundland, polymetallic sulphide deposits. Geological Association of Canada, Special Paper, **22**: 229–254.

Kusakabe, M., and Chiba, H. 1983. Oxygen and sulphur isotope composition of barite and anhydrite from the Fukazawa deposit, Japan. Economic Geology Monograph, **5**: 292–301.

Large, R.R. 1992. Australian volcanic-hosted massive sulfide deposits: Features, styles, and genetic models. Economic Geology, **87**: 549–572. doi:10.2113/gsecongeo.87.3.471.

Lode, S., Piercey, S.J., and Devine, C.A. 2015. Geology, mineralogy, and lithogeochemistry of metalliferous mudstones associated with the Lemarchant volcanogenic massive sulfide deposit, Tally Pond group, central Newfoundland. Economic Geology, **110**: 1835–1859. doi:10.2113/econgeo.110.7.1835.

Lydon, J.W. 1984. Volcanogenic massive sulfide deposits Part I: A descriptive model. Geoscience Canada, **11**: 195–202.

Marchev, P., Downes, H., Thirlwall, M.F., and Moritz, R. 2002. Small-scale variations of $^{87}Sr/^{86}Sr$ isotope composition of barite in the Madjarovo low-sulphidation epithermal system, SE Bulgaria: implications for sources of Sr, fluid fluxes and pathways of the ore-forming fluids. Mineralium Deposita, **37**: 669–677. doi:10.1007/s00126-002-0278-3.

McCuaig, T.C., and Kerrich, R. 1998. P-T-t-deformation-fluid characteristics of lode gold deposits: evidence from alteration systematics. Ore Geology Reviews, **12**: 381–453. doi:10.1016/S0169-1368(98)80002-4.

McNicoll, V., Squires, G., Kerr, A., and Moore, P. 2008. Geological and metallogenic implications of U-Pb zircon geochronological data from the Tally Pond area, central Newfoundland. Current research. Newfoundland and Labrador Department of Natural Resources, Report 08-1, pp. 173–192.

McNicoll, V., Squires, G., Kerr, A., and Moore, P. 2010. The Duck Pond and Boundary Cu-Zn deposits, Newfoundland: New insights into the ages of host rocks and the timing of VHMS mineralization. Canadian Journal of Earth Sciences, **47**(12): 1481–1506. doi:10.1139/E10-075.

Mills, R., Teagle, D., and Tivey, M. 1998. Fluid mixing and anhydrite precipitation within the TAG mound. *In* Proceedings of the Ocean Drilling Program, Scientific Results, 158. *Edited by* P. Herzig, S. Humphris, D. Miller, and R. Zierenberg. Ocean Drilling Program, College Station, Tex., pp. 119–127.

Monecke, T., Petersen, S., and Hannington, M.D. 2014. Constraints on water depth of massive sulfide formation: Evidence from modern seafloor hydrothermal systems in arc-related settings. Economic Geology, **109**: 2079–2101. doi:10.2113/econgeo.109.8.2079.

Monnin, C., and Cividini, D. 2006. The saturation state of the world's ocean with respect to (Ba, Sr)SO_4 solid solutions. Geochimica et Cosmochimica Acta, **70**: 3290–3298. doi:10.1016/j.gca.2006.04.002.

Montañez, I.P., Banner, J.L., Osleger, D.A., Borg, L.E., and Bosserman, P.J. 1996. Integrated Sr isotope variations and sea-level history of Middle to Upper Cambrian platform carbonates: Implications for the evolution of Cambrian seawater $^{87}Sr/^{86}Sr$. Geology, **24**: 917–920. doi:10.1130/0091-7613(1996)024<0917:ISIVAS>2.3.CO;2.

Ohmoto, H. 1996. Formation of volcanogenic massive sulfide deposits: The Kuroko perspective. Ore Geology Reviews, **10**: 135–177. doi:10.1016/0169-1368(95)00021-6.

Ohmoto, H., and Goldhaber, M.B. 1997. Sulphur and carbon isotopes. Geochemistry of hydrothermal ore deposits, **3**: 517–611.

Ohmoto, H., and Rye, R.O. 1979. Isotopes of sulphur and carbon. *In* Geochemistry of hydrothermal ore deposits. 2nd ed. *Edited by* H.L. Barnes. Wiley, New York, pp. 509–567.

Ohmoto, H., Mizukami, M., Drummond, S.E., Eldridge, C.S., Pisutha-Arnond, V., and Lenagh, T.C. 1983. Chemical processes of Kuroko formation. Economic Geology Monographs, **5**: 570–604.

Paradis, S., Jonasson, I.R., Le Cheminant, G.M., and Watkinsons, D.H. 1988. Two zinc-rich chimneys from the Plume Site, southern Juan de Fuca Ridge. The Canadian Mineralogist, **26**: 637–654.

Paytan, A., Kastner, M., Martin, E., Macdougall, J., and Herbert, T. 1993. Marine barite as a monitor of seawater strontium isotope composition. Nature, **366**: 445–449. doi:10.1038/366445a0.

Piercey, S.J., and Hinchey, J. 2012. Volcanogenic massive sulphide (VMS) deposits of the Central Mineral Belt, Newfoundland. In Geological Association of Canada–Mineralogical Association of Canada Joint Annual Meeting, Field Trip Guidebook B, Newfoundland and Labrador Department of Natural Resources, Geological Survey, Open File NFLD/3173, 56 p.

Piercey, S.J., Squires, G.C., and Brace, T.D. 2014. Lithostratigraphic, hydrothermal, and tectonic setting of the Boundary volcanogenic massive sulfide deposit, Newfoundland Appalachians, Canada: formation by subseafloor replacement in a Cambrian rifted arc. Economic Geology, **109**: 661–687. doi:10.2113/econgeo.109.3.661.

Pollock, J.C. 2004. Geology of the Tally Pond group, Victoria Lake Supergroup, Dunnage Zone, Newfoundland: an integrated geochemical, geochronological, isotopic and metallogenic study of a Cambrian ensimatic island arc. Unpublished M. Sc. thesis, Department of Earth Sciences, Memorial University of Newfoundland, St. John's, NL.

Pollock, J.C., Wilton, D.H.C., van Staal, C.R., and Tubrett, M.N. 2002. Laser ablation ICP-MS geochronology and provenance of detrital zircons from the Rogerson Lake Conglomerate, Botwood Belt, Newfoundland. *In* Current research. Newfoundland Department of Mines and Energy, Geological Survey Branch, Report 02-1, p. 169-183.

Ramezani, J., Dunning, G.R., and Wilson, M.R. 2000. Geologic setting, geochemistry of alteration, and U-Pb age of hydrothermal zircon from the Silurian Stog'er Tight gold prospect, Newfoundland Appalachians, Canada. Exploration and Mining Geology, **9**: 171–188. doi:10.2113/0090171.

Ray, D., Banerjee, R., Balakrishnan, S., Paropkari, A.L., and Mukhopadhyay, S. 2017. S- and Sr-isotopic compositions in barite–silica chimney from the Franklin Seamount, Woodlark Basin, Papua New Guinea: constraints on genesis and temporal variability of hydrothermal fluid. International Journal of Earth Sciences, **106**: 1723–1733. doi:10.1007/s00531-016-1381-5.

Reeves, E.P., Seewald, J.S., Saccocia, P., Bach, W., Craddock, P.R., Shanks, W.C., et al. 2011. Geochemistry of hydrothermal fluids from the PACMANUS, northeast Pual and Vienna Woods hydrothermal fields, Manus Basin, Papua New Guinea. Geochimica et Cosmochimica Acta, **75**: 1088–1123. doi:10.1016/j.gca.2010.11.008.

Roedder, E. 1984. Fluid inclusions. Mineralogical Society of America. Reviews in Mineralogy, **12**: p. 644.

Roedder, E., and Bodnar, R.J. 1980. Geological pressure determinations from fluid inclusion studies. Annual Review of Earth and Planetary Sciences, **8**: 263–301. doi:10.1146/annurev.ea.08.050180.001403.

Roedder, E., and Coombs, D.S. 1967. Immiscibility in granitic melts, indicated by

fluid inclusions in ejected granitic blocks from Ascension Island. Journal of Petrology, **8**: 417–451. doi:10.1093/petrology/8.3.417.

Rogers, N., and van Staal, C.R. 2002. Toward a Victoria Lake Supergroup: a provisional stratigraphic revision of the Red Indian to Victoria Lakes area, central Newfoundland. Newfoundland and Labrador Department of Natural Resources, Geological Survey, Report 02-1, pp. 185–195.

Rogers, N., van Staal, C., McNicoll, V., Pollock, J., Zagorevski, A., and Whalen, J. 2006. Neoproterozoic and Cambrian arc magmatism along the eastern margin of the Victoria Lake supergroup: A remnant of Ganderian basement in central Newfoundland? Precambrian Research, **147**: 320–341. doi:10.1016/j.precamres.2006.01.025.

Rogers, N., van Staal, C., Zagorevski, A., Skulski, T., Piercey, S., and McNicoll, V. 2007. Timing and tectonic setting of volcanogenic massive sulphide bearing terranes within the Central Mobile Belt of the Canadian Appalachians. *In* Proceedings of Exploration 07: Fifth Decennial International Conference on Mineral Exploration. *Edited by* B. Milkereit. Toronto, Canada. pp. 1199–1205.

Rye, R.O. 1993. The evolution of magmatic fluids in the epithermal environment; the stable isotope perspective. Economic Geology, **88**: 733–752. doi:10.2113/gsecongeo.88.3.733.

Rye, R.O. 2005. A review of the stable-isotope geochemistry of sulphate minerals in selected igneous environments and related hydrothermal systems. Chemical Geology, **215**: 5–36. doi:10.1016/j.chemgeo.2004.06.034.

Sabine, P.A., and Young, B.R. 1954. Cell size and composition of the barytecelestine isomorphous series. Acta Crystallogr 7: 630 [abstract].

Safina, N.P., Melekestseva, I.Y., Nimis, P., Ankusheva, N.N., Yuminov, A.M., Kotlyarov, V.A., and Sadykov, S.A. 2016. Barite from the Saf'yanovka VMS deposit (central Urals) and Semenov-1 and Semenov-3 hydrothermal sulfide fields (Mid-Atlantic Ridge): A comparative analysis of formation conditions. Mineralium Deposita, **51**: 491–507. doi:10.1007/s00126-015-0617-9.

Sakai, H., Des Marais, D.J., Ueda, A., and Moore, J.G. 1984. Concentrations and isotope ratios of carbon, nitrogen and sulphur in ocean-floor basalts. Geochimica et Cosmochimica Acta, **48**: 2433–2441. doi:10.1016/0016-7037(84)90295-3.

Sangster, D. 1968. Relative sulphur isotope abundances of ancient seas and strata-bound sulphide deposits. *In* Proceedings of the Geological Association of Canada, 19, p. 79.

Scotney, P.M., Roberts, S., Herrington, R.J., Boyce, A.J., and Burgess, R. 2005. The development of volcanic hosted massive sulfide and barite–gold orebodies on Wetar Island, Indonesia. Mineralium Deposita, **40**: 76–99. doi:10.1007/s00126-005-0468-x.

Scott, S.D., and Barnes, H.L. 1971. Sphalerite geothermometry and geobarometry. Economic Geology, **66**: 653–669. doi:10.2113/gsecongeo.66.4.653.

Seal, R.R., II. 2006. Sulphur isotope geochemistry of sulfide minerals. Reviews in mineralogy and geochemistry, **61**: 633–677. doi:10.2138/rmg.2006.61.12.

Seal, R.R., II, Alpers, C.N., and Rye, R.O. 2000. Stable isotope systematics of sulphate minerals. Reviews in Mineralogy and Geochemistry, **40**: 541–602. doi:10.2138/rmg.2000.40.12.

Seal, R.R., II, Ayuso, R.A., Foley, N.K., and Clark, S.H. 2001. Sulphur and lead isotope geochemistry of hypogene mineralization at the Barite Hill gold deposit, Carolina Slate Belt, southeastern United States: A window into and through regional metamorphism. Mineralium Deposita, **36**: 137–148. doi:10.1007/s001260050294.

Shanks, W.C. 2001. Stable isotopes in seafloor hydrothermal systems: vent fluids, hydrothermal deposits, hydrothermal alteration, and microbial processes. Reviews in Mineralogy and Geochemistry, **43**: 469–525. doi:10.2138/gsrmg.43.1.469.

Sharpe, R. 1991. The Hellyer baritic and siliceous caps: Unpublished B.Sc. dissertation, Honors thesis, Department of Earth Sciences, University of Tasmania, Hobart, Tasmania.

Shepherd, T.J., Rankin, A.H., and Alderton, D. 1985. A practical guide to fluid inclusion studies. Blackie and Sons, Glasgow, p. 239.

Sherlock, R., Roth, T., Spooner, E., and Bray, C. 1999. Origin of the Eskay Creek precious metal-rich volcanogenic massive sulfide deposit; fluid inclusion and stable isotope evidence. Economic Geology, **94**: 803–824. doi:10.2113/gsecongeo.94.6.803.

Sillitoe, R.H., Hannington, M.D., and Thompson, J.F.H. 1996. High sulfidation deposits in the volcanogenic massive sulfide environment. Economic Geology, **91**: 204–212. doi:10.2113/gsecongeo.91.1.204.

Spear, F.S. 1993. Metamorphic phase equilibria and pressure-temperature-time paths, Mineralogical Society of America. Monograph, 1: 799p.

Squires, G.C., and Hinchey, J.G. 2006. Geology of the tally pond volcanic belt and adjacent areas (parts of NTS 12A/09 & 12A/10). Newfoundland and Labrador Department of Natural Resources, Geological Survey, Open file 12A/1202.

Squires, G., and Moore, P. 2004. Volcanogenic massive sulphide environments of the Tally Pond volcanics and adjacent area: Geological, lithogeochemical and geochronological results. Newfoundland and Labrador Department of Natural Resources, Geological Survey, Report 04-01: 63-91.

Squires, G., Brace, T., and Hussey, A. 2001. Newfoundland's polymetallic Duck Pond deposit: Earliest Iapetan VMS mineralization, formed within a subseafloor, carbonate-rich alteration system. Paper presented at the Geology and Mineral Deposits of the Northern Dunnage Zone, Newfoundland Appalachians. *Edited by* D.T.W. Evans and A. Kerr. Geological Association of Canada–Mineralogical Association of Canada (GAC–MAC) Annual Meeting, St. John's, Nfld., pp. 167–187.

Swanenberg, H.E.C. 1979. Phase equilibria in carbonic systems, and their application to freezing studies of fluid inclusions. Contributions to Mineralogy and Petrology, **68**: 303–306. doi:10.1007/BF00371552.

Swinden, H.S. 1991. Geology and metallogeny of the Buchans–Robert's Arm belt and related rocks. *In* Metallogenic Framework of Base and Precious Metal Deposits, Central and Western Newfoundland (Field Trip 1). *Edited by* H.S. Swinden, D.T.W. Evans, and B.F. Kean. Geological Survey of Canada, Open File 2156, 81–83.

Ulrich, M.R., and Bodnar, R.J. 1988. Systematics of stretching of fluid inclusions; II, Barite at 1 atm confining pressure. Economic Geology, **83**: 1037–1046. doi:10.2113/gsecongeo.83.5.1037.

Van den Kerkhof, A., and Thiery, R. 2001. Carbonic inclusions. Lithos, **55**: 49–68. doi:10.1016/S0024-4937(00)00038-4.

van Staal, C.R. 2007. Pre-Carboniferous tectonic evolution and metallogeny of the Canadian Appalachians. *In* Mineral Resources of Canada: A Synthesis of Major Deposit Types, District Metallogeny, the Evolution of Geological Provinces, and Exploration Methods. *Edited by* W.D. Goodfellow. Geological Association of Canada, Mineral Deposits Division, Special Publication, **5**: 793–818.

van Staal, C.R., and Barr, S.M. 2012. Lithospheric architecture and tectonic evolution of the Canadian Appalachians and associated Atlantic margin. Tectonic styles in Canada: The LITHOPROBE perspective: Geological Association of Canada Special Paper, **49**: 55.

van Staal, C.R, Dewey, J., Mac Niocaill, C., and McKerrow, W. 1998. The Cambrian-Silurian tectonic evolution of the northern Appalachians and British Caledonides: History of a complex, west and southwest Pacific-type segment of Iapetus. London Geological Society Special Publications, **143**: 197–242. doi:10.1144/GSL.SP.1998.143.01.17.

van Staal, C.R., Barr, S.M., Fyffe, L.R., McNicoll, V., Pollock, J.C., Reusch, D.N., et al. 2002. Ganderia—an important peri-Gondwanan terrane in the northern Appalachians. *In* Abstract. Geological Society of America, Northeastern Section, meeting, Springfield, Massachusetts.

Veizer, J., Ala, D., Azmy, K., Bruckschen, P., Buhl, D., Bruhn, F., et al. 1999. $^{87}Sr/^{86}Sr$, $\delta^{13}C$ and $\delta^{18}O$ evolution of Phanerozoic seawater. Chemical Geology, **161**: 59–88. doi:10.1016/S0009-2541(99)00081-9.

Von Damm, K.L. 1990. Seafloor hydrothermal activity: black smoker chemistry and chimneys. Annual Review of Earth and Planetary Sciences, **18**: 173–204. doi:10.1146/annurev.ea.18.050190.001133.

Von Damm, K.L., Edmond, J.M., Grant, B., Measures, C.I., Walden, B., and Weiss, R.F. 1985. Chemistry of submarine hydrothermal solutions at 21° N, East Pacific Rise. Geochimica et Cosmochimica Acta, **49**: 2197–2220. doi:10.1016/0016-7037(85)90222-4.

Wagner, D.W. 1993. Volcanic stratigraphy and hydrothermal alteration associated with the Duck Pond and Boundary volcanogenic massive sulphide deposits, central Newfoundland. Unpublished dissertation, Department of Earth Sciences, Carleton University, Ottawa, Ont.

Watanabe, M., and Sakai, H. 1983. Stable isotope geochemistry of sulphates from the Neogene ore deposits in the Green Tuff region, Japan. Economic Geology Monograph, **5**: 282–291.

Whitford, D.J., Korsch, M.J., and Solomon, M. 1992. Strontium isotope studies of barites; implications for the origin of base metal mineralization in Tasmania. Economic Geology, **87**: 953–959. doi:10.2113/gsecongeo.87.3.953.

Williams, H. 1995. Geology of the Appalachian-Caledonian Orogen in Canada and Greenland. Geological Survey of Canada: Minister of Energy, Mines and Resources Canada, p. 944.

Williams, H., Colman-Sadd, S.P., and Swinden, H.S. 1988. Tectonic-stratigraphic subdivisions of central Newfoundland. Current Research, Part B. Geological Survey of Canada, Paper, **88**: 91–98.

Zagorevski, A., and Van Staal, C.R. 2011. The record of Ordovician arc–arc and arc–continent collisions in the Canadian Appalachians during the closure of Iapetus. *In* Arc-continent collision. Springer, Berlin, Heidelberg, pp. 341–371.

Zagorevski, A., Van Staal, C.R, McNicoll, V., and Rogers, N. 2007. Upper Cambrian to upper Ordovician peri-Gondwanan island arc activity in the Victoria Lake supergroup, central Newfoundland: Tectonic development of the northern Ganderian margin. American Journal of Science, **307**: 339–370. doi:10.2475/02.2007.02.

Zagorevski, A., van Staal, C.R., Rogers, N., McNicoll, V., Dunning, G.R., and Pollock, J.C. 2010. Middle Cambrian to Ordovician arc-backarc development on the leading edge of Ganderia, Newfoundland Appalachians. Geological Society of America Memoir, **206**: 367–396.

Zhu, C. 2004. Coprecipitation in the barite isostructural family: 1. binary mixing properties. Geochimica et Cosmochimica Acta, **68**: 3327–3337. doi:10.1016/j.gca.2003.10.014.

Appendix A: Whole-rock lithogeochemistry results

Whole-rock major, trace, and rare earth element (REE) concentrations were determined on 10 of the 18 samples analyzed for Sr isotope geochemistry Table A1. Samples were crushed and sieved

Table A1. Whole-rock lithogeochemical data of barite samples from the Lemarchant deposit.

Sample	CNF31816	CNF31861	CNF31733	CNF31810	CNF31730	CNF31721	CNF31874	CNF31865	CNF31868	CNF31855
Drill hole	LM08-19	LM11-68	LM13-94	LM10-43	LM13-94	LM13-73	LM13-82	LM14-96	LM14-96	LM11-52
Depth (m)	98.1	199.9	341.4	218.8	326.3	332.9	340.8	309.9	314.4	216.2
Mineralized zone	24 zone	Main zone	Northwest zone	Main zone	Northwest zone	Northwest zone	Northwest zone	Northwest zone	Northwest zone	Main zone
SiO_2 (wt.%)	0.83	0.53	1.46	0.50	1.47	0.42	4.63	0.03	0.23	1.18
Al_2O_3	0.63	0.08	0.12	0.06	0.77	0.14	0.19	<0.01	0.10	0.43
Fe_2O_3	4.28	0.44	0.28	0.87	0.41	0.23	0.51	0.06	0.12	0.28
MnO	0.03	<0.001	<0.001	0.06	<0.001	0.01	<0.001	<0.001	<0.001	0.00
MgO	0.28	0.08	0.08	1.87	0.14	0.12	0.02	0.03	0.02	0.17
CaO	2.51	0.13	0.14	2.82	0.18	0.20	0.06	0.06	0.03	0.31
Na_2O	0.01	<0.01	<0.01	<0.01	0.02	0.03	0.04	<0.01	<0.01	0.05
K_2O	0.07	<0.01	0.02	<0.01	0.10	<0.01	0.03	<0.01	<0.01	0.04
TiO_2	0.01	0.00	0.00	<0.001	0.00	<0.001	0.00	<0.001	0.00	0.00
P_2O_5	0.25	0.02	0.01	0.01	0.09	0.01	<0.01	<0.01	<0.01	0.08
LOI	2.81	0.70	0.68	1.72	0.86	0.83	1.62	0.23	0.15	0.91
Total	11.71	1.99	2.80	7.94	4.04	1.99	7.12	0.40	0.65	3.47
Ba (ppm)	510000.00	551200.00	548300.00	505200.00	520300.00	547300.00	521400.00	568600.00	576500.00	543100.00
Cu	430.00	2780.00	3070.00	7090.00	2790.00	2000.00	1100.00	1390.00	240.00	1060.00
Zn	190.00	5040.00	5160.00	>10000	>10000	>10000	>10000	5260.00	510.00	>10000
Pb	326.00	8640.00	4670.00	5320.00	>10000	8460.00	6880.00	2910.00	401.00	3370.00
Ag	0.80	16.10	13.50	1.50	8.50	4.20	<0.5	1.10	1.00	2.30
Cr	<20	<20	<20	<20	<20	<20	<20	<20	<20	<20
Co	<1	<1	<1	<1	<1	<1	<1	<1	<1	<1
Ni	30.00	<20	<20	<20	<20	<20	<20	<20	<20	<20
Sc	<1	<1	<1	<1	<1	<1	<1	<1	<1	<1
Be	<1	<1	<1	<1	<1	<1	<1	<1	<1	<1
V	103.00	10.00	20.00	6.00	102.00	15.00	11.00	<5	19.00	45.00
Ga	3.00	3.00	3.00	7.00	10.00	11.00	6.00	2.00	2.00	9.00
Ge	<0.5	<0.5	14.40	1.40	4.70	3.60	<0.5	<0.5	<0.5	<0.5
As	105.00	378.00	53.00	47.00	52.00	30.00	105.00	13.00	29.00	22.00
Rb	1.00	<1	<1	<1	2.00	<1	<1	<1	<1	<1
Sr	4889.00	5905.00	9348.00	4034.00	5419.00	4997.00	3604.00	7438.00	7233.00	5693.00
Y	12.10	4.20	4.90	3.80	6.80	4.80	4.00	3.60	3.80	8.70
Zr	6.00	2.00	3.00	2.00	4.00	2.00	3.00	2.00	3.00	2.00
Nb	<0.2	<0.2	<0.2	<0.2	<0.2	<0.2	<0.2	<0.2	<0.2	<0.2
Mo	3.00	33.00	59.00	>100	68.00	81.00	>100	7.00	3.00	76.00
In	<0.1	<0.1	<0.1	<0.1	<0.1	<0.1	<0.1	<0.1	<0.1	<0.1
Sn	<1	<1	<1	<1	<1	<1	<1	<1	<1	<1
Sb	30.40	103.00	56.10	64.60	119.00	87.10	46.30	12.60	23.80	48.70
Cs	<0.1	<0.1	<0.1	<0.1	<0.1	<0.1	<0.1	<0.1	<0.1	<0.1
La	7.12	12.80	11.40	7.22	10.90	8.80	7.40	11.10	7.72	8.47
Ce	4.09	9.23	8.05	2.57	7.30	4.38	5.12	7.29	3.26	5.16
Pr	0.64	0.63	0.71	0.19	0.65	0.30	0.39	0.52	0.21	0.57
Nd	3.06	1.62	2.12	0.55	1.98	0.80	1.48	1.22	0.56	2.29
Sm	1.47	0.73	0.97	0.67	0.79	0.71	1.05	0.71	0.64	1.27
Eu	1.88	0.19	0.07	<0.005	1.05	0.62	<0.005	1.68	0.65	2.45
Gd	1.99	1.14	1.28	0.91	1.20	1.06	1.63	1.01	0.92	1.84
Tb	0.18	0.04	0.08	0.04	0.07	0.04	0.12	0.05	0.04	0.15
Dy	0.82	0.10	0.22	0.11	0.31	0.12	0.36	0.08	0.10	0.66
Ho	0.16	0.02	0.03	0.02	0.06	0.02	0.05	0.01	0.02	0.11
Er	0.45	0.06	0.09	0.06	0.15	0.06	0.13	0.03	0.05	0.25
Tm	0.07	0.01	0.01	0.01	0.02	0.01	0.02	<0.005	0.01	0.03
Yb	0.41	0.07	0.08	0.07	0.12	0.06	0.11	0.04	0.05	0.18
Lu	0.05	0.01	0.01	0.01	0.02	0.01	0.02	0.01	0.01	0.03
Hf	0.30	0.30	0.30	0.20	0.20	0.30	0.20	0.20	0.20	0.30
Ta	0.27	0.31	0.32	0.28	0.29	0.33	<0.01	0.26	0.26	0.31
W	1.90	2.10	<0.5	0.70	0.60	0.90	<0.5	2.40	0.80	0.80
Tl	<0.05	<0.05	0.29	<0.05	<0.05	<0.05	<0.05	<0.05	<0.05	<0.05
Bi	<0.1	<0.1	<0.1	<0.1	<0.1	<0.1	<0.1	<0.1	<0.1	<0.1
Th	0.12	<0.05	0.44	<0.05	<0.05	<0.05	<0.05	<0.05	<0.05	<0.05
U	8.81	0.50	1.53	3.23	3.05	0.40	3.15	0.08	0.57	10.60

to <80 μm and centrifuged to isolate barite. Samples were analysed by inductively coupled plasma–mass spectrometry (ICP–MS) at Activation Laboratories Inc., Ontario, Canada, using the 4B2-Research-Lithium Metaborate/Tetraborate Fusion-ICP/MS package that involves lithium metaborate/tetraborate fusion and HNO_3 dissolution. Lithogeochemical analyses of these samples were determined prior to Sr isotope analyses to determine the concentrations of Sr and Rb.

Quality assurance and quality control (QA–QC) were monitored using certified reference materials at Activation Laboratories.

Table A2. Summary of accuracy for reference materials used in this study.

Analyte symbol	Unit symbol	Detection limit	Analysis method	NIST 694 RD (%)	DNC-1 RD (%)	GBW 07113 RD (%)	LKSD-3 RD (%)	TDB-1 RD (%)	BaSO4 RD (%)	W-2a RD (%)	DTS-2b RD (%)
SiO_2	%	0.01	FUS-ICP	–1.61	0.11	–2.01	—	—	—	0.82	—
Al_2O_3	%	0.01	FUS-ICP	6.11	–1.25	0.31	—	—	—	0.52	—
Fe_2O_3(T)	%	0.01	FUS-ICP	–5.06	–4.21	0.00	—	—	—	–1.40	—
MnO	%	0.001	FUS-ICP	–13.79	0.00	0.00	—	—	—	4.29	—
MgO	%	0.01	FUS-ICP	3.03	–0.10	–6.25	—	—	—	–0.78	—
CaO	%	0.01	FUS-ICP	–1.72	0.00	3.39	—	—	—	1.10	—
Na_2O	%	0.01	FUS-ICP	0.00	1.06	–3.11	—	—	—	4.21	—
K_2O	%	0.01	FUS-ICP	7.84	–1.71	–0.18	—	—	—	–0.96	—
TiO_2	%	0.001	FUS-ICP	9.09	–2.08	–3.33	—	—	—	0.94	—
P_2O_5	%	0.01	FUS-ICP	0.10	0.00	–40.00	—	—	—	7.69	—
Sc	ppm	1	FUS-ICP	—	0.00	20.00	—	—	—	–2.78	—
Be	ppm	1	FUS-ICP	—	—	0.00	—	—	—	—	—
V	ppm	5	FUS-ICP	–6.21	3.38	20.00	—	—	—	5.34	—
Cr	ppm	20	FUS-MS	—	0.00	—	—	–0.40	—	–2.17	—
Co	ppm	1	FUS-MS	—	–3.51	—	–3.33	—	—	0.00	5.83
Ni	ppm	20	FUS-MS	—	1.21	—	6.38	–2.17	—	0.00	0.26
Cu	ppm	10	FUS-MS	—	10.00	—	–14.29	5.26	—	0.00	—
Zn	ppm	30	FUS-MS	—	0.00	—	—	–3.23	—	–12.50	—
Ga	ppm	1	FUS-MS	—	0.00	—	—	—	—	0.00	—
Ge	ppm	0.5	FUS-MS	—	—	—	—	—	—	40.00	—
As	ppm	5	FUS-MS	—	—	—	0.00	—	—	—	—
Rb	ppm	1	FUS-MS	—	–40.00	—	–8.97	—	—	–4.76	—
Sr	ppm	2	FUS-ICP	—	–0.69	–6.98	—	—	—	3.68	—
Y	ppm	0.5	FUS-MS	—	5.56	—	0.00	–3.61	—	–12.50	—
Zr	ppm	1	FUS-ICP	—	–2.63	–1.49	—	—	—	–5.32	—
Nb	ppm	0.2	FUS-MS	—	–63.33	—	—	—	—	—	—
Mo	ppm	2	FUS-MS	—	—	—	—	—	—	—	—
Ag	ppm	0.5	FUS-MS	—	—	—	3.70	—	—	—	—
In	ppm	0.1	FUS-MS	—	—	—	—	—	—	—	—
Sn	ppm	1	FUS-MS	—	—	—	—	—	—	—	—
Sb	ppm	0.2	FUS-MS	—	–6.25	—	—	—	—	13.92	—
Cs	ppm	0.1	FUS-MS	—	—	—	13.04	—	—	—	—
Ba	ppm	3	FUS-ICP	—	–10.17	–0.79	—	—	–1.40	–4.40	—
La	ppm	0.05	FUS-MS	—	—	—	–7.69	2.35	—	—	—
Ce	ppm	0.05	FUS-MS	—	—	—	–0.56	–0.49	—	7.39	—
Pr	ppm	0.01	FUS-MS	—	—	—	—	—	—	—	—
Nd	ppm	0.05	FUS-MS	—	3.85	—	4.77	6.52	—	3.08	—
Sm	ppm	0.01	FUS-MS	—	—	—	3.75	—	—	0.00	—
Eu	ppm	0.005	FUS-MS	—	—	—	–6.67	0.00	—	—	—
Gd	ppm	0.01	FUS-MS	—	—	—	—	—	—	—	—
Tb	ppm	0.01	FUS-MS	—	—	—	–10.00	—	—	0.00	—
Dy	ppm	0.01	FUS-MS	—	—	—	10.20	–13.00	—	—	—
Ho	ppm	0.01	FUS-MS	—	—	—	—	—	—	1.32	—
Er	ppm	0.01	FUS-MS	—	—	—	—	—	—	—	—
Tm	ppm	0.005	FUS-MS	—	—	—	—	—	—	—	—
Yb	ppm	0.01	FUS-MS	—	5.00	—	7.41	0.00	—	0.00	—
Lu	ppm	0.002	FUS-MS	—	—	—	15.00	—	—	–9.09	—
Hf	ppm	0.1	FUS-MS	—	—	—	2.08	—	—	–3.85	—
Ta	ppm	0.01	FUS-MS	—	—	—	–14.29	—	—	—	—
W	ppm	0.5	FUS-MS	—	—	—	—	—	—	—	—
Tl	ppm	0.05	FUS-MS	—	—	—	—	—	—	–65.00	—
Pb	ppm	5	FUS-MS	—	–4.76	—	—	—	—	—	—
Bi	ppm	0.1	FUS-MS	—	—	—	—	—	—	—	—
Th	ppm	0.05	FUS-MS	—	—	—	0.00	0.00	—	–8.33	—
U	ppm	0.01	FUS-MS	—	—	—	8.70	—	—	–5.66	—

Table A2 (*continued*).

Analyte symbol	Unit symbol	Detection limit	Analysis method	SY-4 RD (%)	CTA-AC-1 RD (%)	BIR-1a RD (%)	NCS DC86321 RD (%)	ZW-C RD (%)	NCS DC70009 RD (%)	OREAS 100a RD (%)	OREAS 101a RD (%)
SiO_2	%	0.01	FUS-ICP	0.38	—	0.92	—	—	—	—	—
Al_2O_3	%	0.01	FUS-ICP	−0.87	—	2.06	—	—	—	—	—
Fe_2O_3(T)	%	0.01	FUS-ICP	−0.32	—	−2.57	—	—	—	—	—
MnO	%	0.001	FUS-ICP	1.85	—	−2.86	—	—	—	—	—
MgO	%	0.01	FUS-ICP	−7.41	—	−1.24	—	—	—	—	—
CaO	%	0.01	FUS-ICP	0.50	—	1.80	—	—	—	—	—
Na_2O	%	0.01	FUS-ICP	−2.25	—	1.65	—	—	—	—	—
K_2O	%	0.01	FUS-ICP	0.00	—	−33.33	—	—	—	—	—
TiO_2	%	0.001	FUS-ICP	1.05	—	0.00	—	—	—	—	—
P_2O_5	%	0.01	FUS-ICP	−8.40	—	−52.38	—	—	—	—	—
Sc	ppm	1	FUS-ICP	−9.09	—	0.00	—	—	—	—	—
Be	ppm	1	FUS-ICP	15.38	—	—	—	—	—	—	—
V	ppm	5	FUS-ICP	0.00	—	7.42	—	—	—	—	—
Cr	ppm	20	FUS-MS	—	—	5.41	—	—	0.00	—	—
Co	ppm	1	FUS-MS	—	—	−3.85	—	—	8.11	−6.08	−5.74
Ni	ppm	20	FUS-MS	—	—	0.00	—	—	—	—	—
Cu	ppm	10	FUS-MS	—	11.11	—	—	—	9.38	−5.33	—
Zn	ppm	30	FUS-MS	—	5.26	0.00	—	−6.67	10.00	—	—
Ga	ppm	1	FUS-MS	—	—	6.25	—	−4.04	3.03	—	—
Ge	ppm	0.5	FUS-MS	—	—	—	—	—	−0.89	—	—
As	ppm	5	FUS-MS	—	—	—	—	—	4.43	—	—
Rb	ppm	1	FUS-MS	—	—	—	—	—	3.20	—	—
Sr	ppm	2	FUS-ICP	0.92	—	−0.91	—	—	—	—	—
Y	ppm	0.5	FUS-MS	—	4.04	12.50	−0.51	—	−0.78	5.63	0.00
Zr	ppm	1	FUS-ICP	2.32	—	−16.67	—	—	—	—	—
Nb	ppm	0.2	FUS-MS	—	—	—	—	—	—	—	—
Mo	ppm	2	FUS-MS	—	—	—	—	—	—	3.73	−8.68
Ag	ppm	0.5	FUS-MS	—	—	—	—	—	−5.56	—	—
In	ppm	0.1	FUS-MS	—	—	—	—	—	−7.69	—	—
Sn	ppm	1	FUS-MS	—	—	—	—	—	—	—	—
Sb	ppm	0.2	FUS-MS	—	—	3.45	—	—	—	—	—
Cs	ppm	0.1	FUS-MS	—	—	—	—	−2.31	—	—	—
Ba	ppm	3	FUS-ICP	2.94	—	16.67	—	—	—	—	—
La	ppm	0.05	FUS-MS	—	—	−4.76	—	—	8.86	5.38	−3.06
Ce	ppm	0.05	FUS-MS	—	—	−5.26	−3.68	—	8.29	7.13	−1.15
Pr	ppm	0.01	FUS-MS	—	—	—	—	—	1.27	6.16	−2.99
Nd	ppm	0.05	FUS-MS	—	3.96	−4.00	−5.00	—	0.30	9.21	−0.25
Sm	ppm	0.01	FUS-MS	—	0.62	9.09	—	—	4.00	10.17	4.51
Eu	ppm	0.005	FUS-MS	—	7.92	−1.82	—	—	—	9.70	−0.12
Gd	ppm	0.01	FUS-MS	—	0.00	−5.00	—	—	1.35	5.93	—
Tb	ppm	0.01	FUS-MS	—	—	—	0.87	—	−3.03	7.11	−4.90
Dy	ppm	0.01	FUS-MS	—	—	0.00	7.10	—	1.45	5.17	0.60
Ho	ppm	0.01	FUS-MS	—	—	—	4.44	—	−2.22	5.41	4.49
Er	ppm	0.01	FUS-MS	—	—	—	0.42	—	−0.75	8.05	6.67
Tm	ppm	0.005	FUS-MS	—	—	—	−3.97	—	0.00	3.90	3.45
Yb	ppm	0.01	FUS-MS	—	8.77	5.88	2.97	—	6.71	4.70	8.00
Lu	ppm	0.002	FUS-MS	—	—	−13.33	8.70	—	7.50	−0.44	1.88
Hf	ppm	0.1	FUS-MS	—	—	0.00	—	—	—	—	—
Ta	ppm	0.01	FUS-MS	—	—	—	—	0.12	—	—	—
W	ppm	0.5	FUS-MS	—	—	—	—	2.81	−7.27	—	—
Tl	ppm	0.05	FUS-MS	—	—	—	—	−1.18	5.56	—	—
Pb	ppm	5	FUS-MS	—	—	66.67	—	—	—	—	—
Bi	ppm	0.1	FUS-MS	—	—	—	—	—	—	—	—
Th	ppm	0.05	FUS-MS	—	10.55	—	4.24	—	1.77	4.07	8.47
U	ppm	0.01	FUS-MS	—	9.09	—	—	—	—	5.93	0.47

Table A2 (*concluded*).

Analyte symbol	Unit symbol	Detection limit	Analysis method	OREAS 101b RD (%)	JR-1 RD (%)	BXGO-1 RD (%)	BXMG-3 RD (%)	BXSP-1 RD (%)
SiO_2	%	0.01	FUS-ICP	—	—	1.59	–4.37	0.20
Al_2O_3	%	0.01	FUS-ICP	—	—	–0.87	0.40	1.66
Fe_2O_3(T)	%	0.01	FUS-ICP	—	—	—	—	—
MnO	%	0.001	FUS-ICP	—	—	—	—	—
MgO	%	0.01	FUS-ICP	—	—	—	—	—
CaO	%	0.01	FUS-ICP	—	—	—	—	—
Na_2O	%	0.01	FUS-ICP	—	—	—	—	—
K_2O	%	0.01	FUS-ICP	—	—	—	42.86	0.00
TiO_2	%	0.001	FUS-ICP	—	—	–5.87	0.45	0.81
P_2O_5	%	0.01	FUS-ICP	—	—	19.05	–7.61	–16.26
Sc	ppm	1	FUS-ICP	—	—	—	—	—
Be	ppm	1	FUS-ICP	—	—	—	—	—
V	ppm	5	FUS-ICP	—	—	—	—	—
Cr	ppm	20	FUS-MS	—	—	—	—	—
Co	ppm	1	FUS-MS	–4.26	20.48	—	—	—
Ni	ppm	20	FUS-MS	—	—	—	—	—
Cu	ppm	10	FUS-MS	0.96	—	—	—	—
Zn	ppm	30	FUS-MS	—	—	—	—	—
Ga	ppm	1	FUS-MS	—	11.80	—	—	—
Ge	ppm	0.5	FUS-MS	—	—	—	—	—
As	ppm	5	FUS-MS	—	–1.84	—	—	—
Rb	ppm	1	FUS-MS	—	–9.73	—	—	—
Sr	ppm	2	FUS-ICP	—	—	—	—	—
Y	ppm	0.5	FUS-MS	–1.12	2.88	—	—	—
Zr	ppm	1	FUS-ICP	—	—	—	—	—
Nb	ppm	0.2	FUS-MS	—	–1.97	—	—	—
Mo	ppm	2	FUS-MS	0.48	—	—	—	—
Ag	ppm	0.5	FUS-MS	—	—	—	—	—
In	ppm	0.1	FUS-MS	—	—	—	—	—
Sn	ppm	1	FUS-MS	—	4.90	—	—	—
Sb	ppm	0.2	FUS-MS	—	–7.56	—	—	—
Cs	ppm	0.1	FUS-MS	—	9.13	—	—	—
Ba	ppm	3	FUS-ICP	—	—	—	—	—
La	ppm	0.05	FUS-MS	3.42	–1.52	—	—	—
Ce	ppm	0.05	FUS-MS	4.43	–1.91	—	—	—
Pr	ppm	0.01	FUS-MS	0.79	9.32	—	—	—
Nd	ppm	0.05	FUS-MS	0.00	4.72	—	—	—
Sm	ppm	0.01	FUS-MS	2.08	–0.83	—	—	—
Eu	ppm	0.005	FUS-MS	4.38	–10.00	—	—	—
Gd	ppm	0.01	FUS-MS	—	—	—	—	—
Tb	ppm	0.01	FUS-MS	0.56	0.00	—	—	—
Dy	ppm	0.01	FUS-MS	0.62	—	—	—	—
Ho	ppm	0.01	FUS-MS	0.47	—	—	—	—
Er	ppm	0.01	FUS-MS	2.67	—	—	—	—
Tm	ppm	0.005	FUS-MS	4.14	7.46	—	—	—
Yb	ppm	0.01	FUS-MS	3.41	7.03	—	—	—
Lu	ppm	0.002	FUS-MS	0.00	4.23	—	—	—
Hf	ppm	0.1	FUS-MS	—	–0.22	—	—	—
Ta	ppm	0.01	FUS-MS	—	–8.60	—	—	—
W	ppm	0.5	FUS-MS	—	—	—	—	—
Tl	ppm	0.05	FUS-MS	—	–1.28	—	—	—
Pb	ppm	5	FUS-MS	—	–1.55	—	—	—
Bi	ppm	0.1	FUS-MS	—	–28.57	—	—	—
Th	ppm	0.05	FUS-MS	–5.39	5.24	—	—	—
U	ppm	0.01	FUS-MS	–4.04	5.86	—	—	—

Precision could not be calculated because reference materials were only analyzed once because of the low number of sample analyses. Accuracy is summarized for the elements of interest in Table A2. Accuracy for the reference materials is given as percent relative difference (% RD) and calculated using the following equation:

$$\mathrm{RD}(\%) = 100 * \frac{\mu_i - C_i}{C_i}$$

where μ_i is the mean value of element i in the standard over a number of analytical runs, and Ci is the certified value of i in the reference material. Table A2 shows that the accuracy of most elements is –10% ≤ RD ≤ 10%, which shows that the analyses have good accuracy. However, some elements have accuracies above ± 10% because the concentrations of these elements are close to the detection limit.

Appendix B: Precision and accuracy of LA–ICP–MS data

Appendix Table B1 appears on following page.

Table B1. Accuracy and precision of the calibration standard BHVO (LA-ICP-MS) normalized to Sr contents of the barites.

Analyses	Mg	Al	Si	Ca34	Ca44	Sc	Ti	V	Cr	Mn	Fe	Co	Ni	Cu63	Cu65	Zn66	Zn67	Ga	Ge
BHVO-1	43243.20	71953.20	230472.00	81417.60	81417.60	32.99	16592.40	308.09	293.04	1318.68	87318.00	44.00	116.03	127.12	127.12	102.17	102.17	22.02	1.58
BHVO-2	43005.60	72032.40	230472.00	81417.60	81457.20	32.99	16750.80	308.09	292.64	1318.68	87753.60	44.00	116.03	126.72	126.72	100.58	101.77	22.02	1.58
BHVO-3	42966.00	71913.60	230472.00	81457.20	81457.20	32.99	16711.20	308.09	293.04	1318.68	87832.80	44.00	116.03	127.12	127.12	100.98	102.17	21.98	1.62
BHVO-4	43005.60	71953.20	230472.00	81417.60	81417.60	32.99	16711.20	308.09	293.04	1318.68	87832.80	44.00	116.03	127.12	127.12	102.17	102.17	22.02	1.58
BHVO-2G_1	43005.60	72072.00	230472.00	81576.00	81576.00	33.66	16711.20	308.09	293.04	1318.68	87912.00	43.96	116.03	124.74	127.12	102.17	101.77	22.02	1.62
BHVO-2G_2	42966.00	71834.40	230076.00	81180.00	81576.00	32.99	16711.20	307.30	292.64	1314.72	87912.00	43.96	116.03	126.72	126.72	102.17	100.98	22.02	1.62
BHVO-2G_3	43005.60	72072.00	230472.00	81576.00	81417.60	32.99	16711.20	308.09	293.04	1318.68	87912.00	44.00	116.03	127.12	127.12	102.17	102.17	22.02	1.62
BHVO-1	43164.00	72072.00	230472.00	81576.00	81576.00	32.87	16711.20	308.09	293.04	1318.68	87912.00	43.96	116.03	127.12	127.12	102.17	101.77	22.02	1.58
BHVO-2	43164.00	71676.00	230472.00	81180.00	81576.00	32.87	16711.20	308.09	293.04	1318.68	87912.00	43.96	116.03	126.72	127.12	101.77	102.17	21.98	1.58
BHVO-3	43164.00	72072.00	230472.00	81576.00	81576.00	32.87	16750.80	307.69	293.04	1318.68	87912.00	43.96	116.03	127.12	126.72	101.77	101.38	22.18	1.58
BHVO-4	43005.60	72072.00	230472.00	81576.00	81576.00	32.99	16711.20	308.09	293.04	1318.68	87912.00	43.96	116.03	127.12	127.12	102.17	101.77	22.02	1.62
BHVO-2G_1	43164.00	72072.00	230472.00	81576.00	81576.00	32.99	16711.20	308.09	293.04	1318.68	87912.00	43.96	116.03	127.12	127.12	102.17	102.17	22.02	1.58
BHVO-2G_2	43005.60	72072.00	230472.00	81576.00	81576.00	33.03	16711.20	308.09	293.04	1318.68	87912.00	43.96	116.03	127.12	127.12	102.17	102.17	22.02	1.58
BHVO-1	43005.60	71953.20	230472.00	81576.00	81576.00	32.99	16711.20	308.09	293.04	1306.80	87912.00	44.00	116.03	127.12	127.12	101.77	102.17	22.02	1.62
BHVO-2	43005.60	71992.80	230472.00	81576.00	81496.80	33.03	16711.20	308.09	293.04	1318.68	87832.80	44.00	116.03	126.72	127.12	101.77	101.38	22.02	1.58
BHVO-3	42966.00	71913.60	230472.00	81576.00	81576.00	32.99	16711.20	308.09	293.04	1314.72	87793.20	44.00	115.63	127.12	127.12	101.77	101.77	21.98	1.58
BHVO-4	43005.60	72072.00	230472.00	81576.00	81576.00	32.99	16711.20	308.09	293.04	1318.68	87832.80	43.96	116.03	127.12	127.12	102.17	102.17	22.02	1.58
Average	43049.86	71988.14	230448.71	81494.47	81529.41	33.01	16708.87	308.02	292.99	1317.52	87842.12	43.97	116.00	126.88	127.05	101.89	101.89	22.02	1.60
Certified values	42996.47	71978.14	230447.43	81475.91	81475.91	33.00	163000.00	308.00	293.00	1316.58	87836.14	44.00	116.00	127.00	127.00	102.00	102.00	22.00	1.60
Precision	100.12	100.01	100.00	100.02	100.07	100.03	10.25	100.01	100.00	100.07	100.01	99.94	100.00	99.91	100.04	99.89	99.89	100.09	99.87
Accuracy (stddev)	89.52	110.14	96.04	134.63	67.49	0.17	32.75	0.21	0.13	3.06	144.51	0.02	0.10	0.58	0.16	0.46	0.36	0.04	0.02

Analyses	Rb	Y	Zr	Nb	Mo	In	Sn	Sb	Cs	Ba	La	Ce	Pr	Nd	Sm	Eu	Gd155	Gd157
BHVO-1	9.19	26.02	169.88	18.30	3.80	0.10	2.61	0.30	0.10	131.08	15.21	37.62	5.35	24.51	6.10	2.07	6.18	6.18
BHVO-2	9.19	25.98	169.88	18.30	3.80	0.10	2.61	0.32	0.10	131.08	15.21	37.58	5.35	24.51	6.10	2.07	6.14	6.18
BHVO-3	9.19	26.02	170.28	18.30	3.80	0.10	2.61	0.30	0.10	131.08	15.21	37.62	5.35	24.47	6.10	2.08	6.18	6.14
BHVO-4	9.19	26.02	169.88	18.30	3.80	0.10	2.61	0.30	0.10	131.08	15.21	37.58	5.35	24.51	6.10	2.07	6.18	6.30
BHVO-2G_1	9.19	26.02	169.88	18.30	3.80	0.00	2.61	0.30	0.14	131.08	15.21	37.58	5.35	24.51	6.10	2.07	6.18	6.18
BHVO-2G_2	9.19	26.02	169.88	18.30	3.80	0.10	2.57	0.30	0.14	131.08	15.17	37.62	5.35	24.55	6.10	2.07	6.14	6.18
BHVO-2G_3	9.19	26.02	169.88	18.30	3.80	0.10	2.61	0.30	0.10	131.08	15.21	37.58	5.35	24.51	6.10	2.07	6.18	6.18
BHVO-1	9.19	25.98	169.88	18.30	3.80	0.10	2.61	0.30	0.10	135.04	15.21	37.62	5.35	24.51	6.10	2.06	6.18	6.14
BHVO-2	9.19	25.98	169.88	18.30	3.80	0.10	2.61	0.30	0.10	131.08	15.21	37.54	5.35	24.47	6.10	2.06	6.18	6.18
BHVO-3	9.23	26.02	169.88	18.30	3.80	0.10	2.57	0.30	0.10	130.68	15.21	37.62	5.35	24.55	6.10	2.06	6.14	6.14
BHVO-4	9.19	26.02	169.88	18.30	3.80	0.10	2.61	0.30	0.10	131.08	15.21	37.58	5.35	24.51	6.10	2.06	6.18	6.18
BHVO-2G_1	9.19	26.02	169.88	18.30	3.80	0.10	2.61	0.27	0.10	131.08	15.21	37.62	5.35	24.51	6.10	2.06	6.18	6.18
BHVO-2G_2	9.19	26.02	169.88	18.30	3.80	0.10	2.61	0.30	0.10	131.08	15.21	37.58	5.35	24.51	6.10	2.06	6.18	6.18
BHVO-1	9.19	26.02	169.88	18.30	3.80	0.10	2.61	0.34	0.10	131.08	15.21	37.58	5.46	24.51	6.10	2.06	6.18	6.18
BHVO-2	9.19	26.02	169.88	18.30	3.76	0.10	2.61	0.30	0.10	131.08	15.21	37.62	5.35	24.51	6.10	2.08	6.18	6.18
BHVO-3	9.23	25.98	169.88	18.30	3.84	0.10	2.61	0.30	0.10	131.08	15.17	37.58	5.35	24.47	6.10	2.07	6.14	6.18
BHVO-4	9.19	26.02	169.88	18.30	3.84	0.10	2.61	0.30	0.10	131.08	15.21	37.62	5.35	24.51	6.10	2.06	6.18	6.18
Average	9.19	26.01	169.91	18.30	3.80	0.09	2.61	0.30	0.10	131.29	15.20	37.60	5.35	24.51	6.10	2.07	6.17	6.18
Certified values	9.20	26.00	170.00	18.30	3.80	0.10	2.60	0.30	0.10	131.00	15.20	37.60	5.35	24.50	6.10	2.07	6.16	6.16
Precision	99.91	100.03	99.95	99.97	100.10	93.64	100.34	100.55	104.17	100.22	100.01	99.99	100.07	100.04	99.97	99.78	100.13	100.29
Accuracy (stddev)	0.01	0.02	0.10	0.00	0.02	0.02	0.01	0.01	0.01	0.97	0.01	0.02	0.03	0.02	0.00	0.01	0.02	0.03

Analyses	Tb	Dy	Ho	Er	Tm	Yb	Lu	Hf	Ta	W	Pb206	Pb208	Bi	Th	U
BHVO-1	0.92	5.27	0.98	2.56	0.34	2.01	0.28	4.32	1.15	0.22	1.70	1.70	0.00	1.22	0.40
BHVO-2	0.92	5.27	0.98	2.56	0.34	2.02	0.28	4.32	1.15	0.23	1.69	1.70	0.00	1.22	0.40
BHVO-3	0.92	5.31	0.98	2.56	0.34	2.01	0.28	4.32	1.15	0.23	1.70	1.70	0.00	1.22	0.40
BHVO-4	0.92	5.27	0.98	2.56	0.34	2.01	0.28	4.32	1.15	0.23	1.70	1.70	0.01	1.22	0.40
BHVO-2G_1	0.92	5.27	0.98	2.57	0.34	2.02	0.28	4.32	1.15	0.23	1.70	1.70	0.01	1.22	0.40
BHVO-2G_2	0.92	5.27	0.98	2.57	0.34	2.02	0.28	4.32	1.15	0.27	1.70	1.69	0.01	1.22	0.40
BHVO-2G_3	0.92	5.27	0.98	2.56	0.34	2.02	0.28	4.32	1.15	0.10	1.70	1.70	0.01	1.22	0.40
BHVO-1	0.92	5.27	0.98	2.57	0.34	2.02	0.28	4.32	1.15	0.24	1.70	1.70	0.01	1.22	0.40
BHVO-2	0.91	5.27	0.98	2.57	0.34	2.02	0.28	4.32	1.15	0.23	1.69	1.69	0.01	1.22	0.39
BHVO-3	0.92	5.31	0.98	2.57	0.34	2.02	0.28	4.32	1.15	0.23	1.66	1.69	0.01	1.22	0.39
BHVO-4	0.92	5.27	0.98	2.57	0.34	1.90	0.28	4.32	1.15	0.23	1.70	1.70	0.01	1.22	0.41
BHVO-2G_1	0.92	5.27	0.98	2.57	0.34	2.02	0.28	4.32	1.15	0.23	1.70	1.70	0.01	1.22	0.40
BHVO-2G_2	0.92	5.27	0.98	2.57	0.34	2.02	0.28	4.32	1.15	0.23	1.70	1.70	0.01	1.22	0.40
BHVO-1	0.92	5.27	0.98	2.57	0.34	2.02	0.28	4.32	1.15	0.23	1.70	1.70	0.01	1.22	0.40
BHVO-2	0.92	5.27	0.98	2.57	0.34	2.02	0.27	4.32	1.15	0.23	1.70	1.69	0.02	1.22	0.40
BHVO-3	0.92	5.27	0.98	2.57	0.34	2.02	0.28	4.32	1.15	0.23	1.70	1.70	0.01	1.22	0.40
BHVO-4	0.92	5.27	0.98	2.57	0.34	2.02	0.28	4.32	1.15	0.23	1.70	1.70	0.01	1.22	0.40
Average	0.92	5.27	0.98	2.57	0.34	2.01	0.28	4.32	1.15	0.22	1.70	1.70	0.01	1.22	0.40
Certified values	0.92	5.28	0.98	2.56	0.34	2.01	0.28	4.32	1.15	0.23	1.70	1.70	0.01	1.22	0.40
Precision	99.91	99.84	99.93	100.36	100.03	100.03	99.69	99.92	99.94	97.63	99.90	99.86	90.15	99.97	99.77
Accuracy (stddev)	0.00	0.01	0.00	0.01	0.00	0.03	0.00	0.00	0.00	0.03	0.01	0.00	0.01	0.00	0.00

Appendix C: Fluid inclusion microthermometry

Table C1. Results of fluid inclusion microthermometry and salinity calculations for different fluid inclusion assemblages in bladed barite from the Lemarchant deposit.

Sample/ assemblage	Assemblage	Type	Degree of Fill (F)	First melting temperature (T_{mCO2})	Final melting temperature ($T_{m\ ice\ clathrate}$ °C)	Final melting temperature ($T_{m\ ice}$ °C)	Temperature of homogenization (T_{hCO2})	Final homogenization temperature (T_h °C)	Salinity* (NaCl eq)
CNF31723 (vein)									
1	1	I	0.75	–56.10	8.90	—	—	248.10	1.78
2	1	I	0.75	–56.10	9.10	—	—	248.10	1.40
3	1	I	0.75	—	9.10	—	—	248.10	1.40
4	1	I	0.75	—	9.10	—	—	246.00	1.40
5	1	I	0.80	–56.00	7.80	—	—	246.00	3.90
6	1	I	0.80	–56.00	9.70	—	—	247.80	0.20
7	1	III	0.99	–56.00	—		—	—	
8	1	III	0.99	—	7.80		—	—	3.90
1	2	I	0.75	–56.00	9.70	—	—	236.00	0.20
2	2	I	0.75	—	—	—	—	236.00	
3	2	I	0.75	—	—	—	—	—	
4	2	I	0.75	–56.00	—	—	—	—	
CNF31723 (bladed barite)									
1	1	II	0.95	—	—	—	—	decrepitated	
2	1	II	0.95	—	—	–0.30	—	decrepitated	
3	1	II	0.95	—	—	1.00	—	198.30	
4	1	II	0.95	—	10.50	—	—	decrepitated	0.00
5	1	II	0.95	—	9.30	—	—	—	1.00
6	1	II	0.95	—	—	—	—	—	
1	2	II	0.75	—	—	–3.20	—	—	
2	2	II	0.75	—	—	—	—	214.40	
3	2	II	0.75	—	—	–2.90	—	216.20	
CNF31874 (bladed barite)									
1	1	II	0.75	–59.20	9.50	–4.00	—		0.62
2	1	II	0.95	—	9.50	—	27.70–29.00	211.70	0.62
3	1	III	1.00	—	7.10	—	—	—	5.16
4	1	II	0.75	—		–3.50	—	—	
5	1	II	0.90	—		–3.00	—	—	
6	1	II	0.95	—		—	—	—	
7	1	II	0.95	—		—	—	—	
8	1	II	0.95	—			—	—	
9	1	II	0.95	—			—	—	
10	1	II	0.95	—			—	—	
1	2	I	0.75	–56.30	–4.70	–4.70	31.00	—	
2	2	I	0.50	–56.30	—	—	—	decrepitated	
3	2	I	0.75	–56.30	—	—	—	261.30	
4	2	III	1.00	—	10.30	—	—	decrepitated	~0.00
5	2	I	0.75	—	—	—	—	256.00	
6	2	I	0.75	—	—	—	—	—	
7	2	I	0.75	—	9.90	—	—	276.00	~0.00
8	2	I	0.75	—	9.90	—	—	decrepitated	~0.00
9	2	I	0.75	—	9.90	—	—	decrepitated	~0.00
10	2	I	0.75	—	—	—	—	decrepitated	
CNF31865 (bladed barite)									
1	1	I	0.75	–56.50	—	—	30.80	—	
2	1	I	0.75	—	9.50	—	—	—	0.60
3	1	I	0.95	—	7.60	—	—	—	4.20
4	1	I	0.75	—	—	—	—	—	
5	1	I	—	—	—	—	—	—	
6	1	I	—	—	—	—	—	—	
7	1	I	—	—	—	—	—	—	
8	1	I	0.75	—	9.50	—	—	—	
9	1	I	0.95	—	9.10	—	30.20	—	0.60
10	1	I	0.75	—	—	—	—	228.00	1.40
11	1	I	0.75	—	—	—	—	250.00	
12	1	I	0.75	—	—	—	—	250.00	

Table C1 (*concluded*).

Sample/ assemblage	Assemblage	Type	Degree of Fill (F)	First melting temperature (T_{mCO2})	Final melting temperature ($T_{m\ ice\ clathrate}$ °C)	Final melting temperature ($T_{m\ ice}$ °C)	Temperature of homogenization (T_{hCO2})	Final homogenization temperature (T_h °C)	Salinity* (NaCl eq)
13	1	I	0.75	—	—	—	—	255.00	
1	2	I	0.75	–56.20	—	—	30.40	—	
2	2	I	0.75	—	—	—	30.40	—	
3	2	I	0.75	—	—	—	—	—	
4	2	I	0.95	—	9.40	—	—	—	
5	2	I	0.75	—	9.70	—	—	—	0.80
6	2	I	0.75	—	—	—	—	—	0.20
8	2	II	0.90	—	—	—	—	—	
9	2	II	0.95	—	—	—	—	—	
10	2	II	0.95	—	—	—	—	—	
11	2	II	0.75	—	—	—	—	—	
12	2	II	0.75	—	—	—	—	245.00	
CNF31860 (bladed barite)									
1	1	I	0.75	—	9.80	—	30.80	—	
2	1	I	0.75	–57.10	9.80	—	—	—	0.00
3	1	I	0.90	—	—	—	—	191.00	0.00
4	1	I	0.75	—	—	—	—	245.30	
5	1	I	0.90	—	—	—	—	245.30	

*Salinities (NaCl eq) were calculated using the Q2 program within the software CLATHRATES.

Table C2. Isochore calculations for fluid inclusion assemblages using the FLUIDS software package (Anderko and Pitzer 1993; Duan et al. 1995).

Sample-FIA	T (K)	T (°C)	P (MPa)	P (bar)	V (cc/mol)
CN31860 (bladed barite)	518.45	245.30	199.39	1993.94	22.14
	536.19	263.04	215.32	2153.16	22.14
	553.92	280.77	232.60	2326.02	22.14
	571.66	298.51	251.19	2511.90	22.14
	589.39	316.24	271.24	2712.36	22.14
	607.13	333.98	292.12	2921.24	22.14
	624.86	351.71	313.74	3137.43	22.14
	642.60	369.45	336.01	3360.06	22.14
	660.33	387.18	358.87	3588.72	22.14
	678.07	404.92	382.34	3823.38	22.14
	695.80	422.65	406.40	4064.04	22.14
	713.54	440.39	431.05	4310.47	22.14
	731.27	458.12	456.22	4562.23	22.14
	749.01	475.86	481.88	4818.85	22.14
	766.74	493.59	507.99	5079.91	22.14
	784.48	511.33	537.73	5377.29	22.14
	802.21	529.06	566.80	5668.00	22.14
	819.95	546.80	596.11	5961.06	22.14
	837.68	564.53	625.64	6256.37	22.14
	855.42	582.27	655.39	6553.85	22.14
	873.15	600.00	685.34	6853.45	22.14
CNF31865 (bladed barite)	523.15	250.00	192.14	1921.44	23.06
	540.65	267.50	204.04	2040.38	23.06
	558.15	285.00	217.86	2178.61	23.06
	575.65	302.50	233.68	2336.79	23.06
	593.15	320.00	251.43	2514.29	23.06
	610.65	337.50	270.05	2700.54	23.06
	628.15	355.00	289.32	2893.19	23.06
	645.65	372.50	309.08	3090.82	23.06
	663.15	390.00	329.32	3293.20	23.06
	680.65	407.50	350.09	3500.87	23.06
	698.15	425.00	371.43	3714.29	23.06
	715.65	442.50	393.34	3933.36	23.06
	733.15	460.00	415.75	4157.47	23.06
	750.65	477.50	438.59	4385.92	23.06
	768.15	495.00	461.82	4618.17	23.06
	785.65	512.50	489.04	4890.39	23.06
	803.15	530.00	515.25	5152.49	23.06
	820.65	547.50	541.64	5416.38	23.06

Table C2 (*concluded*).

Sample-FIA	T (K)	T (°C)	P (MPa)	P (bar)	V (cc/mol)
	838.15	565.00	568.21	5682.07	23.06
	855.65	582.50	594.96	5949.58	23.06
	873.15	600.00	621.89	6218.91	23.06
CNF3174 (bladed barite)	484.15	211.00	166.37	1663.68	23.99
	503.60	230.45	175.22	1752.17	23.99
	523.05	249.90	186.26	1862.60	23.99
	542.50	269.35	199.17	1991.75	23.99
	561.95	288.80	213.88	2138.85	23.99
	581.40	308.25	230.42	2304.22	23.99
	600.85	327.70	248.36	2483.55	23.99
	620.30	347.15	267.16	2671.64	23.99
	639.75	366.60	286.64	2866.40	23.99
	659.20	386.05	306.71	3067.07	23.99
	678.65	405.50	327.38	3273.82	23.99
	698.10	424.95	348.70	3486.95	23.99
	717.55	444.40	370.63	3706.31	23.99
	737.00	463.85	393.13	3931.27	23.99
	756.45	483.30	416.12	4161.17	23.99
	775.90	502.75	442.02	4420.19	23.99
	795.35	522.20	468.71	4687.05	23.99
	814.80	541.65	495.59	4955.88	23.99
	834.25	561.10	522.66	5226.63	23.99
	853.70	580.55	549.93	5499.30	23.99
	873.15	600.00	577.39	5773.87	23.99
CNF31874-2 (bladed barite)	533.15	260.00	170.74	1707.43	24.17
	550.15	277.00	183.80	1838.01	24.17
	567.15	294.00	197.73	1977.26	24.17
	584.15	311.00	212.51	2125.11	24.17
	601.15	328.00	227.99	2279.95	24.17
	618.15	345.00	244.07	2440.67	24.17
	635.15	362.00	260.67	2606.66	24.17
	652.15	379.00	277.75	2777.53	24.17
	669.15	396.00	295.31	2953.07	24.17
	686.15	413.00	313.32	3133.18	24.17
	703.15	430.00	331.77	3317.72	24.17
	720.15	447.00	350.64	3506.45	24.17
	737.15	464.00	369.91	3699.08	24.17
	754.15	481.00	389.54	3895.35	24.17
	771.15	498.00	409.50	4095.03	24.17
	788.15	515.00	433.81	4338.07	24.17
	805.15	532.00	456.63	4566.33	24.17
	822.15	549.00	479.61	4796.09	24.17
	839.15	566.00	502.73	5027.31	24.17
	856.15	583.00	525.99	5259.92	24.17
	873.15	600.00	549.39	5493.87	24.17

References

Anderko, A., and Pitzer, K.S. 1993. Phase equilibria and volumetric properties of the systems KCl-H_2O and NaCl-KCl-H_2O above 573K: Equation of state representation. Geochimica et Cosmochimica Acta, **57**: 4885–4897. doi:10.1016/0016-7037(93)90127-I.

Duan, Z., Møller, N., and Weare, J.H. 1995. Equation of state for the NaCl-H_2O-CO_2 system: prediction of phase equilibria and volumetric properties. Geochimica et Cosmochimica Acta, **59**: 2869–2882. doi:10.1016/0016-7037(95)00182-4.